

REPORT DOCUMENTATION PAGE

Form Approved
OMB No. 0704-0188

Public reporting burden for this collection of information is estimated to average 1 hour per response, including the time for reviewing instructions, searching existing data sources, gathering and maintaining the data needed, and completing and reviewing the collection of information. Send comments regarding this burden estimate or any other aspect of this collection of information, including suggestions for reducing this burden, to Washington Headquarters Services, Directorate for Information Operations and Reports, 1215 Jefferson Davis Highway, Suite 1204, Arlington, VA 22202-4302, and to the Office of Management and Budget, Paperwork Reduction Project (0704-0188), Washington, DC 20503.

1. AGENCY USE ONLY (Leave blank)			2. REPORT DATE 31.Jul.03	3. REPORT TYPE AND DATES COVERED THESIS
4. TITLE AND SUBTITLE "SHAPE MEMORY ALLOY INDUCED WING WARPING FOR A SMALL UNMANNED AERIAL VEHICLE"			5. FUNDING NUMBERS	
6. AUTHOR(S) 2D LT OBENCHAIN MATTHEW B				
7. PERFORMING ORGANIZATION NAME(S) AND ADDRESS(ES) MASSACHUSETTS INSTITUTE OF TECHNOLOGY			8. PERFORMING ORGANIZATION REPORT NUMBER CI02-1194	
9. SPONSORING/MONITORING AGENCY NAME(S) AND ADDRESS(ES) THE DEPARTMENT OF THE AIR FORCE AFIT/CIA, BLDG 125 2950 P STREET WPAFB OH 45433			10. SPONSORING/MONITORING AGENCY REPORT NUMBER	
11. SUPPLEMENTARY NOTES				
12a. DISTRIBUTION AVAILABILITY STATEMENT Unlimited distribution In Accordance With AFI 35-205/AFIT Sup 1			12b. DISTRIBUTION CODE	
13. ABSTRACT (Maximum 200 words)				
DISTRIBUTION STATEMENT A Approved for Public Release Distribution Unlimited			20030909 075	
14. SUBJECT TERMS			15. NUMBER OF PAGES 138	
			16. PRICE CODE	
17. SECURITY CLASSIFICATION OF REPORT	18. SECURITY CLASSIFICATION OF THIS PAGE	19. SECURITY CLASSIFICATION OF ABSTRACT	20. LIMITATION OF ABSTRACT	

Shape Memory Alloy Induced Wing Warping for a Small Unmanned Aerial Vehicle

By

Matthew Bridger Obenchain

B.S. Engineering Mechanics
United States Air Force Academy, 2001

SUBMITTED TO THE DEPARTMENT OF AERONAUTICS AND ASTRONAUTICS IN
PARTIAL FULFILLMENT OF THE REQUIREMENTS FOR THE DEGREE OF

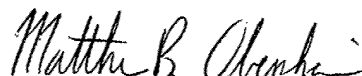
MASTER OF SCIENCE IN AERONAUTICS AND ASTRONAUTICS
AT THE
MASSACHUSETTS INSTITUTE OF TECHNOLOGY

JUNE 2003

© 2003 Matthew Bridger Obenchain. All rights reserved

The author hereby grants to MIT permission to reproduce and to distribute publicly paper and electronic copies of this thesis document in whole or in part.

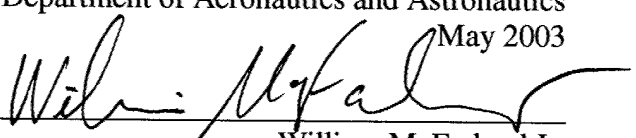
Signature of Author



Department of Aeronautics and Astronautics

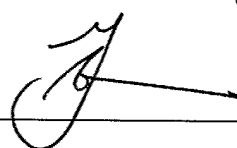
May 2003

Certified by



William McFarland Jr.
Charles Stark Draper Laboratory
Thesis Supervisor

Certified by



Marthinus van Schoor
Visiting Professor of Aeronautics and Astronautics
Thesis Advisor

Accepted by

Edward M. Greitzer
H.N. Slater Professor of Aeronautics and Astronautics
Chair, Committee on Graduate Students

[THIS PAGE INTENTIONALLY LEFT BLANK]

Shape Memory Alloy Induced Wing Warping for a Small Unmanned Aerial Vehicle

By

Matthew Bridger Obenchain

Submitted to the Department of Aeronautics and Astronautics
on May 9, 2003, in partial fulfillment of the
requirements for the degree of
Master of Science in Aeronautics and Astronautics

Abstract

The Wide Area Surveillance Projectile (WASP) is a gun-launched unmanned aerial vehicle designed to be carried as payload in an artillery shell. Due to the 15000 g shock sustained during gun launch, conventional ailerons are too fragile to be a reliable means of roll control for the aircraft. For this reason, the possibility of using shape memory alloys (SMA) to control the vehicle is investigated.

A conceptual design is introduced in which pre-strained Nitinol wires are attached to the surface of the wing. When the resistively heated wires pass a transition temperature, a phase change occurs in the wires and they contract to recover the pre-strain. As the wires contract, they twist the wing in what is known as wing warping.

This conceptual design is refined through extensive modeling and finite element analysis. Thermal analysis is used to determine how fast the wires heat and cool, which determines how fast the vehicle can be controlled. Structural analysis is used to determine the amount of twist induced in the wing when the wires contract. A preliminary performance analysis illustrates what bank angles and roll rates the WASP could achieve when the actuator is used.

Tensile testing of the Nitinol wire is conducted to determine its modulus of elasticity in both its martensite and austenite phases. In addition, cycle tests are performed in which the wire is heated and cooled at constant stress to determine the transition temperatures of the material.

Tests are conducted on prototype wings with Nitinol wires attached to determine the actual performance of the actuator. Using epoxy to attach the Nitinol to the wing is found to be problematic, since the epoxy degrades as the wires are heated. Using mechanical means to attach the wires is shown to be much more effective.

This thesis shows that an SMA actuator can repeatedly twist the wing of a small UAV to angles in excess of one degree. Analytical results show that the wing can be actuated every 3.2 seconds. Performance analysis predicts that roll rates of over 25 degrees/second can be achieved. These results indicate that an SMA actuator has the ability to control the aircraft during slow, banking turns while the aircraft follows a racetrack pattern.

Thesis Supervisor: William McFarland Jr.
Title: Staff, Charles Stark Draper Laboratory

Thesis Advisor: Marthinus van Schoor
Title: Visiting Professor of Aeronautics and Astronautics

[THIS PAGE INTENTIONALLY LEFT BLANK]

Table of Contents

Chapter 1: Introduction	15
1.1 : Wasp Design Evolution	16
1.1.1 : MIT/Draper Project – WASP I	16
1.1.2 : WASP Phase II	16
1.1.3 : WASP G-hardening Program	17
1.2 : Roll Control	18
1.2.1 : Wing Warping	18
1.2.2 : Piezoelectric Actuation	19
1.2.3 : Shape Memory Alloy Actuation	19
1.3 : Thesis Objectives	20
1.4 : Thesis Outline	20
Chapter 2: Shape Memory Alloy Background	21
2.1 : Martensitic Transformations	21
2.2 : The Shape Memory Effect	23
2.3 : Stress-Strain Behavior	25
2.4 : Transition Temperature and Hysteresis	26
2.5 : Material Properties	27
2.6 : Two-Way Shape Memory	27
2.7 : Stress-Induced Martensite and Superelasticity	28
2.8 : Two-Way Systems	29
Chapter 3: Previous Applications of Shape Memory Alloys	31
3.1 : Shape Memory Alloy Composites	31
3.2 : Shape Memory Alloy Wire Actuators	33
3.3 : Large Scale SMA Actuators	35
Chapter 4: Conceptual Design	37
4.1 : Wasp Wing Design	37
4.2 : Design Approaches	38
4.2.1 : Bias Approach	38
4.2.2 : Differential Approach	39

4.3 : Design Concept.....	39
Chapter 5: Modeling and Analysis	43
5.1 : Thermal Modeling	43
5.1.1 : Single Wire Model.....	43
5.1.2 : Wing Section Model	48
5.1.3 : Conclusions from Thermal Modeling.....	53
5.2 : Structural Modeling	54
5.2.1 : Initial Wing Twist Models.....	54
5.2.2 : Bonding Analysis.....	59
5.2.3 : Wing Test Blank Model.....	61
5.3 : Thermal – Structural Interaction.....	66
5.4 : Performance Analysis.....	71
5.4.1 : Bias Approach Performance	75
5.4.2 : Differential Approach Performance.....	81
5.4.3 : Comparison	86
5.5 : Power Consumption.....	86
Chapter 6: Material Characterization Tests	89
6.1 : Nitinol Wire	89
6.2 : Tensile Tests	89
6.2.1 : Test Specimens	90
6.2.2 : Test Setup	90
6.2.3 : Low Temperature Tests	91
6.2.4 : High Temperature Tests.....	92
6.3 : Cycle Tests.....	94
6.3.1 : Test Specimen.....	94
6.3.2 : Test Setup	94
6.3.3 : Test Procedure	97
6.3.4 : Test Results.....	97
Chapter 7: Prototype Construction and Testing.....	101
7.1 : Construction.....	101
7.1.1 : Lay-up and Curing of Test Blanks.....	101

7.1.2 : Preparation of Nitinol Wire	103
7.2 : Wires Attached with Epoxy.....	106
7.2.1 : Tests One and Two	106
7.2.2 : Test Three	110
7.2.3 : Test Four.....	112
7.2.4 : Conclusion	116
7.3 : Wires Attached with Pins	117
7.3.1 : Bias Test	118
7.3.2 : Differential Test.....	121
7.3.3 : Conclusion	124
7.4 : Comparison of Analytical and Experimental Results.....	125
7.4.1 : Structural Analysis.....	125
7.4.2 : Time Response.....	126
7.4.3 : Conclusion	128
Chapter 8: Conclusions and Recommendations	129
8.1 : Conclusions.....	129
8.2 : Recommendations.....	130
References.....	135

List of Figures

Figure 1.1: Phase II WASP	17
Figure 1.2: WASP in Flight and Launch Configurations	18
Figure 2.1: Crystal Structures	22
Figure 2.2: Accommodation Modes	23
Figure 2.3: Detwinning	23
Figure 2.4: Shape Memory Cycle	24
Figure 2.5: SMA Martensitic Stress-Strain Curve.....	25
Figure 2.6: Transformation vs. Temperature Curve	26
Figure 2.7: Two-Way Shape Memory	28
Figure 2.8: Superelasticity	29
Figure 3.1: Lobster Robot	34
Figure 3.2: Biomimetic Hydrofoil	34
Figure 3.3: SMA Actuated Wing	35
Figure 4.1: WASP Wing in Flight and Launch Configurations.....	37
Figure 4.2: Wire Options	40
Figure 4.3: Conceptual Design	40
Figure 5.1: Finite Element Model of Single Wire	44
Figure 5.2: Typical Temperature Response of Nitinol Wires (Time in seconds, Temperature in degrees Celsius)	46
Figure 5.3: Plain Wires Exposed to Forced Convection.....	47
Figure 5.4: Wing Cutout Diagram	49
Figure 5.5: Wing Section Model Geometries	49
Figure 5.6: Typical Meshed Model.....	50
Figure 5.7: Heating and Cooling of Completely Enclosed Wires	51
Figure 5.8: Heating and Cooling of Half Enclosed Wires.....	52
Figure 5.9: Heating and Cooling Response of Covered 1000 Micron Wire (Time in seconds, Temperature in degrees Celsius).....	53
Figure 5.10: Wing Twist Configurations	57
Figure 5.11: Meshed Model of Configuration 3	58

Figure 5.12: Rotation Results for Configuration 3	59
Figure 5.13: Bonding Analysis Stress Results.....	60
Figure 5.14: Stress in Epoxy Layer.....	61
Figure 5.15: Dimensions and Location of Nitinol Section	62
Figure 5.16: Meshed Wing Blank Model	64
Figure 5.17: Bias Approach Wing Twist Results	65
Figure 5.18: Differential Approach Wing Twist Results.....	66
Figure 5.19: Heat Distribution in Wing	67
Figure 5.20: Deflection Due to Expansion of Top Fiberglass Layer.....	68
Figure 5.21: Deflection from Foam Expansion in X-Direction.....	69
Figure 5.22: Deflection from Foam Expansion in Y-Direction.....	69
Figure 5.23: Deflection from Foam Expansion in Z-Direction	70
Figure 5.24: Wing Twist Profile for Inner Wing Panel	72
Figure 5.25: Steady State Roll Rate for Various Maximum Twist Angles	73
Figure 5.26: Roll Rate and Bank Angle Response for One Degree Wing Twist.....	73
Figure 5.27: Roll Rate Response for Bias Actuation of One Wing (One Degree Wing Twist)	76
Figure 5.28: Bank Angle Response for Bias Actuation of One Wing (One Degree Wing Twist)	76
Figure 5.29: Bank Angles From Bias Actuation of One Wing.....	77
Figure 5.30: Roll Rate Response for Bias Actuation with 0.1 Second Delay	77
Figure 5.31: Bank Angle Response for Bias Actuation with 0.1 Second Delay	78
Figure 5.32: Roll Rate Response for Bias Actuation with 0.5 Second Delay	78
Figure 5.33: Bank Angle Response for Bias Actuation with 0.5 Second Delay	79
Figure 5.34: Roll Rate Response for Bias Actuation with 0.5 Seconds Additional Power	80
Figure 5.35: Roll Rate Response for Bias Actuation with 0.5 Seconds Additional Power	80
Figure 5.36: Roll Rate Response for Differential Actuation of One Wing (One Degree Wing Twist)	81
Figure 5.37: Bank Angle Response for Differential Actuation of One Wing (One Degree Wing Twist)	82
Figure 5.38: Roll Rate Response for Differential Actuation with 0.1 Second Delay.....	82

Figure 5.39: Bank Angle Response for Differential Actuation with 0.1 Second Delay	83
Figure 5.40: Roll Rate Response for Differential Actuation with 0.5 Second Delay	83
Figure 5.41: Bank Angle Response for Differential Actuation with 0.5 Second Delay	84
Figure 5.42: Roll Rate Response for Differential Actuation with 0.5 Seconds Additional Power	85
Figure 5.43: Bank Angle Response for Differential Actuation with 0.5 Seconds Additional Power	85
Figure 6.1: INSTRON Grip Setup	91
Figure 6.2: Stress vs. Strain Curves for Low Temperature Tensile Tests	92
Figure 6.3: Stress vs. Strain Curves for High Temperature Tensile Tests.....	93
Figure 6.4: Test Fixture Diagram.....	95
Figure 6.5: Test Fixture.....	96
Figure 6.6: Typical Cycle Test Results.....	98
Figure 6.7: Transition Temperature Determination	99
Figure 7.1: Lay-up Diagram	102
Figure 7.2: Cure Setup	102
Figure 7.3: Dimensions of Nitinol Covered Area.....	103
Figure 7.4: Wire Arrangement.....	104
Figure 7.5: Pre-straining Fixture.....	104
Figure 7.6: Bolt End of Pre-straining Fixture Showing Crimped End of Wire	105
Figure 7.7: Clamp End of Pre-straining Fixture	105
Figure 7.8: Wire Bending Fixture.....	106
Figure 7.9: Nitinol Wires Attached With Epoxy	107
Figure 7.10: Setup for Tests One and Two	108
Figure 7.11: Test Specimen Prior to Test Two	109
Figure 7.12: Test Specimen After Test Two, Showing Bond Failure	109
Figure 7.13: Oven Test Setup	111
Figure 7.14: Wing Twist from Oven Test.....	111
Figure 7.15: LVDT Setup	113
Figure 7.16: First Actuation of Epoxy Covered Wires	114
Figure 7.17: Third Actuation of Epoxy Covered Wires	115

Figure 7.18: Fifth Actuation of Epoxy Covered Wires.....	115
Figure 7.19: Heating and Cooling of Epoxy Covered Wires.....	116
Figure 7.20: Nitinol Wire Attached With Pins	117
Figure 7.21: Enlarged View of Pins.....	118
Figure 7.22: First Actuation Cycle.....	119
Figure 7.23: Second Actuation Cycle	120
Figure 7.24: Twist Angle Evolution with Bias Actuation	121
Figure 7.25: First Actuation of Top Wires.....	122
Figure 7.26: First Actuation of Bottom Wires	123
Figure 7.27: Twist Angle Evolution for Differential Actuation	124
Figure 7.28: Revised Heating and Cooling Curve for 1000 Micron Wires (Time in seconds, Temperature in Degrees Celsius).....	126
Figure 7.29: Heating and Cooling of Nitinol Wire Attached Using Epoxy.....	127
Figure 7.30: Heating and Cooling of Wires Attached Using Pins.....	128

List of Tables

Table 2.1: Nitinol Material Properties	27
Table 5.1: Nitinol Thermal Properties [28].....	44
Table 5.2: Wing Section Thermal Properties [28-30].....	48
Table 5.3: Rohacell Foam Properties [30]	54
Table 5.4: Fiberglass Properties [31].....	55
Table 5.5: Nitinol Properties [31]	55
Table 5.6: Wing Twist Results.....	57
Table 5.7: Nitinol Austenite Properties [31].....	63
Table 5.8: Epoxy Properties [32].....	63
Table 5.9: Coefficients of Thermal Expansion [30,31]	68
Table 5.10: Maximum Deflections from Foam Expansion	70
Table 5.11: Roll Equation Constants	71
Table 5.12: Heating and Cooling Times for Nitinol Wire	74
Table 6.1: Experimental Transition Temperature Results	99
Table 6.2: Transition Temperature Variance Between Samples (degrees Celsius).....	100

Chapter 1: Introduction

The Wide Area Surveillance Projectile (WASP) program began as part of the MIT/Draper Technology Development Partnership Project, which was a joint effort between the MIT Aeronautics and Astronautics Department and the Charles Stark Draper Laboratory. Since it started in 1996, the WASP program's goal has been to develop a small unmanned aerial vehicle (UAV) to be carried as cargo in a 155 mm artillery shell.

Prior to launch, the WASP is folded and enclosed in a shroud, which is inserted into the artillery shell. When ground forces need information about the battlefield, they can launch the shell. Once the shell reaches the desired location, an explosive charge opens the rear of shell and a small parachute pulls out the folded WASP. Once the WASP is de-spun by the parachute, its wings unfold into flight configuration, and the electric motor starts. The WASP is then ready to fly a pre-planned track to gather the needed intelligence.

The WASP concept is intended to fill a specific niche in the spectrum of reconnaissance/surveillance operations. At one end of the spectrum, satellites can provide global coverage. They provide excellent strategic surveillance, but are limited in their tactical usefulness. High altitude systems such as the U-2 and the Joint Surveillance Target Attack Radar System (JSTARS), which comprise the next level in the spectrum, provide theater level coverage. Currently, UAV's such as the Global Hawk and Predator occupy another niche, which is to provide tactical battlefield coverage. The UAV's in use at the present time, however, have a number of shortfalls prompting creation of a new system.

As documented in the WASP Final Report of January 2001 [1], there are a number of shortcomings addressed by the WASP. First, because it is carried in an artillery shell, the WASP can arrive on station in minutes to provide time critical targeting and surveillance. Next, the WASP provides troops at the unit level with a readily available means to see the battlefield. It

does not need take-off and landing facilities, and its small size makes it easily transportable until use. Another advantage of the WASP due to its gun launch capability is the preservation of its energy until it reaches station. Unlike current UAV's, the WASP does not expend its own fuel to reach the target area. Finally, the WASP provides launch platform flexibility. Although it is designed to survive the shock of gun launch, it can easily be used in other low-g applications such as deployment by larger aircraft. Additionally, it can be scaled to fit in smaller shells such as those used in five-inch naval guns.

1.1: Wasp Design Evolution

Since its inception, WASP has been steadily refined to ensure that it meets mission requirements. There have been three major phases in the program.

1.1.1: MIT/Draper Project – WASP I

The original WASP was an aluminum prototype designed by students at MIT [2]. It was constructed to survive a 15,000 g acceleration during launch, and it was scaled to fit a five inch shell used in naval artillery. Although this prototype successfully passed testing to verify it could survive the high-g environment, it was not able to achieve controlled flight. Its aluminum construction was far too heavy.

1.1.2: WASP Phase II

From March 1999 to January 2001 the DARPA sponsored second phase of the WASP program addressed two primary issues: packaging and flightworthiness. During this phase, the majority of the WASP structure was redesigned and fabricated using composite materials. The design was also driven by a more sophisticated set of requirements. Although the assembled aircraft was not tested for g-hardness at this time, the design was meant to be g-hard credible, meaning that components had the potential to survive the extremely high launch accelerations. Previous work showed that composite parts could survive the g-forces experienced during launch. Curved composite panels were tested in high-g conditions to show that using a wing constructed from composite materials was feasible [2]. Composite cylinders that contained holes and slots were similarly tested to analyze the use of these materials in the body section of the WASP [3]. Static testing also verified the integrity of various parts of the design.

As summarized in the final report for this phase [1], a number of design iterations were performed to obtain a flyer with suitable aerodynamic properties. Properties such as the wing shape, structure, and dihedral were altered and each design was wind tunnel tested to determine its performance. Even though the WASP calls for a folding wing, straight wings were constructed for simplicity purposes. To achieve roll control, servomotors were used to actuate small ailerons on these wings. Once a suitable design was found, the aircraft was constructed and flight-testing was performed. This testing culminated in December 2000, when the WASP displayed its ability to sustain powered flight while following a specific flight path. Figure 1.1 shows one of the WASP flight test vehicles.

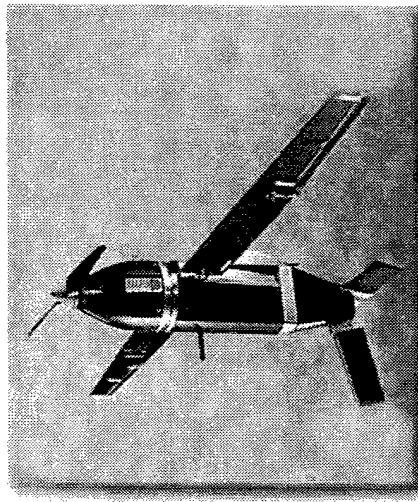


Figure 1.1: Phase II WASP

1.1.3: WASP G-hardening Program

The next task in designing the WASP was to ensure that it could survive the gun launch environment. In a continuation of the DARPA program, each structural component was analyzed and redesigned if necessary to ensure that it could survive the launch and fit into the required artillery shell. Since the previous phase focused mainly on the flightworthiness of the vehicle, many parts that were acceptable for flight-testing were not acceptable for g-hardness. Making the aircraft g-hard involved significant design challenges. First, because of the launch accelerations, adding one pound of weight actually adds approximately 15,000 pounds of load to the structure. Also, many moving parts that were sufficient for the flight test vehicle needed to be eliminated, since they would not survive the launch accelerations. The final report for this

phase details the specific finite element analysis and testing used to verify the structural integrity of the aircraft [4]. Figure 1.2 shows the WASP in flight and launch configurations.

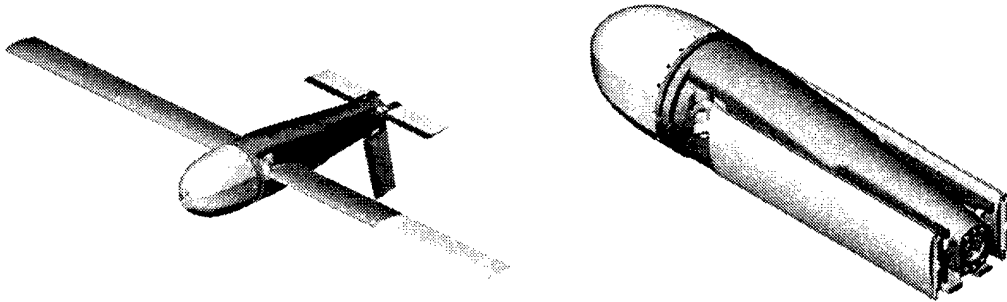


Figure 1.2: WASP in Flight and Launch Configurations

1.2: Roll Control

During the g-hardening phase, it was concluded that the wing design used to control the WASP during flight-testing was not acceptable for the final design. The WASP flyer used small servomotors to actuate ailerons, which provided roll control for the aircraft. This mechanism was unacceptable for many reasons.

First, the WASP uses a folding wing design in order to meet the size constraints of the artillery shell. This posed packaging problems for the servomotors used to actuate the ailerons. While in the folded configuration there was not enough space between the wing panels to accommodate the necessary actuators.

Second, and more importantly, it is unlikely that the mechanical structure of these ailerons would survive the shock of the launch environment. It is very likely that the linkages would either break or be displaced enough to alter the performance of the system. Finally, placing the servos on the exterior of the wing produced excessive drag. For these reasons, the decision was made to investigate other options for roll control.

1.2.1: *Wing Warping*

One alternative to using conventional ailerons is to use a mechanism that twists the entire wing. This concept is known as wing warping. By changing the angle of attack on all or part of one wing, a lift differential between the two wings is created, which will roll the aircraft. If a g-

hard wing warping actuator could be developed, the ailerons would be unnecessary. To explore this option, it was decided that two approaches would be considered.

1.2.2: Piezoelectric Actuation

The first option considered was to use piezoelectric actuators to twist the wing. Piezoelectric materials work by mechanically deforming when exposed to an electric field. As described in a recent MIT thesis, the piezoelectric “patches” were embedded in the composite structure of a WASP wing, and voltage was applied to actuate them [5].

One advantage to using piezoelectric materials to build an actuator is the high bandwidth available. Piezoelectric actuators can be cycled at very high frequencies. On the downside, the magnitude of displacement produced by these materials is not that large. In terms of power consumption, piezoelectric actuators require large voltages, but the current needed to drive them is small. One other drawback to piezoelectric actuators is that they can be brittle.

Overall, it was shown that using piezoelectric materials to actuate the WASP wing was feasible, if care was taken in the manufacturing of the wings, actuators, and necessary electrical circuitry.

1.2.3: Shape Memory Alloy Actuation

The second option considered, which is the subject of this thesis, is to use a class of materials known as shape memory alloys (SMA’s) to build a g-hard wing actuator for the WASP. If deformed at a low temperature, shape memory alloys will return to the original shape when heated past a certain “transformation” temperature. Heating the wires, which is usually done using an electric current, produces a phase change in the material, which causes plastic strain to be recovered.

The most obvious advantage of using SMA’s is the large amount of strain that can be recovered during this transformation, which by most estimates is between six to eight percent. This results in a large stroke, in contrast to that found in piezoelectric actuators. On the other hand, the bandwidth available using SMA’s is not as large. Because they operate due to temperature changes, the speed of actuation is dependant on how fast the wires can be heated and cooled. The power use of an SMA actuator is driven by the amount of current needed to heat the wires, which can be high. The voltage needed to heat the wire, however, is usually very small.

SMA's are often described as having a much higher energy density than piezoelectric actuators, meaning that per unit volume, SMA actuators can produce much more work. One other major advantage to using SMA's is the toughness of the material.

1.3: Thesis Objectives

The goal of this thesis is to develop and test a first-order SMA-actuated wing design in order to simulate the use of this type of actuator on the WASP vehicle. After forming a conceptual design, a series of modeling steps will be taken to refine it. Thermal modeling will be used to determine how fast SMA wires on the wing can be heated and cooled, which will determine the speed of the actuator. This modeling will determine the optimum size wires. Structural analysis will be performed to predict the amount of wing twist resulting from use of the SMA actuator. Once the time and structural responses are known, these will be used in a performance analysis to determine how effective the SMA-actuated wing will be in controlling the aircraft as a whole. After completing the modeling and analysis, a prototype wing will be constructed and tested.

1.4: Thesis Outline

This thesis begins by explaining the fundamental properties of SMA's in Chapter Two. In Chapter Three, previous applications of SMA's are outlined, and relevant results of these studies are discussed. The conceptual design for a shape memory alloy actuated WASP wing is described in Chapter Four. In order to provide a more detailed design for the actuator, Chapter Five describes a number of modeling steps taken during the course of the project. It then explains preliminary analysis of the performance of the WASP using this actuator. Chapter Six explains the experiments done to characterize the specific shape memory alloy wire used in the project, and Chapter Seven contains the details of the construction and testing of a first order prototype of the actuator. The thesis ends with conclusions and recommendations in Chapter Eight.

Chapter 2: Shape Memory Alloy Background

There is disagreement over the first discovery of shape memory alloys. Some sources indicate that the shape memory effect was first seen in brasses in 1938 at MIT and Harvard [6,7]. Others, however, credit Chang and Read with the discovery for their work with gold-cadmium alloys (AuCd), as reported in 1951 [8-10]. The discovery credited with bringing shape memory alloys to their current importance in scientific research was made in 1963 by William J. Buehler and his colleagues at the U.S. Naval Ordnance Laboratory [6,7,9]. Their work focused on the presence of the shape memory effect in equiatomic alloys of nickel and titanium (NiTi). By combining the chemical symbols for those elements with the acronym for their laboratory, they coined the common name for this alloy – Nitinol. In subsequent years, it was also found that the shape memory effect is present in many copper alloys. Eventually it was concluded that the shape memory effect is common to alloys that undergo thermoelastic martensitic transformations [11]. Understanding the basics of this type of transformation is essential to understanding the shape memory effect.

2.1: Martensitic Transformations

There are two types of solid-state transformations: diffusional and displacive [12]. Diffusional transformations occur when a new phase is formed due to the random movement of atoms over long distances. The new phase has a different chemical composition than the original, or parent, phase. Because atomic migration is required, these transformations are dependent on both time and temperature.

On the other hand, displacive transformations happen when atoms cooperatively rearrange into a new, more stable, crystal structure. The chemical composition stays the same, since no atomic migration occurs. The lack of atomic migration also eliminates the time

dependency of this type of transformation. In general, martensitic transformations are displacive transformations. Upon cooling, the low temperature phase (martensite) forms from the high temperature phase (austenite).

To better understand the microscopic effects of the martensitic transformation, it is useful to consider a two dimensional example. Figure 2.1 shows the typical structures of the two phases. Austenite has an ordered rectangular microstructure, whereas martensite molecules appear as parallelograms.

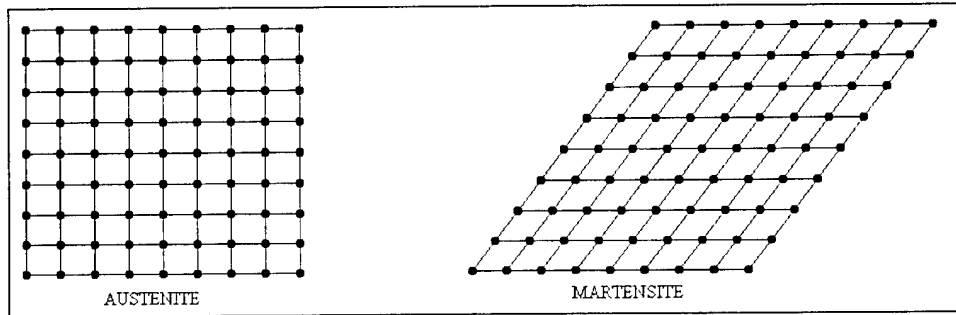


Figure 2.1: Crystal Structures

The transformation from austenite to martensite can be thought of as having two parts: a deformation step and an accommodation step [12]. The deformation step, sometimes called Bain strain, consists of all atomic movements needed to produce the new microstructure from the old. The end result of this lattice deformation is the martensitic structure shown in Figure 2.1. It is evident that the phase change results in a shape change as well.

This shape change poses a problem. As the nucleation and growth process proceeds, martensite forms while being surrounded by austenite. Because of the different shapes, either the surrounding austenite must change shape to allow for the shape of the martensite, or the martensite must be altered to fit within the original space constraints of the solid. It is much easier for the latter to occur, and this process forms the accommodation step of the transformation.

During the accommodation step, there are two possible ways for the martensite to change to a suitable shape. These are known as slip and twinning, and are shown in Figure 2.2 [8,12].

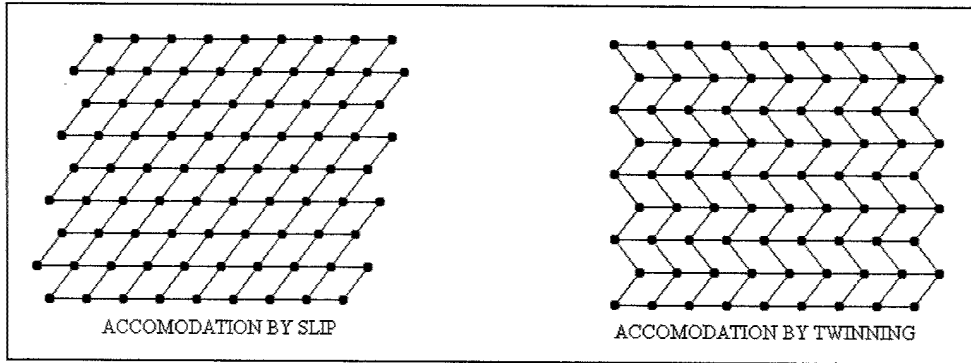


Figure 2.2: Accommodation Modes

As shown, the martensite produced in both accommodation modes occupies roughly the same shape as the original austenite. In many martensitic transformations, the accommodation step consists totally of slip or of some combination of slip and twinning. Since slip involves the breaking of atomic bonds, it is an irreversible process. The accommodation step in shape memory alloys involves only twinning. This is what makes the shape memory effect possible.

2.2: The Shape Memory Effect

Since twinning does not involve the breaking of bonds, the twinned microstructure can respond easily to applied stresses. An applied shear stress simply results in the different orientations (called twin variants) reordering to respond to the stress. This produces a macroscopic shape change. The process of combining different twin variants into a single variant is called detwinning. This process is shown in Figure 2.3.

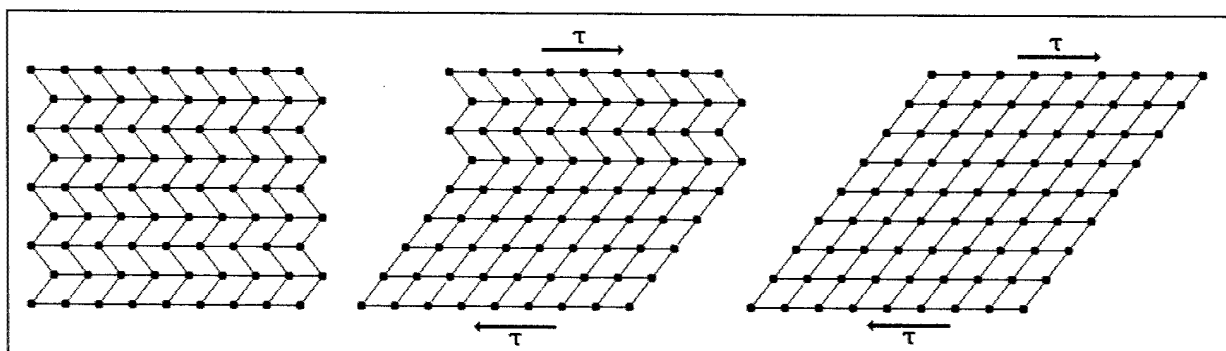


Figure 2.3: Detwinning

This two dimensional model shows that two possible twin variants exist for the martensite phase: parallelograms skewed to the left or right. In austenite, however, only one variant exists – squares. If martensite, in either the twinned or detwinned configuration, is heated to produce the reverse martensitic transformation, only one shape can result – the original austenite microstructure of rectangular molecules from Figure 2.1. This is the basis for the shape memory effect. Since the detwinned martensite configuration corresponds to a macroscopic deformation, the deformed shape must return to the undeformed shape when the material is heated to the austenite phase.

The shape memory effect is illustrated in Figure 2.4. When austenite (a) is cooled, twinned martensite (b) forms. The twinned martensite has a different microstructure, but the same overall shape as the austenite. If stress is applied, it deforms the martensite into a single variant (c) through detwinning, which has a different overall shape. Upon heating, the deformed martensite returns to the original shape and austenite microstructure.

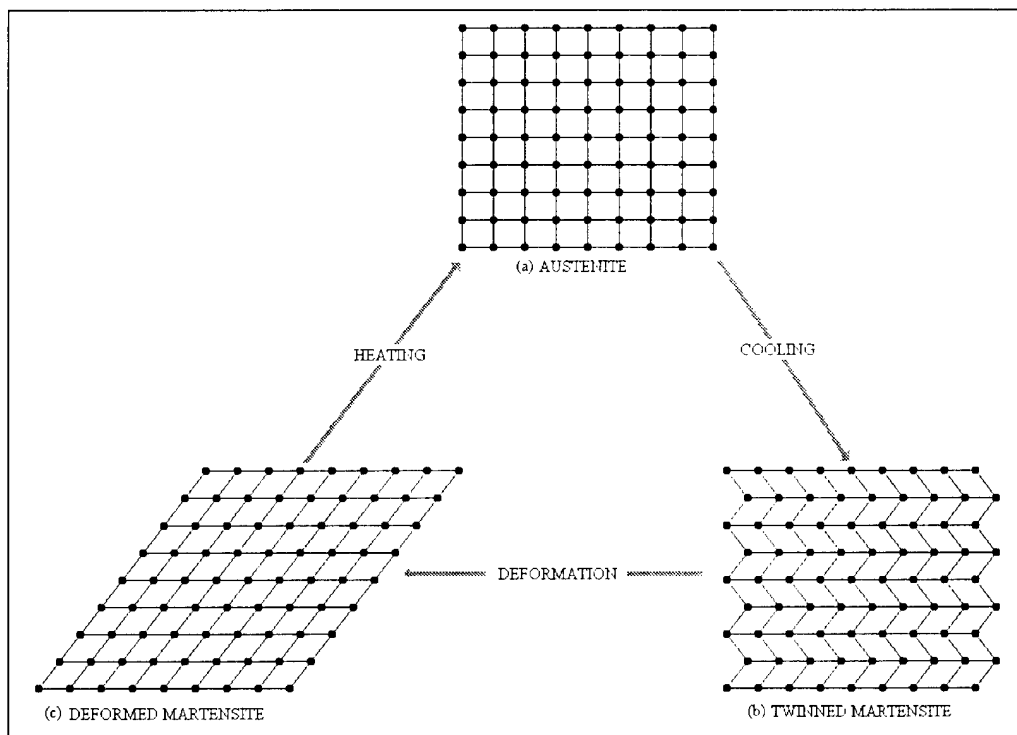


Figure 2.4: Shape Memory Cycle

The shape memory effect shown above is referred to as one-way shape memory. It is only observed when martensite is heated to form austenite. Heating either the twinned or

deformed martensite in Figure 2.4 (b) or (c) will result in the same austenite structure. On the other hand, when austenite is cooled to form martensite, only the deformed shape of Figure 2.4 (b) will be produced. External stress must be applied to get to the structure of Figure 2.4 (c). In this one-way shape memory, only the shape at high temperature, shown in Figure 2.4 (a), is “remembered.” This shape memory effect is the basis for the work done in this thesis.

2.3: Stress-Strain Behavior

As stated earlier, an applied shear stress results in detwinning of the twin variants. However, at some point no more detwinning is possible and the material begins to behave as a normal metal. Increased stress produces the stretching of bonds (elastic deformation) and then the breaking of bonds and movement of dislocations (plastic deformation). The result is the interesting stress-strain curve of shape memory alloys when in the martensitic phase.

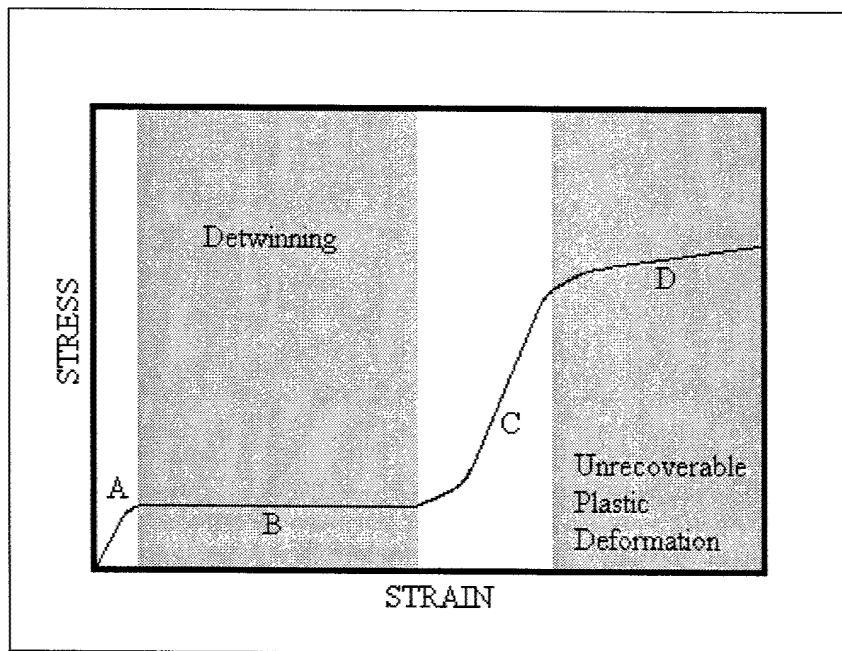


Figure 2.5: SMA Martensitic Stress-Strain Curve

As shown above, the stress-strain curve has four major regions. Region A represents normal elastic strain. Region B is the range in which detwinning results from applied stress. The border between regions B and C is the point at which the material has completely

detwinned. Region C is the second area of elastic strain. Finally, region D shows the area of plastic deformation due to dislocation motion.

Understanding this stress-strain relationship is essential to properly utilizing shape memory alloys. Plastic deformation in region B is recoverable via the shape memory effect described in Section 2.2. Deformation in region D, in contrast, is not recoverable. For Nitinol, the maximum amount of recoverable strain is normally listed at around eight percent. In this thesis, the strains used will be significantly lower than this, in order to prevent any danger of inducing permanent deformation.

2.4: Transition Temperature and Hysteresis

The temperatures at which the martensitic (cooling) and reverse martensitic (heating) transformations occur are not the same. Furthermore, the transformations do not occur instantaneously, but rather over a range of temperatures. Figure 2.5 illustrates these facts. In the figure, M_f , M_s , A_s , and A_f stand for the martensite finish, martensite start, austenite start, and austenite finish temperatures, respectively.

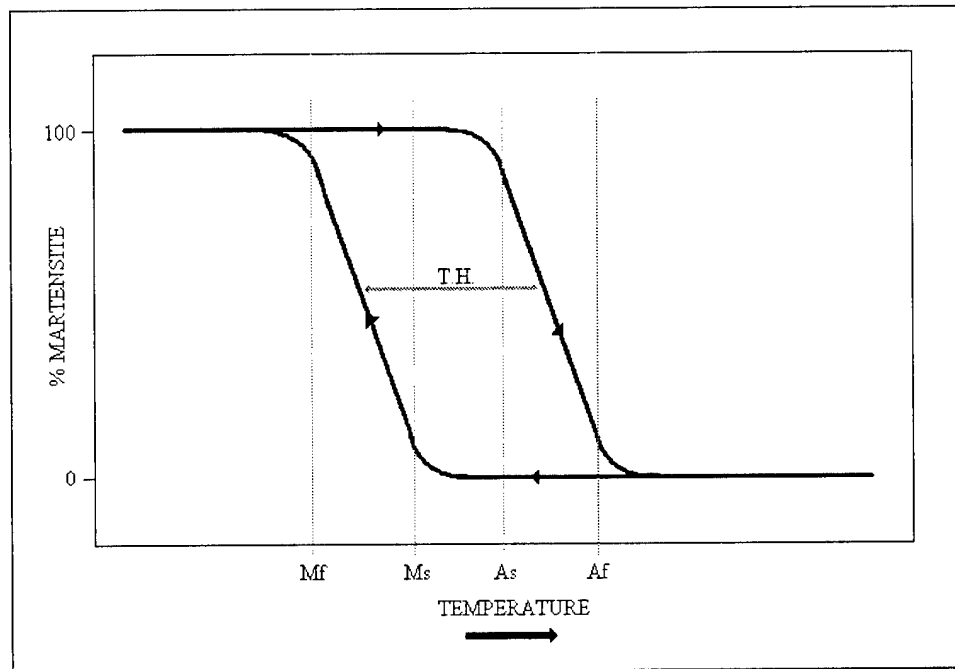


Figure 2.6: Transformation vs. Temperature Curve

If the material was cooled below M_f and then heated, transformation to austenite would not begin until the temperature reached A_s . At temperatures in between A_s and A_f there would be a mixture of austenite and martensite, as shown above. Similarly, if the material was heated past A_f and then cooled, transformation to martensite would not begin until the temperature reached M_s .

The abbreviation T.H. in Figure 2.6 represents the temperature hysteresis, which is the difference between the temperatures at which the forward and reverse transformations occur. The transformation temperatures and hysteresis for a shape memory alloy can be altered by changing the percentages of elements in the alloy or by adding additional alloying elements. As a general rule, it is desirable to use SMA's with as small a hysteresis as possible.

In this thesis, assumed values for these transition temperatures were used during the modeling stage described in Chapter Five. In Chapter Six, experimental determination of these temperatures is explained.

2.5: Material Properties

The martensite and austenite phases of a shape memory alloy have very different material properties. Most notably, there is a significant increase in both modulus of elasticity and yield strength when the SMA is heated from martensite to austenite. Typical value ranges for Nitinol are shown below [9].

Table 2.1: Nitinol Material Properties

Property	Martensite Value	Austenite Value
Modulus of Elasticity (E, psi)	4×10^6 to 6×10^6	10×10^6 to 12×10^6
Yield Strength, (σ_y , ksi)	10 to 20	28 to 100

Taking advantage of these property changes can be very useful when designing actuators and systems using SMA's. This will be discussed further in Section 2.8.

2.6: Two-Way Shape Memory

As previously mentioned, normal shape memory will not "remember" a deformed shape in the low temperature (martensite) phase. In two-way shape memory (TWSM), on the other

hand, distinct shapes are remembered for both phases. As the alloy is heated and cooled, the shape will alternate between the low and high temperature shapes, as shown in Figure 2.7.

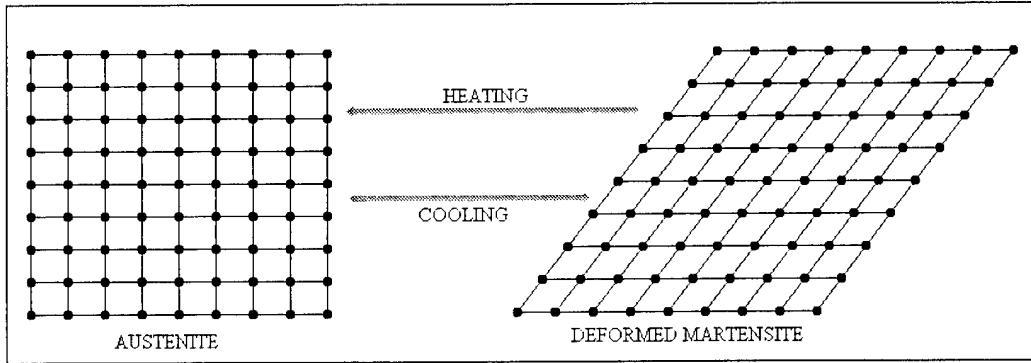


Figure 2.7: Two-Way Shape Memory

In order to obtain TWSM, the alloy must be thermomechanically treated using a process known as training. There are a variety of methods to accomplish this training of the alloy, but all are based on the same principle. Training processes for TWSM produce small internal stresses on the microscopic level in the parent austenite phase [6,12]. When the alloy is cooled, these stresses cause the transformation to proceed directly to the structure shown in Figure 2.4 (c), while completely bypassing the twinned configuration normally produced during the accommodation step. The internal stresses caused by training essentially bias the formation of martensite to favor one of the twin variants over the other, allowing a deformed shape to be “programmed” for the low temperature phase as well [12].

2.7: Stress-Induced Martensite and Superelasticity

Up to this point, only martensitic transformations due to temperature changes have been considered. Stress can also cause austenite to transform to martensite. At temperatures above M_s , martensite can be made stable by applying stress to the material, but it will be unstable if the stress is removed [12]. The stress needed to produce martensite above M_s increases as temperature increases. Because of this, there is a temperature at which the stress needed to create martensite is actually enough to break the atomic bonds in the material. This temperature is called M_d .

Superelasticity, which is sometimes also called pseudoelasticity, is seen when an SMA is deformed at a temperature above A_s but below M_d . The stresses cause single variant martensite

to form, and the material strains. When the stress is removed, the martensite variants return to austenite, and the deformation is recovered. This phenomenon, which causes the material to be extremely elastic, is shown in Figure 2.8.

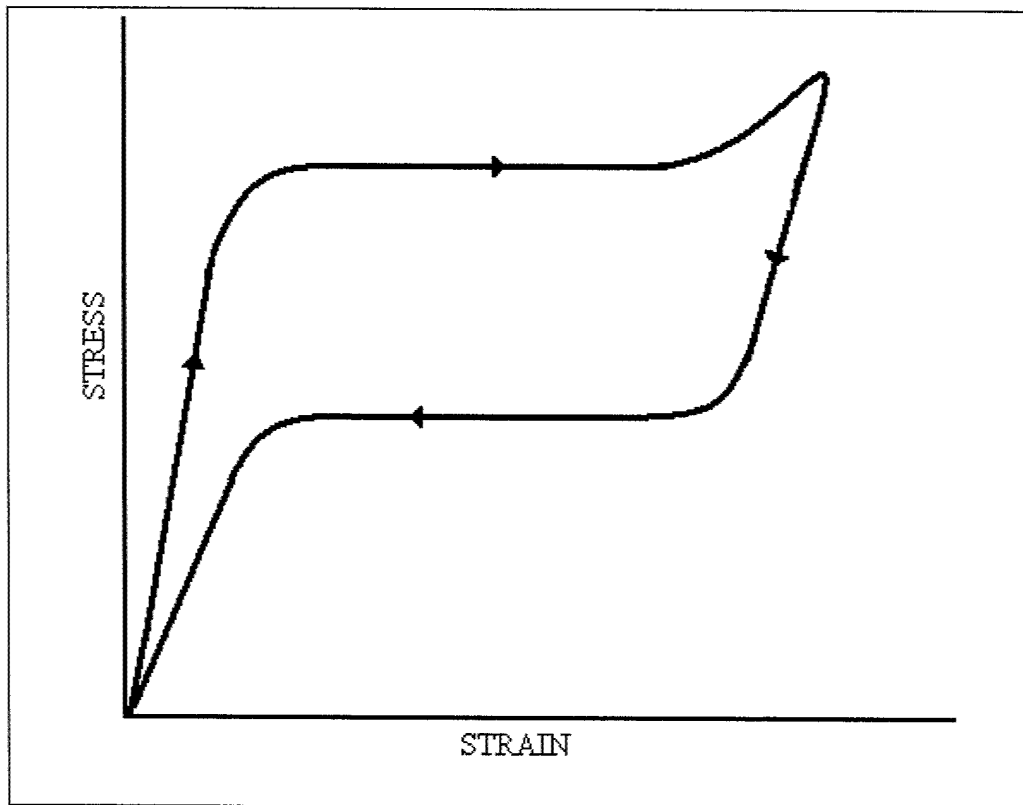


Figure 2.8: Superelasticity

Although the property of superelasticity will not be utilized in this thesis, the idea of stress-induced martensite will be important in describing results of materials testing. This testing will be described in Chapter Six.

2.8: Two-Way Systems

Instead of training shape memory alloys to be two-way by themselves, it is also possible to obtain a “system” two-way effect by combining regular one-way SMA’s with springs, weights, or other parts. There are two approaches to doing this, each of which exploits the difference in strength and stiffness between the high and low temperature phases [11].

The first is known as the bias technique. In this technique, a shape memory spring or wire can be combined with another spring or weight, which provides a bias force. In the low temperature condition, the bias force deforms the shape memory alloy. As the temperature of the alloy increases and reaches A_s , the alloy changes back to the parent austenite phase and returns to its original shape.

The second technique is called the differential technique. Instead of combining a shape memory alloy with a conventional spring or weight, two shape memory alloys are combined to act against each other as an antagonistic pair. For example, two shape memory alloy springs with equal stiffness could be compressed equal amounts and placed in series. If one of the springs is heated, and the other remains at the low temperature, the heated spring will increase in stiffness, which will result in it extending. The other spring will compress until a new equilibrium is reached. This forms one memorized state of the system. The other is when the opposite spring is heated and equilibrium is reached in the opposite direction. Two simple SMA wires can also be used in this manner. When one contracts, it provides the force necessary to deform the other, and visa-versa.

These two techniques are seen repeatedly in current SMA actuator technology. They will also be used as the starting point for the conceptual design in this thesis.

Chapter 3: Previous Applications of Shape Memory Alloys

A tremendous amount of work has been done concerning the application of shape memory alloys in recent years. Although none of this work directly involves designing a shape memory alloy actuator for a small UAV wing, many previous studies illustrated problems and techniques for using shape memory alloys that are related to this thesis. This chapter outlines portions of this work that are significant to this thesis.

3.1: Shape Memory Alloy Composites

One significant area of study has been in the field of composite materials. Several efforts have been made to embed SMA's in composites, and these have yielded an abundance of important information.

Many of the initial experiments with SMA composites were done to investigate the possibility of using the properties of SMA's to control the dynamics of beams or other structures. Liang, Jia, and Rogers investigated embedding Nitinol wires in a graphite/epoxy composite beam to control vibration and alter natural frequencies [13,14]. Resistive heating was used to trigger a phase change in the wires. In order to build the SMA composite beams, pre-strained wires were included in the initial lay-up, and they were constrained to prevent them from changing shape during the curing process. Rogers lists various methods for controlling vibration in the beam. In transient vibration control, SMA wires are placed off the neutral axis, and actuated in an antagonistic manner. This provides force to reduce vibration.

Another method, called structural tuning, involves heating an undeformed SMA wire in the structure to take advantage of the stiffness change when the SMA transforms from martensite to austenite. Finally, active strain energy tuning involves placing pre-strained SMA wires on

opposite sides of the neutral axis. When the wires are actuated together no deformation results, but a residual state of stress is formed when the wires “try” to contract. This stress changes the dynamic properties of the beam.

Baz et al. similarly used SMA wires to control the vibrations of a flexible cantilevered beam [15]. Instead of including the SMA wires in the original lay-up, mechanical fasteners were used to connect the wires to the beam after the curing process was completed. Although this worked, it did add weight to the structure. This study demonstrated that enhanced cooling of the wire could be obtained by only partially embedding the wire in the composite.

The work of Bidaux et al. focused on epoxy beams that contained Nitinol wires embedded along the neutral axis [16]. These wires were also constrained during the curing process to maintain their pre-strain. This study found that the SMA wire could be resistively heated to control vibration, but it also found that using wires with a smaller pre-strain enhanced the durability of the bond between the wire and the epoxy. Balta et al conducted a similar study to analyze the effectiveness of using NiTiCu wires [17]. Along with detailing the vibrational control properties of the SMA wire, it found that the surface preparation of the wire plays a significant roll in determining the quality of the bond between the epoxy and SMA wire. Specifically it found that having an oxide coating on the wire enhanced the bond strength.

Several other studies have been completed to optimize the actual process of producing SMA composites. In the previous studies, one-way SMA’s were used, which necessitated the use of some constraining device during the cure cycle of the composite. White et al. and Hebda et al. noted that there are often significant problems with the resulting bond between the SMA wires and the surrounding epoxy [18,19]. They proposed the utilization of the two-way shape memory effect to solve this problem. Since wires with two-way memory will expand upon cooling, there is no need to constrain them during the curing process to prevent them from contracting. These studies outlined a method for training the SMA wire to obtain two-way shape memory, and they investigated the growth of voids around the SMA wires. Consistent with other research, it was found that sacrificing recoverable strain in the wire could be necessary to assure that the wires stay bonded after the curing process.

A third area of study related to SMA composites is the analysis of the structural deformation that can be obtained using embedded SMA wires. Hebda and White, using the previously mentioned manufacturing techniques, constructed composite beams with SMA wire

having a 1.5 percent recoverable strain [20]. This study found that when the SMA wires were resistively heated, the addition of heat into the beam caused deflection due to the coefficients of thermal expansion of the beam materials. As the SMA wires reach the transition temperature, the SMA induced deflection overshadowed the thermally induced deflection.

Song et al. also found that embedding SMA's in composite beams provided a reliable means to precisely control the position of the beam [21]. They were able to develop a simple controller to move the tip of the beam to a desired position with no overshoot.

3.2: Shape Memory Alloy Wire Actuators

Another major group of applications involves the use of SMA wires that are not embedded in any type of matrix. Rather, the ends of the wires are connected to a structure, and the wires serve as discrete actuators designed to create movement in the structure. While not dealing directly with the use of SMA's with a composite wing, these studies shed light on the use of SMA's as actuator devices, and therefore illustrate important details to consider in this thesis.

Much of the work in this area has been centered in the field of biomimetics. One such program is the underwater robot program led by Dr. Joe Ayers at the Northeastern University Marine Science Center. As documented by Whiting et al., SMA actuators have been developed to act as muscles for an ambulatory robot modeled after the American lobster [22]. Each muscle consists of a 250-micron diameter Nitinol wire. The ends of each wire are formed into a small loop using a metal crimp. Kevlar strings are tied to these loops, and then these strings are tied to the "skeleton" of the robot to attach the SMA wire to the structure. To insulate the wire from the outside water environment, a plastic sleeve encapsulates the entire muscle. The crimps also serve as points for electrical connection. Much like the way muscles work in natural organisms, the Nitinol wires are used in antagonistic pairs. When one contracts, it provides the force necessary to extend the other (this is the differential approach to two way shape memory described in Chapter Two). Each leg of the lobster contains 3 pairs of SMA muscles. To contract the muscle, current pulses are sent through the wire. The water surrounding the robot then cools the wire so the antagonistic muscle can deform it.

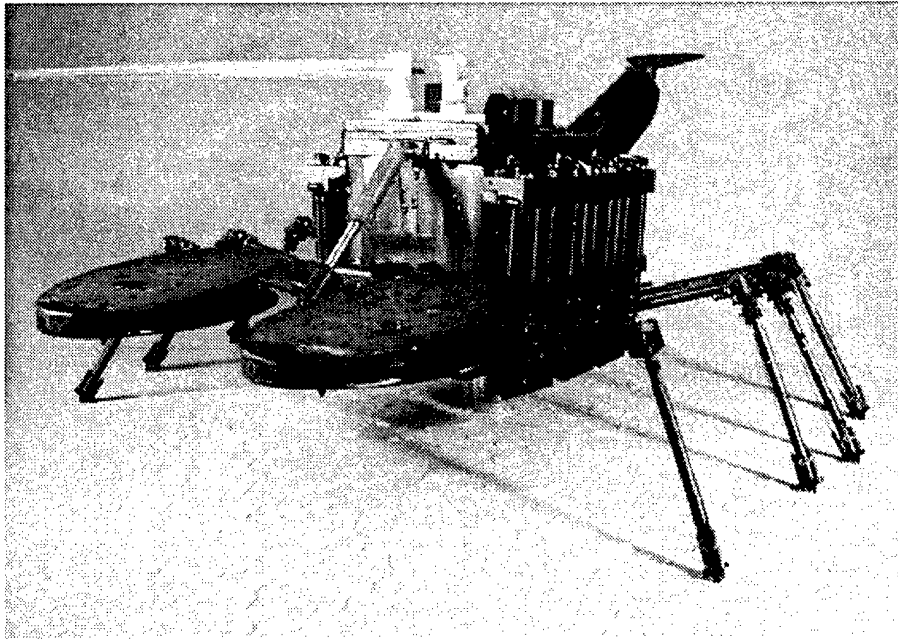


Figure 3.1: Lobster Robot

Rediniotis et al have developed an SMA actuated biomimetic hydrofoil [23,24]. The biomimetic hydrofoil has a skin that is supported by a backbone and rib skeleton, as shown below.

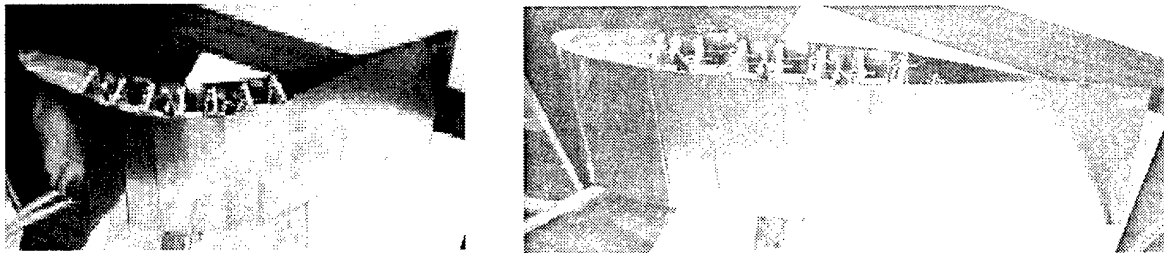


Figure 3.2: Biomimetic Hydrofoil

Shape memory alloys were chosen as actuator materials because of their large energy densities, compared to piezoelectric and other materials. They used NiTiCu wires with a diameter of 60 microns. In this application, the SMA actuators were also used to mimic muscles. However, a different technique was used. Instead of using two antagonistic SMA wires, a bias spring is used to provide the restoring force for the SMA wire. Each SMA wire was attached to the skin of the hydrofoil using a Kevlar tendon.

Initially, one-way SMA wires were used, but this meant that the bias springs had to exert enough force to deform the wire. The wires were replaced with two-way trained wires, which means that the wires will re-extend as soon as they cool. This means that the springs are only needed to overcome internal frictions in the hydrofoil. For this reason, a much smaller spring is adequate.

Since the underwater environment is variable, the SMA wires are contained in isolated cooling channels. A fluid flows through this channel, and this fluid is monitored so as to actively control the temperature in the environment around the SMA wire. By actively controlling the temperature of the SMA wire, actuation frequencies up to 20 hertz were achieved. Actuation frequencies of this magnitude are commonly thought to be unobtainable when using SMA actuators, so this research is groundbreaking.

Not all SMA actuators are used in biomimetic devices. Strelec and Lagoudas fabricated and tested an SMA actuated wing [25]. This wing used two-way trained SMA wires. Heating and cooling were done through resistive heating and natural convection, respectively. This study showed that SMA wires could be used to change the shape of a large scale airfoil and thus change its aerodynamic performance.

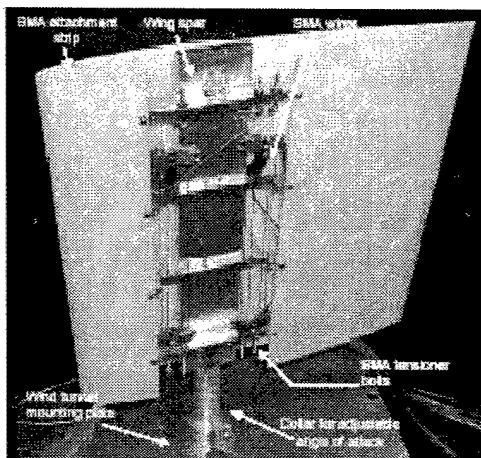


Figure 3.3: SMA Actuated Wing

3.3: Large Scale SMA Actuators

Many SMA actuators are not constructed from wire. The DARPA Smart Wing program has investigated the use of SMA torque tubes to induce wing warping in a full-scale aircraft wing [26,27]. This torque tube is designed to replace electric or hydraulic torsion actuators. The

stiffness of the wing box acts as a bias spring to provide restoring force to the torque tube, which is pre-strained before it is installed.

An important difference between this concept and those using SMA wire is the method of heating the actuator. Unlike in wire actuators, direct resistive heating was found to be inefficient in terms of both uniformity of heating and power consumption. For this reason, heat was added by wrapping the torque tube in heater wire.

In terms of aerodynamic performance, this program has shown that SMA actuation can provide wing twist sufficient to create the roll moments needed to control the aircraft. Additionally, this study has shown that the use of hingeless control surfaces increases lift and decreases drag by delaying flow separation on the wing.

Chapter 4: Conceptual Design

This chapter begins by describing the design of the WASP wing, and then outlines the basic concept for an SMA actuator for this wing.

4.1: Wasp Wing Design

During WASP Phase II, the shape and size of the wing were finalized and wind tunnel tested to ensure that it met the aerodynamic requirements of the aircraft. This design was improved during the g-hardening program, and a structurally sound wing was constructed and tested. Hinges were designed to allow the wing to fold into the proper launch configuration while contained inside the artillery shell. Figure 4.1 shows the WASP wing in flight and launch configurations.

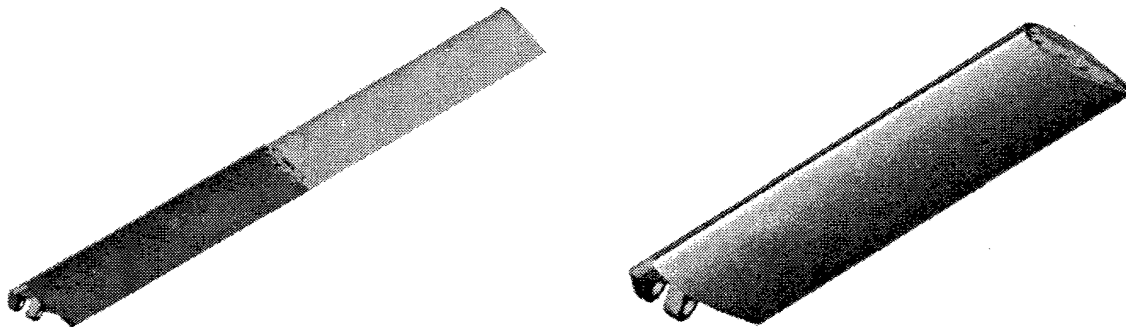


Figure 4.1: WASP Wing in Flight and Launch Configurations

The wing design calls for each wing to be constructed of two 11-inch long panels, which are separated by a mid-span hinge. The wing has a chord length of 2.85 inches. The core material of the wing is a Nomex honeycomb. The wing skin is composed of two layers of

fiberglass/epoxy composite prepreg. The inner layer is a 0/90 weave, while the outer layer is a unidirectional layer with fibers running along the span of the wing. It should be noted, however, that the materials and lay-up of the wing could be changed, as long as the shape of the wing is not altered.

4.2: Design Approaches

The basic concept for the SMA actuated UAV wing is to attach Nitinol wires to the outside surface of the wing using an epoxy or other high strength adhesive. To impart a twisting motion, the wires must be placed at a 45 degree angle to the wing span axis, since the fibers in the wing are all either parallel or perpendicular to the span (if the lay-up is changed, a different wire angle may be used to impart a twisting force). The force transferred to the wing when the wires contract will cause a torsional deflection of the wing. This will change the wing's angle of attack, thus creating a roll moment. To heat the Nitinol wire, resistive heating is used. Since the wire is on the outside surface of the wing, cooling occurs predominantly via forced convection caused by the passing air stream.

Essentially, the basic SMA actuator design must be a two-way system. There must be two memorized states: the normal flight configuration (zero degrees angle of attack (AOA)) and the roll configuration where the wing is twisted. Since extensive training of the wire is needed to obtain a two-way memory in the wire itself, it is desirable to use one-way shape memory for this design. Given this framework, there are two possible approaches, as discussed in Section 2.8. Both of these approaches will be investigated with analysis and testing.

4.2.1: *Bias Approach*

The first approach utilizes the bias technique of obtaining a two-way system. Pre-strained Nitinol wires are placed on either the top or the bottom of the wing, and the torsional stiffness of the wing is used as the bias spring to provide the necessary restoring force. When the wires are heated the wing will twist. When the wires cool, the stiffness of the wing will cause the wires to be deformed and the wing will return to normal configuration. For this approach to work, the torsional stiffness of the wing must be sufficient to deform the Nitinol wires when they are in the martensitic phase. At the same time the wing must be flexible enough to be twisted when the Nitinol is heated to its austenite phase.

4.2.2: Differential Approach

The second approach uses the differential technique. Instead of having no Nitinol wires on the bottom of the wing, unstrained wires are added to that side. Now when the top wires are heated, they will contract. This will create a wing twist, but it will also result in a deformation of the unstrained wires on the bottom. To return the wing to normal configuration, the bottom wires are heated, they contract, the top wires are stretched again, and the wing twist is removed. It is important to note that the top wires must be cooled to below the martensite finish temperature before the wing can be untwisted. If deformation occurs in the top wires while they are still austenite, this deformation will be permanent, and the actuator will be rendered useless.

In both of these approaches, the wing twists in only one direction. Therefore, the actuation and recovery of one wing results in the aircraft stopping at a particular bank angle when the roll rate returns to zero. For the aircraft to return to level flight, the other wing must be actuated and recovered to produce a roll in the opposite direction.

4.3: Design Concept

Because of the folding wing design, any wires needed for an actuator on the outboard panel must traverse the mid-span hinge. This would most likely necessitate them being exposed to the outside air stream which could stress them and cause drag. A service loop is also needed to accommodate the folding wing if actuators are included on the outboard panel. Furthermore, any wing twist that is imparted in the inboard panel will result in a constant angle of attack for the outboard panel, assuming that twisting the wing does not add dihedral. For these reasons, an initial decision was made to place the SMA actuator on the inboard panel only.

To produce enough force to twist the wing, several wires must be placed at a 45 degree angle. There are several ways to accomplish this. One is to use several short wires. Another is to bend a long wire into the desired pattern. These options are shown below.

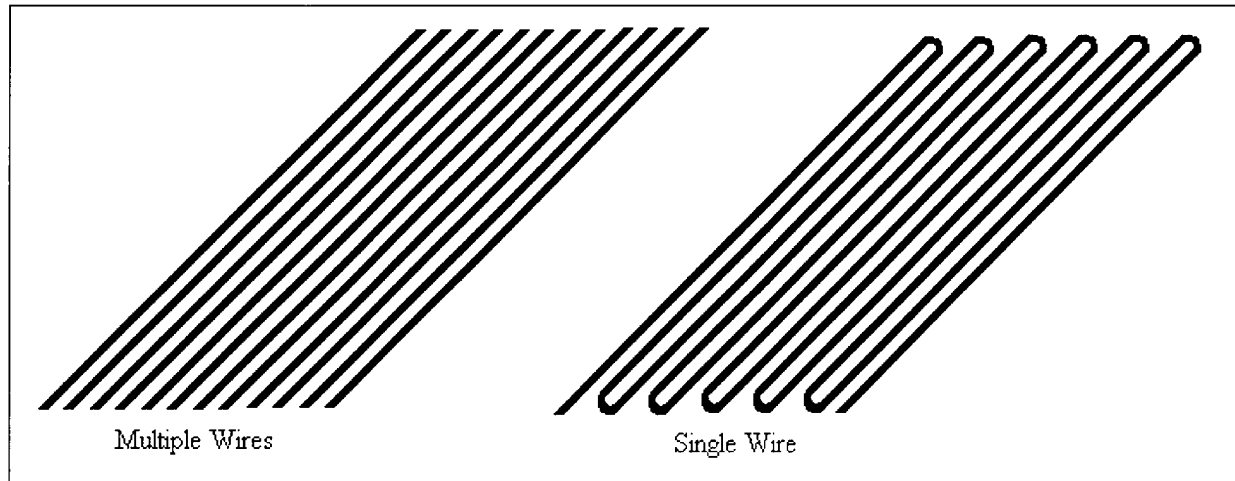


Figure 4.2: Wire Options

For simplicity reasons, the single wire option was chosen. This means that only two terminal connections are needed to heat the wire in the actuator. When the wire is placed on the inboard panel of the wing, the conceptual design looks as follows.

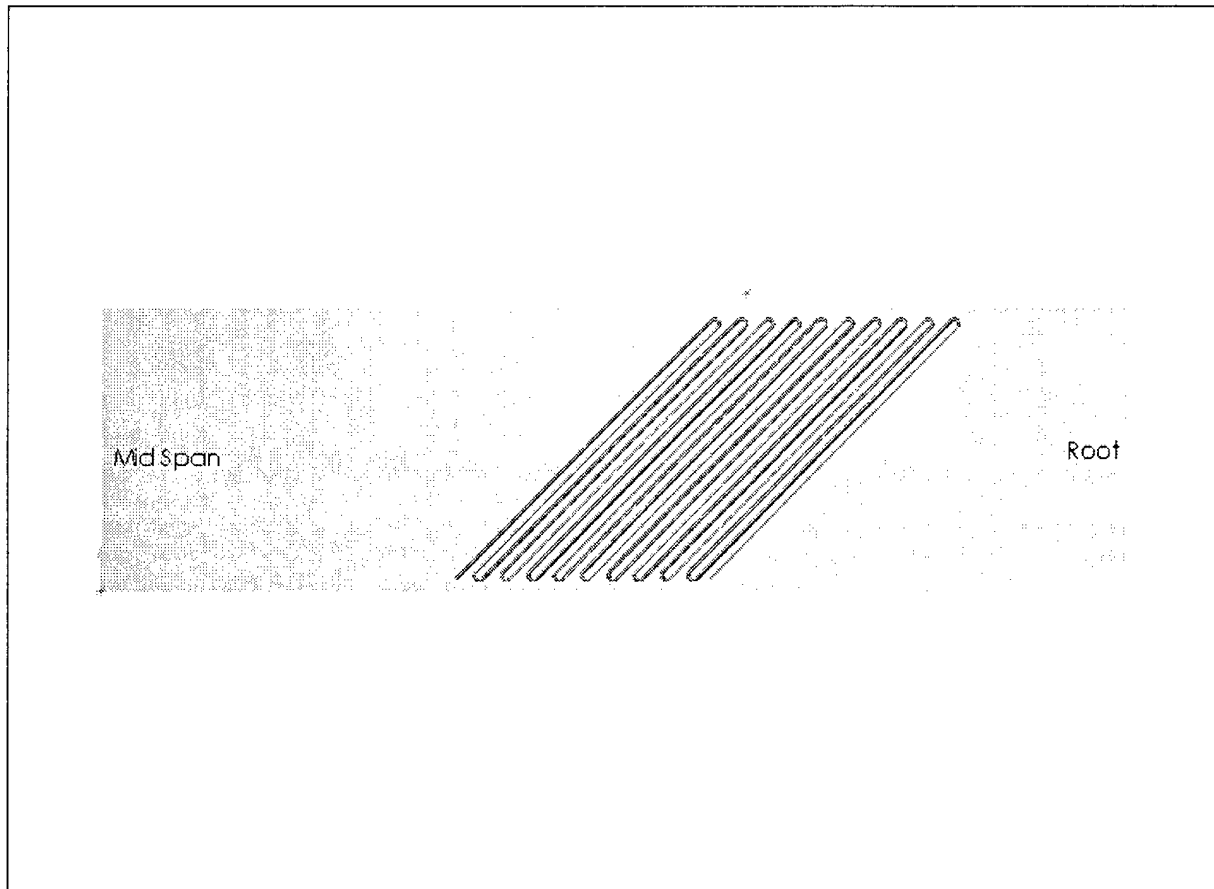


Figure 4.3: Conceptual Design

For the differential approach, the same wire pattern must be placed on the opposite side of the wing as well. The exact orientation of the wires was chosen based on which side of the wing the wires were located as well as the desired twist angle. In order to prevent stalling, it was decided that the wing should be twisted to a negative AOA to produce the roll moment. This means that wires on the top of the wing must be oriented at a positive 45 degree angle. It should be noted that if the bias approach was used and it was desired to have the wires on the bottom of the wing instead, they would need to be at a negative 45 degree angle.

Figure 4.3 shows one possible configuration for the wire, but there are several possibilities. These configurations will be analyzed in Chapter Five to determine which one is most suitable for the WASP wing.

[THIS PAGE INTENTIONALLY LEFT BLANK]

Chapter 5: Modeling and Analysis

In order to refine the conceptual design, a series of finite element models were constructed using ANSYS, a commercially available finite element analysis program. The goal of the modeling stage was to determine specifics of the design that would make it most suitable for use on the WASP wing. The modeling explained in this chapter helped to predict the effectiveness of the actuator in terms of both its time response and its ability to cause mechanical movement in the wing. A preliminary performance analysis was also conducted to predict the response of the aircraft if an actuator of this type was implemented. This chapter will explain the assumptions and simplifications used to model the wing as well as the results of the model solutions and performance analysis.

5.1: Thermal Modeling

As stated before, the time response of the shape memory alloy actuator is dependant on how fast the wires can be heated and cooled. For this reason, analytical solutions were sought to indicate how wire size and surrounding material affect the bandwidth of the actuator.

5.1.1: Single Wire Model

Before considering wires connected to the surface of the wing, a simple model of one Nitinol wire was constructed in ANSYS. The wire's cross-section, a circle, was first created. This geometry was then meshed using PLANE55 elements. These elements contain three nodes and each node has a single degree of freedom – temperature. A plot of the model is shown below.

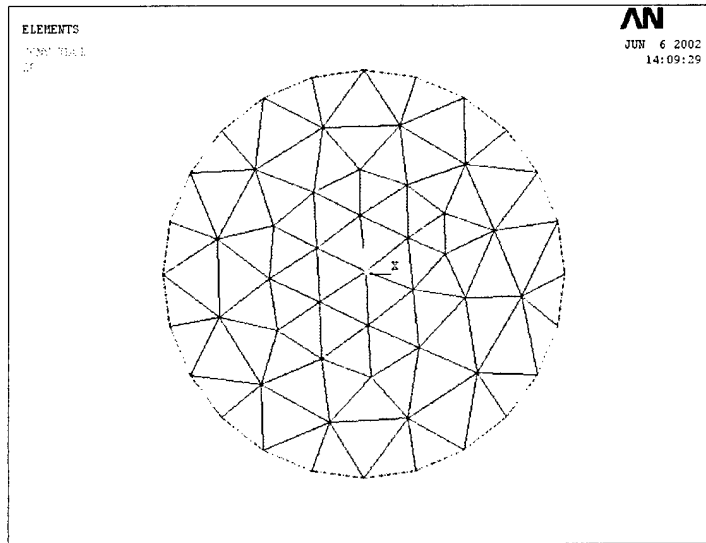


Figure 5.1: Finite Element Model of Single Wire

Each element was set to contain the material properties of Nitinol. For this analysis, the thermal properties used were those of Nitinol in its martensitic phase.

Table 5.1: Nitinol Thermal Properties [28]

Property	Value
Thermal Conductivity (W/m-C)	8.6
Specific Heat (J/kg-C)	322
Density (kg/m ³)	6450

In order to model the heating of the wire due to the electric current, a heat generation load was used in ANSYS. This load was applied to the entire area of the wire. By placing an equal heat generation on the entire circular area, the model assumes that the wire is uniformly heated throughout its cross-section. This is a reasonable assumption, since the wires have a relatively small cross-sectional area. To determine the value for the heat generation rate in ANSYS, simple calculations were performed in a spreadsheet. The resistance of the wire was calculated using Equation 5.1.

$$R = \rho \frac{L}{A} \quad (5.1)$$

In this equation, ρ is the resistivity of the wire, L is the length of the wire, and A is the cross-sectional area of the wire. Next, the power generated in the wire was calculated using Equation 5.2, where I is the current applied to the wire.

$$P = I^2 R \quad (5.2)$$

Finally, the heat generation rate was calculated by dividing the power generated in the wire by the total volume of the wire, as shown in Equation 5.3.

$$H.G.R = \frac{P}{AL} \quad (5.3)$$

In the above equations, the resistivity of the Nitinol was assumed to be 80×10^{-8} ohm - m. The current was set at 20 MA/m^2 to avoid overheating the wires. In the end, since the maximum applied current is a function of area, manipulation of the above equations shows that the heat generation rate for the Nitinol wires is independent of the length of the wire. The heat generation rate calculated using this method was $3.2 \times 10^8 \text{ W/m}^3$.

Applying this model in ANSYS within a transient analysis illustrated how fast the wire would heat when perfectly insulated, assuming that all power was used to heat the wire. To gain insight on the heating and cooling response of the wires when not perfectly insulated, a series of models were constructed to analyze different diameter wires when exposed to a moving air stream. The convection was modeled in ANSYS by applying a film coefficient of $50 \text{ W/m}^2\text{-C}$ and an ambient air temperature of 20 degrees Celsius to the circumference of each wire. This convection coefficient was an estimate of the affect of the aircraft flying at 60 mph, or 26.8 m/s.

For each model and wire diameter, the first step in determining the thermal response solution was to define the load steps to be solved. The first load step contained the initial conditions, the heat generation load, and the convective boundary condition. This load step represented the resistive heating of the wire. The initial condition of the model was a uniform temperature of 20 degrees Celsius. The second load step, which used the results of the first load step for its initial conditions, applied only the convective boundary condition. This represented the cooling period. For each load step, a time was specified to indicate how long the load step was applied, and time stepping options were set for the transient analysis. To find the total cycle time for each model, two runs were necessary. First, the model was solved to determine how much time was required to heat the wires to 100 degrees Celsius, which was assumed to be the A_f temperature for the wire. This time was then used as the limit for how long the first load step was applied in the second run. The second run was performed, and the total time response of the wire temperature was plotted. Figure 5.2 shows a typical temperature vs. time graph for the wires.

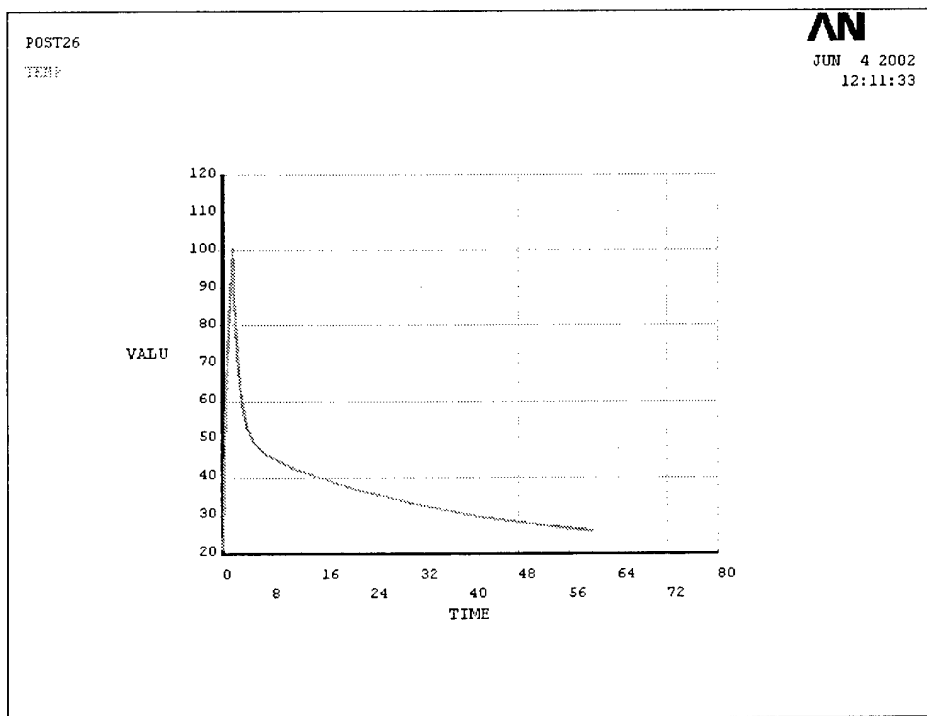


Figure 5.2: Typical Temperature Response of Nitinol Wires (Time in seconds, Temperature in degrees Celsius)

The amount of time needed for the wire to heat to 100 degrees Celsius and then cool to 70 degrees, which was assumed to be the M_f temperature of the wire, was recorded for each wire size. The results are shown below.

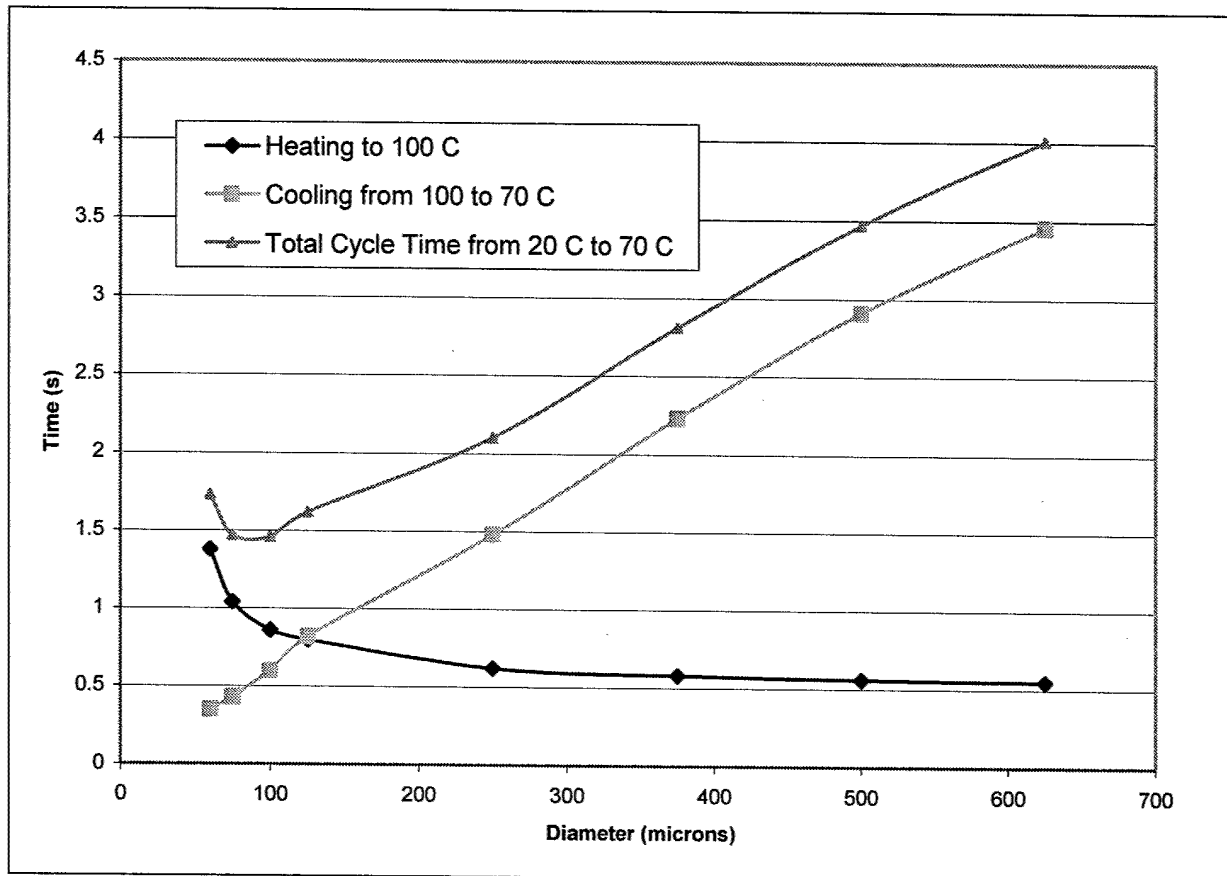


Figure 5.3: Plain Wires Exposed to Forced Convection

There are several notable trends indicated by the graph. First, as the wire diameter increases, the time elapsed while heating the wire to 100 degrees decreases. This can be explained by the presence of the convective boundary condition. For smaller wires, the convection has a larger effect on the heating of the wire. In fact, the steady state temperature reached for extremely small wires will not even reach 100 degrees, since the convective cooling dominates the resistive heating in the wire. Second, as the wire diameter increases, the time needed to cool the wires to 70 degrees increases. This is reasonable, since smaller wires have a larger circumference per unit area ratio. When the heating and cooling times are added, the result is a minimum value for diameters between 75 and 100 microns. Wires of this diameter take the shortest time to heat from 20 to 100 degrees and then cool to 70 degrees, which represents the total temperature cycle needed to repeat the shape memory effect.

5.1.2: Wing Section Model

When the Nitinol wires are attached to the wing, the cooling of the wire happens because of both convection and conduction. As air passes over the wires, the wires are convectively cooled as in the previous model. In addition, conductive cooling takes place due to the heat transfer between the wires and the material that contacts them. Since the cooling of the wires is highly dependent on the material that surrounds them, it was necessary to consider the entire wing thickness in the thermal analysis. The thermal properties of the composite skin, core, and the polymer that surrounds the SMA wires were taken into account.

For this analysis, two possible configurations were considered. The first is when the SMA wires are completely enclosed in a polymer of some type, such as Kapton or an epoxy adhesive. The second configuration is when the top half of each wire is exposed to the moving air stream.

The wing section modeled in this analysis is composed of four main components. The composite skin is a fiberglass/epoxy lay-up with a 60% volume fraction. The core material is Rohacell 31 foam. The SMA wires are Nitinol, and the polymer surrounding the wires is Kapton. The following properties were used in the thermal analysis.

Table 5.2: Wing Section Thermal Properties [28-30]

Material	Thermal Conductivity (W/m-C)	Specific Heat (J/kg-C)	Density (kg/m ³)
Kapton	0.12	1090	1420
Nitinol	8.6	322	6450
Composite	0.543	1000 (estimate)	1600
Rohacell Foam	0.031	1000	32.04

The wing section considered in this analysis is a rectangular cutout, as shown in Figure 5.4. For both configurations, the thickness of the top and bottom composite layers was set at 0.03 inches, or 7.62×10^{-4} meters. The thickness of the core section was 0.25 inches, or 6.35×10^{-3} meters. The spacing of the wires on the surface of the wing was set constant at twice the diameter of the wire.

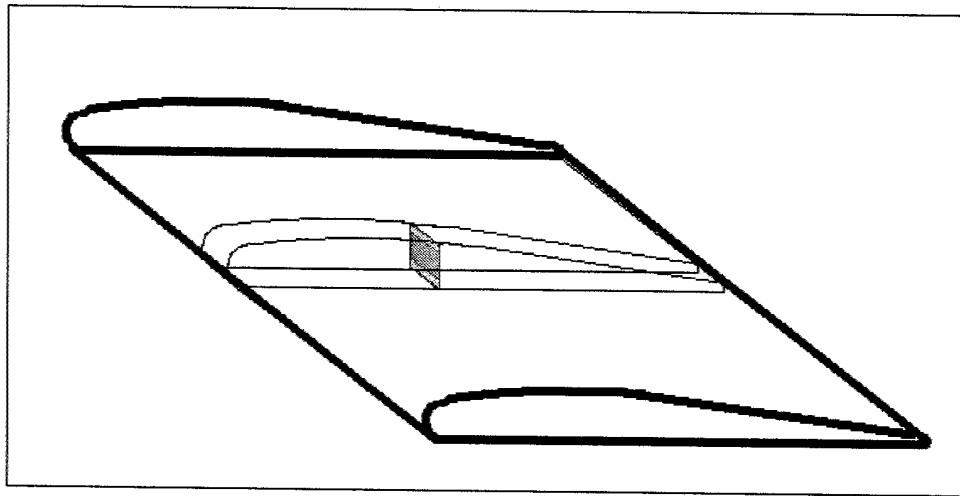


Figure 5.4: Wing Cutout Diagram

For the totally enclosed configuration, the thickness of the polymer on the surface of the wing is twice the wire diameter. The polymer thickness is equal to the wire diameter for the half-enclosed wire configuration. Figure 5.5 shows the typical geometries of the models.

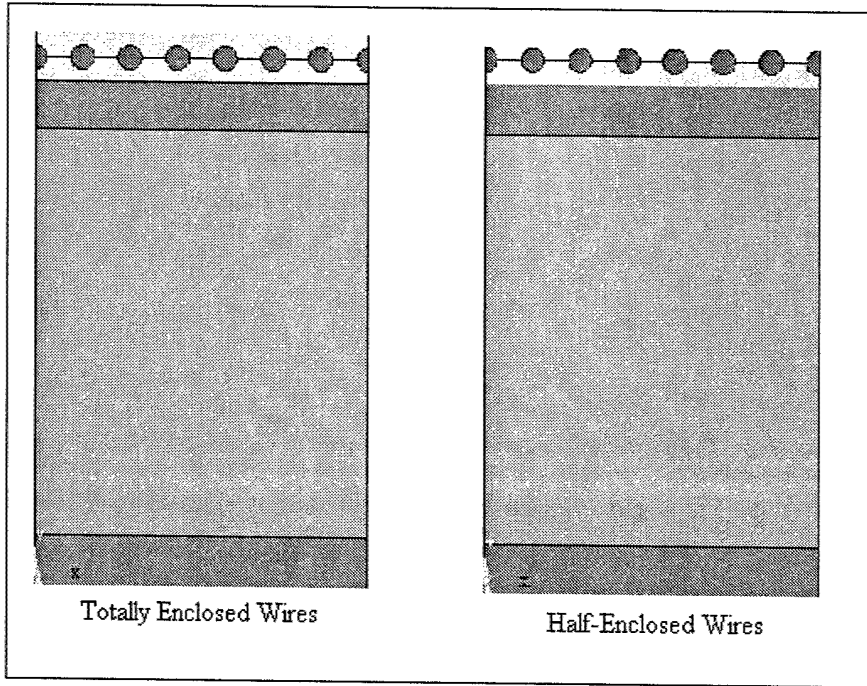


Figure 5.5: Wing Section Model Geometries

For each model, the finite element mesh was generated in a multi-step process. Automatic meshing was used for the circular wire cross-section and the polymer surrounding the wires. Triangular elements were used to mesh the circles. The areas representing the composite layers

and core section were meshed using a simple rectangular mesh pattern. For the entire model, the 4-node PLANE55 element was used as in the single wire model. Figure 5.6 shows a typical meshed model.

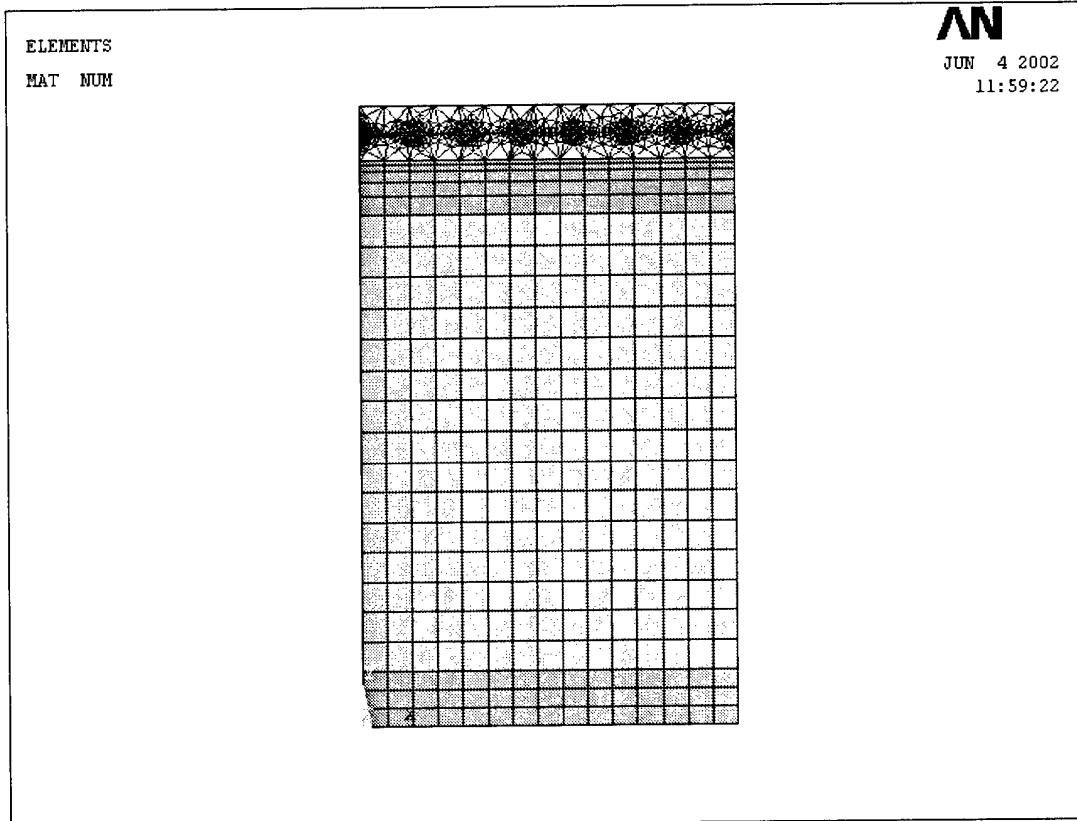


Figure 5.6: Typical Meshed Model

For each wire size and configuration, the response times were recorded, as in the single wire analysis. The following results were obtained.

Configuration 1: Completely Enclosed Wires

As in the single wire analysis, it was expected that there would be a specific diameter wire that minimized the total cycle time for heating and cooling. This trend can be seen in the results, but the minimizing diameter is considerably different from that found for the plain wire with only convective cooling. As shown in Figure 5.7, the amount of time needed to heat the wires decreased as the diameter was increased. This is similar to what occurred for the plain wire. The time needed to cool the wire, however, did not follow the same trend as the plain wires.

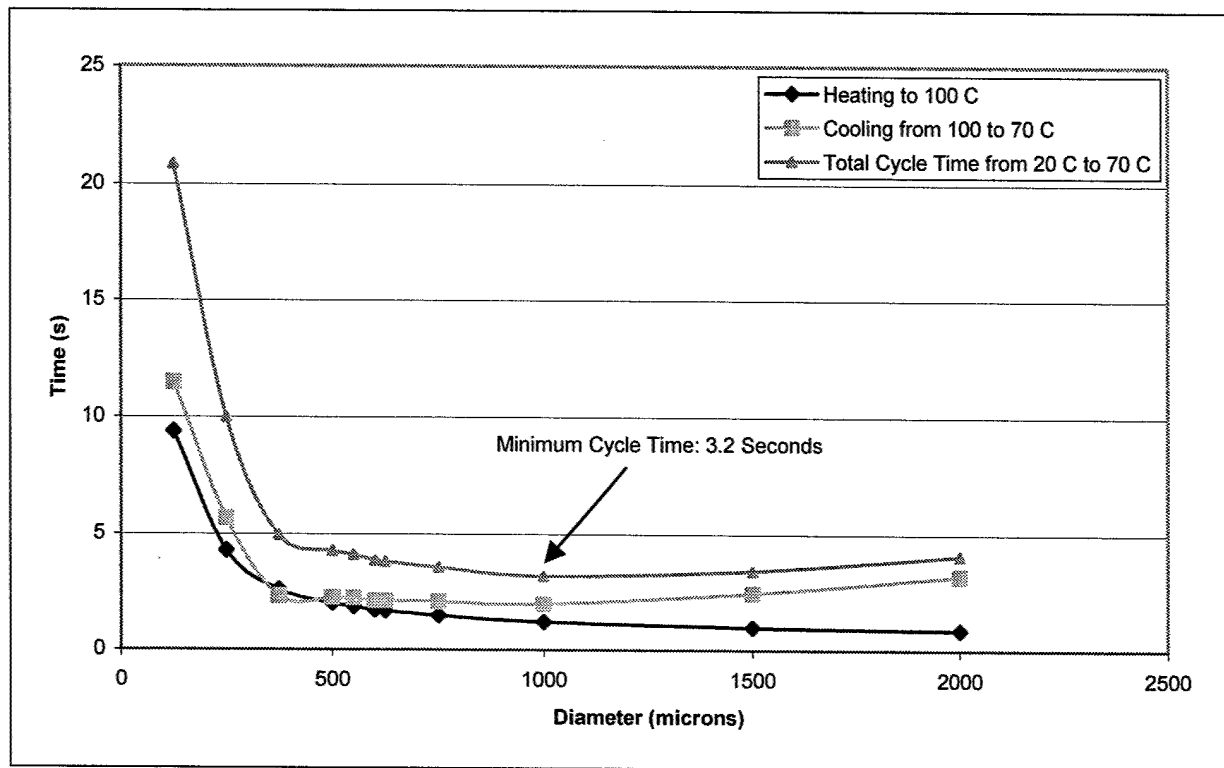


Figure 5.7: Heating and Cooling of Completely Enclosed Wires

Unlike the plain wire, the smallest diameter wires did not produce the lowest cooling times. The minimum amount of time for the wire to cool from 100 to 70 C was found in wires with a 1000-micron diameter.

The reason for this is the presence of the surrounding wing structure and polymer. Since the smaller wires take longer to heat to 100 C, there is more time for heat to flow into the surrounding wing structure and polymer. When the resistive heating is removed and the wires are allowed to cool, more heat must be removed from the surrounding structure before the wires can cool. This results in a longer cooling time for the smaller wires. For wires with a diameter greater than 1000 microns, the difference in heating time is much less pronounced. For this reason, the effect of the surface area to cross-sectional area ratio begins to determine the cooling rate, and increasing diameter wires take longer to cool, as expected.

The result of these trends is that the size of the wire that minimizes the total cycle time increases from under 100-microns in the plain wire case to around 1000 microns for the totally enclosed case. For this configuration, the smallest achievable cycle time is 3.2 seconds.

Configuration 2: Half Enclosed Wires

The removal of the top half of the polymer surrounding the Nitinol wires had a tremendous effect on the cycle time of the wires. In general, the trends for heating and cooling were similar to those found for the first configuration. A notable difference is that the heating time for the half enclosed wires is slightly less than that for the totally enclosed wires. Evidently, the conduction between the wires and the polymer removes heat at a greater rate than the convection used in the model to represent the moving air stream. The time needed to cool the wires is also smaller, which can be explained by the smaller amount of polymer compared to the first configuration. As shown in Figure 5.8, the total result is that for equal size wires, smaller cycle times can be achieved by removing the upper half of the polymer surrounding the wires. In addition, the diameter of the wire that minimizes the cycle time decreases to 550 microns. The minimum cycle time is 2.3 seconds.

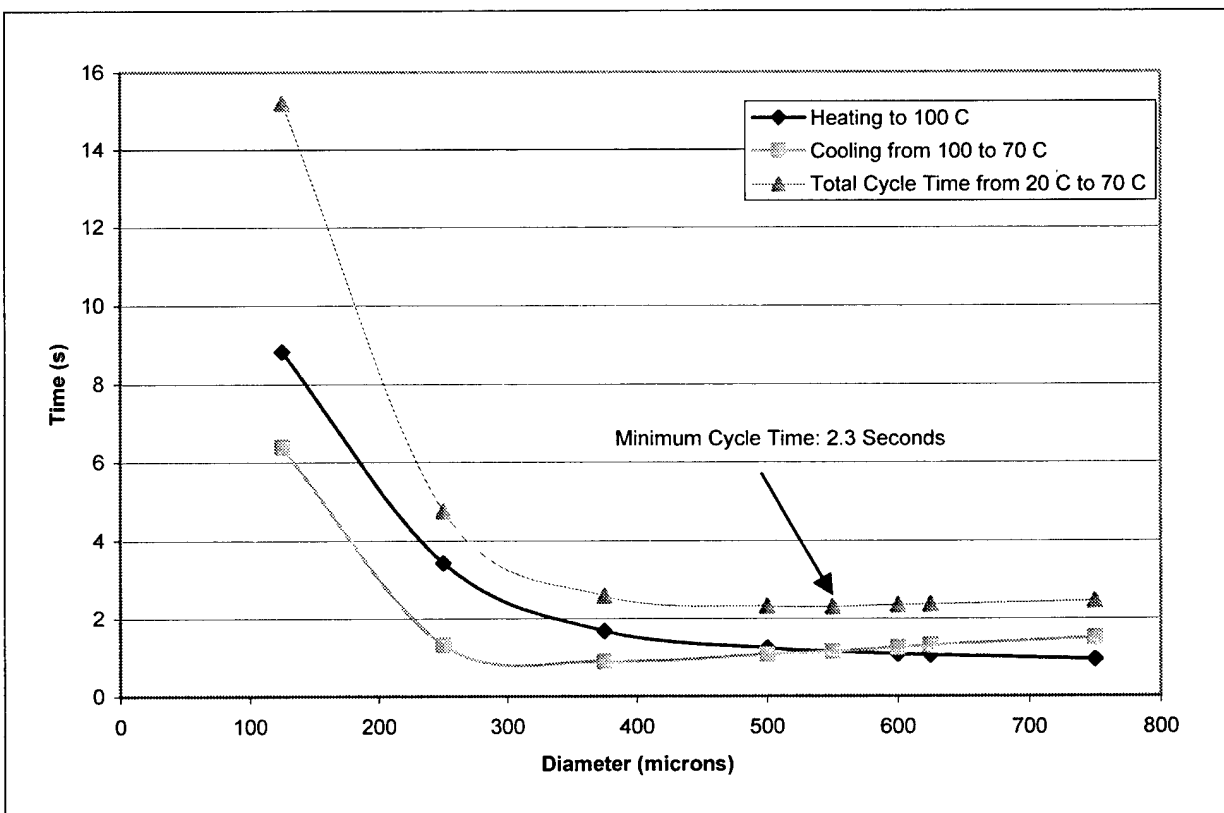


Figure 5.8: Heating and Cooling of Half Enclosed Wires.

5.1.3: Conclusions from Thermal Modeling

After completing the thermal modeling, it was evident that the half covered wires responded faster than those that were fully covered with epoxy. However, for this first order design, it was decided that using a fully covered wire would be much easier in terms of fabrication. The results indicate that the 1000-micron wire produces the fastest combined heating and cooling response when it is totally covered. This response is shown in below.

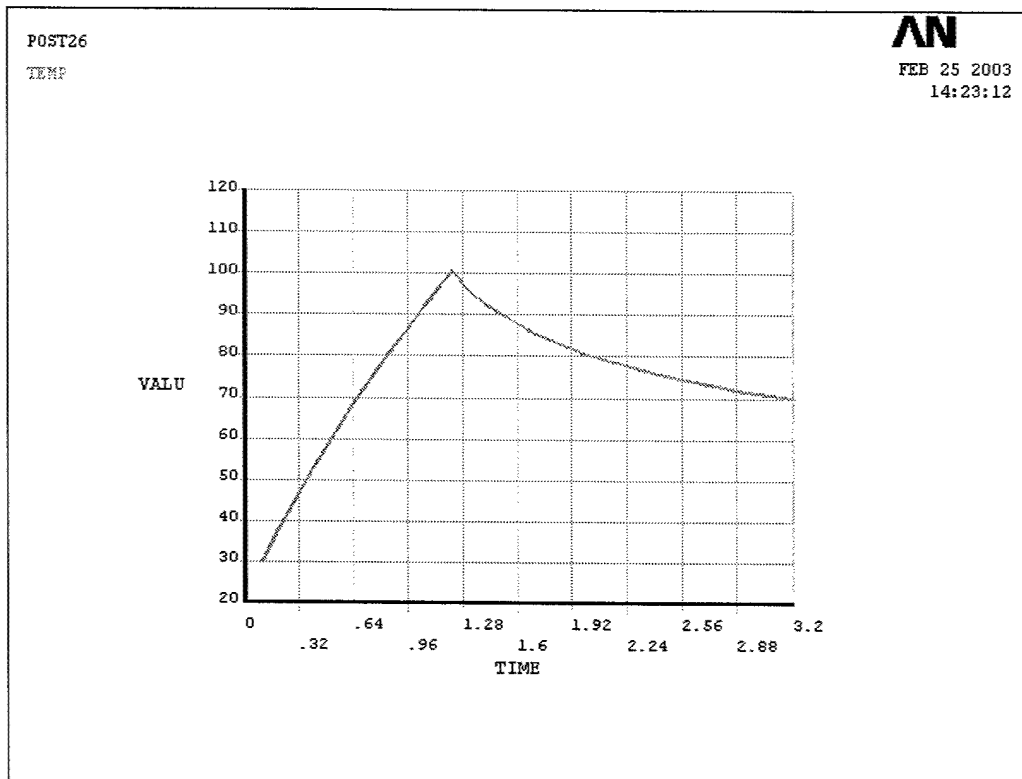


Figure 5.9: Heating and Cooling Response of Covered 1000 Micron Wire (Time in seconds, Temperature in degrees Celsius)

As stated before, this wire has a total cycle time of 3.2 seconds. It takes 1.2 seconds for the wire to heat from 20 degrees Celsius to 100 degrees, and it takes 2 seconds for it to cool from 100 degrees to 70 degrees.

5.2: Structural Modeling

Finite element models were also used to determine the effectiveness of the SMA actuator in twisting the WASP wing.

5.2.1: Initial Wing Twist Models

An important step in advancing from the conceptual design of the SMA actuator was to determine the best location and configuration of the Nitinol wires on the wing. To accomplish this task, a series of simple two-dimensional models were constructed and analyzed. These models were created with the assumption that the bias approach for actuation would be used. The WASP wing was assumed to be a 21 by 2.85 inch rectangle. For each model, a different configuration of Nitinol wire was used, and the wing twist resulting from actuation of the wire was determined from the model solution.

In these models, three material property sets were defined. The core material, which is Rohacell foam, was modeled as an isotropic material.

Table 5.3: Rohacell Foam Properties [30]

Property	Value
Modulus of Elasticity (E, psi)	5000
Poisson's Ratio (v)	.3

The material properties for the remaining materials were taken from data used in previous analyses by Draper Laboratory staff. The fiberglass composite was modeled as a linear orthotropic material, as shown in Table 5.4:

Table 5.4: Fiberglass Properties [31]

Property	Value
E_x (psi)	5.7×10^6
E_y	2.7×10^6
E_z	2.7×10^6
ν_{xy}	0.26
ν_{yz}	0.40
ν_{xz}	0.26
G_{xy} (psi)	4.7×10^5
G_{yz}	4.7×10^5
G_{xz}	4.7×10^5

The Nitinol wire was modeled as if it were contained in a polymer matrix. For this reason, its properties were also defined in terms of a linear orthotropic material.

Table 5.5: Nitinol Properties [31]

Property	Value
E_x (psi)	3.75×10^6
E_y	5×10^5
E_z	5×10^5
ν_{xy}	0.3
ν_{yz}	0.3
ν_{xz}	0.3
G_{xy} (psi)	2×10^5
G_{yz}	2×10^5
G_{xz}	2×10^5

Modeling the wing in two dimensions was made more challenging by the fact that the wing is a multi-layered structure with orthotropic materials in varying orientations. For this reason, it was necessary to use a special type of finite element. The SHELL99 element in ANSYS is known as a Linear Layered Structural Shell. This element has eight nodes, each of which has six degrees of freedom: three translational and three rotational. To define the structure of the model, the SHELL99 element allows each layer to be specified in terms of material, orientation, and thickness. In these models two different element cases were defined. For areas that did not contain Nitinol, each element had 7 layers (1 layer of foam and 6 layers of fiberglass). Areas with Nitinol contained one or two additional layers, depending on the specific configuration. Each of the fiberglass layers was 0.01 inches thick, while the foam core

was 0.25 inches thick. For each configuration, the Nitinol wires were modeled as a constant thickness strip or area, depending on the model. The Nitinol layers were set to be 0.005 inches thick.

In the actual WASP wing, as noted in Chapter Four, the wing has two plies of fiberglass on each side – one plain weave ply and one unidirectional ply. In these models and all subsequent models, however, three plies were used on each side. Because of the difficulty in modeling a woven ply, those layers are modeled using one layer of unidirectional fiberglass in the zero-degree orientation, and one in the 90-degree orientation. This accounts for the six total layers of fiberglass in the SHELL99 elements. This simplification results in a more conservative model, since the weave ply has less stiffness than two plies of unidirectional fibers.

In order to simulate the action of the Nitinol recovering a pre-strain when heated by an electrical current, the models use the concept of an equivalent thermal load. The coefficients of thermal expansion (CTE) for the fiberglass and foam were set to zero. The CTE for the Nitinol was set to be orthotropic, with a value of zero in the minor directions. In the major direction, the Nitinol CTE was set to be -0.04. Thus by applying a one-degree temperature to the model, the Nitinol contracted with a four percent free strain, in accordance with normal thermal strain behavior.

$$\varepsilon_T = \alpha \Delta T \quad (5.4)$$

Once the uniform temperature was applied to the model, the last step was to apply boundary conditions. The edge of the rectangle corresponding to the wing root was fixed to constrain the model.

In total, five cases were analyzed. These are shown in Figure 5.10.

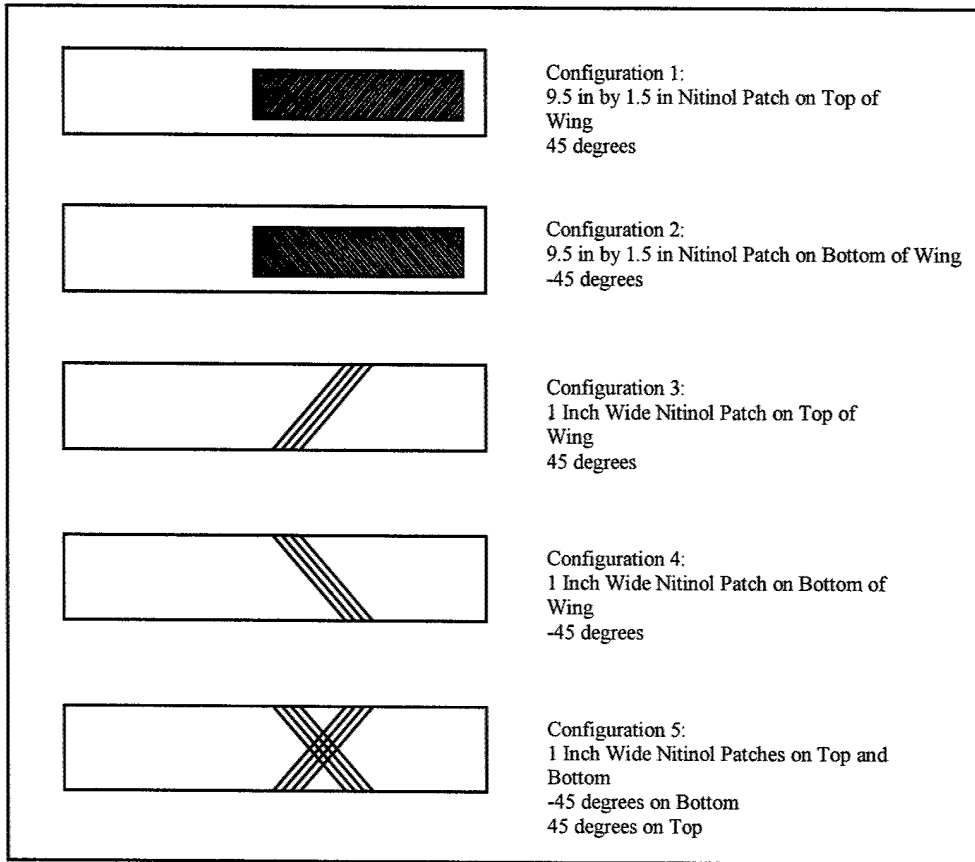


Figure 5.10: Wing Twist Configurations

Each model was run to obtain a solution, and the displacement response of the wing was examined. For each configuration, the amount of rotation at the wing tip was recorded. The amount of wing twist was also compared with the area of Nitinol wire used to determine how efficient the configuration was. Since more Nitinol area means increased wire length, it is best to minimize the Nitinol area to save in both weight and power. The results are shown below.

Table 5.6: Wing Twist Results

Configuration	Nitinol Area (in ²)	Wing Twist (deg)	Twist/Area (deg/in ²)
1	14.25	11.33	0.795
2	14.35	11.17	0.783
3	2.85	2.58	0.973
4	2.85	2.58	0.973
5	5.70	5.25	0.922

The results showed that using a 45-degree strip was the most efficient means to twist the wing, as in configurations 3 and 4. Figures 5.11 and 5.12 show the meshed model and rotation results for configuration 3. The values for the rotation results are in radians.

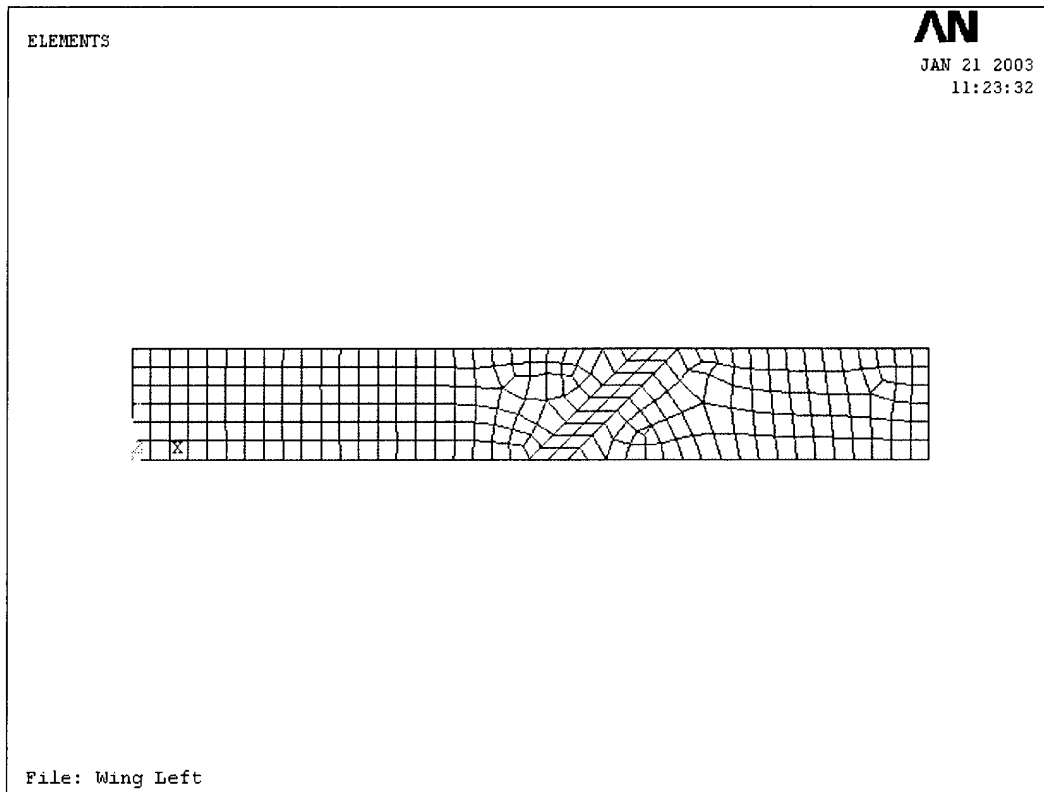


Figure 5.11: Meshed Model of Configuration 3

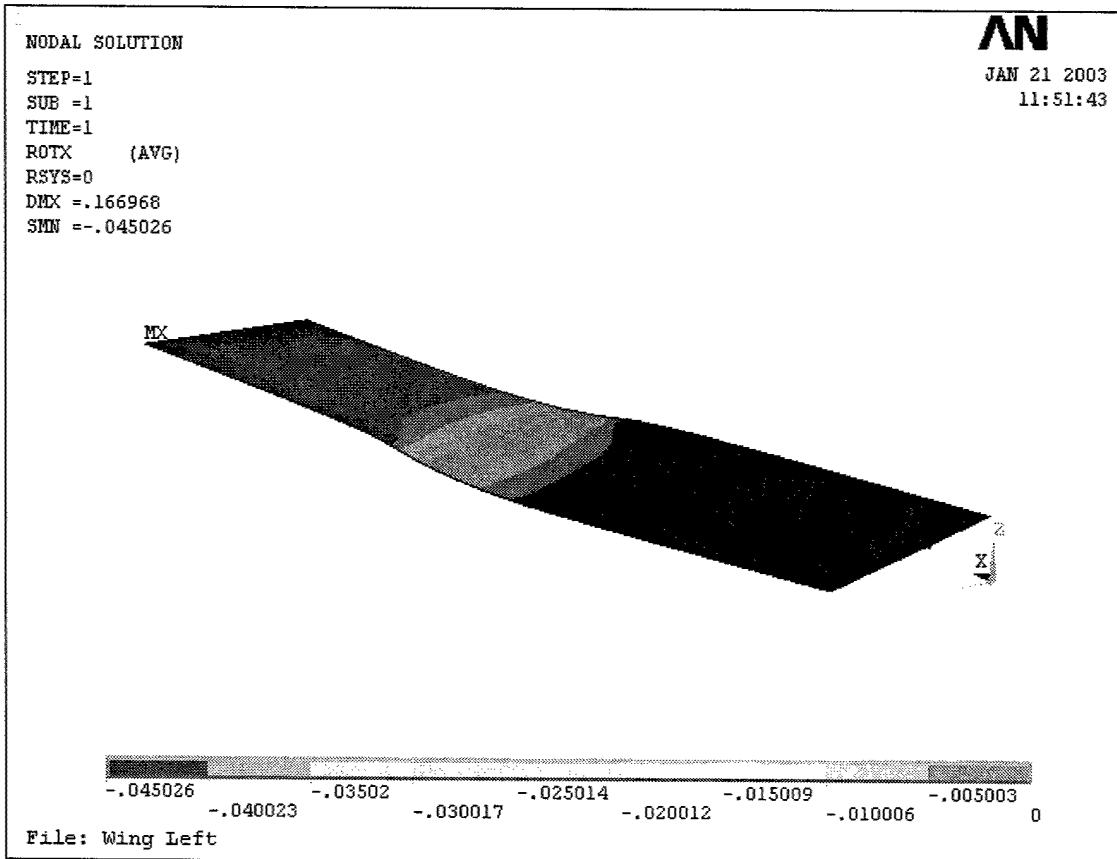


Figure 5.12: Rotation Results for Configuration 3

5.2.2: Bonding Analysis

In the previous analyses, it was assumed that the Nitinol wires were pre-strained by four percent. However, it was noted in Chapter Three that previous work has indicated that sacrificing recoverable strain in the actuator is most likely necessary to preserve a bond between the Nitinol and adhesive. For this reason, a very simple bond analysis was performed using ANSYS. A two dimensional model of a wing with a rectangular profile was constructed, and layers of epoxy and Nitinol were included on top of the upper fiberglass layer. A thermal load was placed on the Nitinol to initiate a thermal strain as in the previous structural models. The leading edge of the wing was constrained, and the following deflection results were produced. The contours show the von Mises stress.

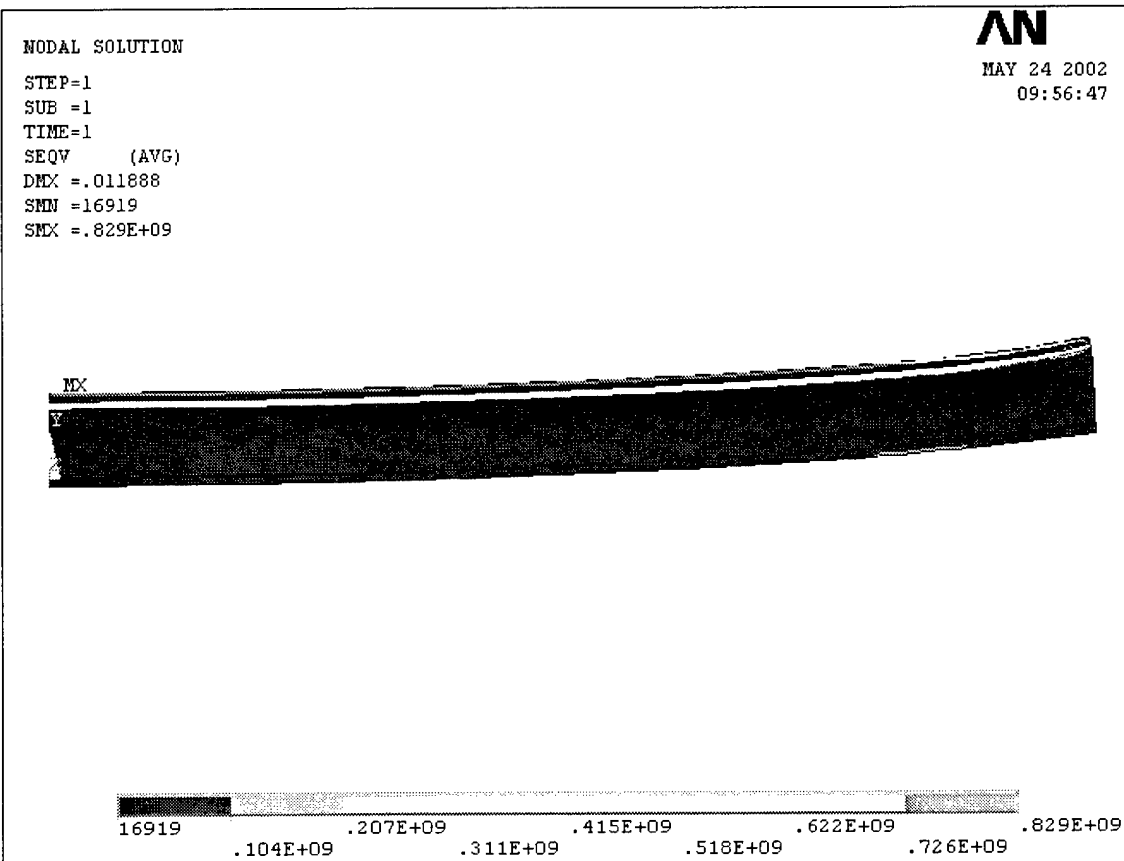


Figure 5.13: Bonding Analysis Stress Results

To determine if the bond would hold, the von Mises stress in the epoxy layer was compared with an approximate tensile strength for high-strength epoxies. The tensile strength was assumed to be 7250 psi or 5×10^7 Pa. Figure 5.14 shows the result for a pre-strain of four percent. The stress near the end of the epoxy layer is greater than the assumed tensile strength, indicating bond failure. To remedy this, lower pre-strain values were used for the Nitinol layer and the analysis was repeated. It was concluded based on these models that a pre-strain of greater than one percent was not feasible if the wires were to remain bonded to the WASP wing.

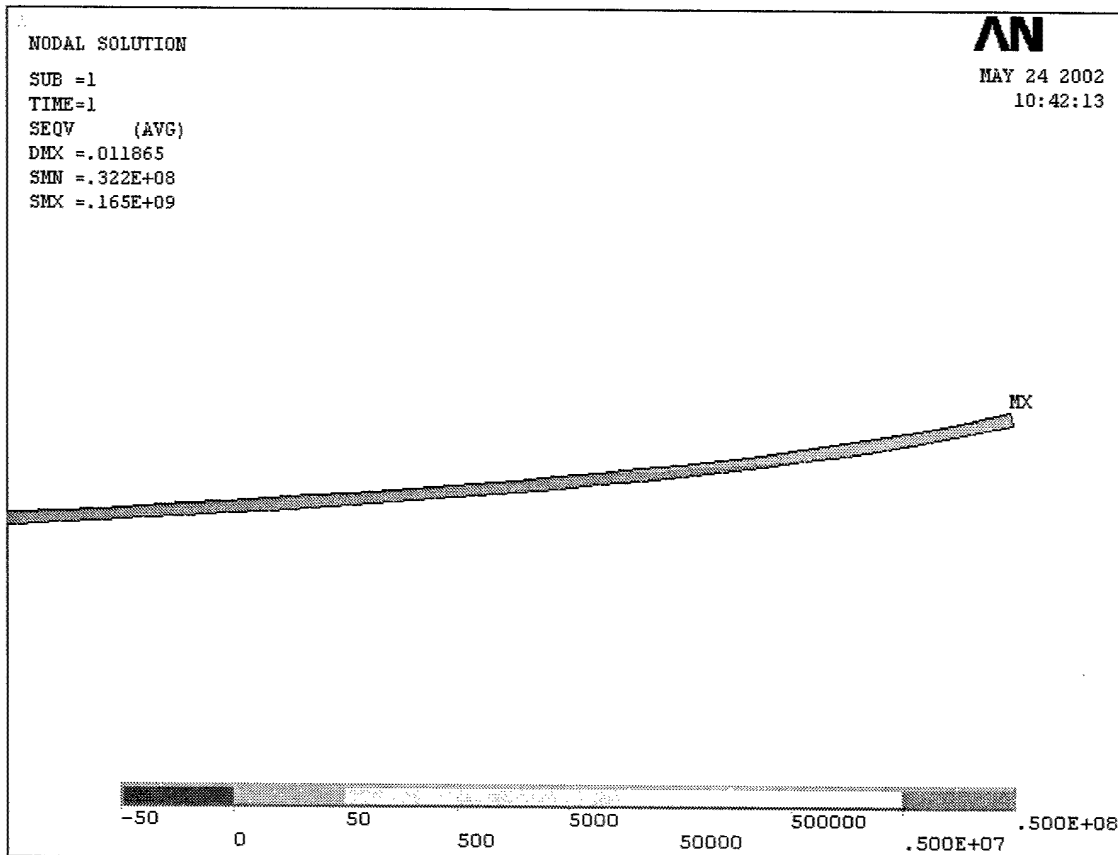


Figure 5.14: Stress in Epoxy Layer

5.2.3: Wing Test Blank Model

After determining the most effective configuration for the Nitinol wire on the surface of the wing and the amount of pre-strain to be used in the wire, the next step was to more accurately determine how much wing twist would result from activation of the wires. The goal of this step was to build a three-dimensional model of the wing in ANSYS that would account for the chosen configuration of Nitinol wires. Attempts were made to capture the exact geometry of the WASP wing, but this model became prohibitively large for repeated analysis. For this reason, it was decided that the best course of action was to construct a finite element model of the three-dimensional test blank that would be used during bench testing.

From the outset, a major simplification was made in the size of the model. Since the WASP wing has a rigid mid-span hinge and the SMA actuator is place on the inboard wing panel, the wing twist on the outboard panel should be constant, and it should equal the twist at

the end of the inboard panel. For this reason, only the inboard panel was modeled in this stage. The inboard panel was constructed in ANSYS as an 11 by 3 inch rectangle with a thickness of .25 inches.

To model the location of the Nitinol wires, a 45 degree section was created in the middle of the wing. Actually modeling the exact geometry of the wires on the surface of the wing resulted in a prohibitively large model, so the wires were modeled as a single layer of Nitinol with its principle axis oriented 45 degrees to the wing. The dimensions and location of this section are shown below.

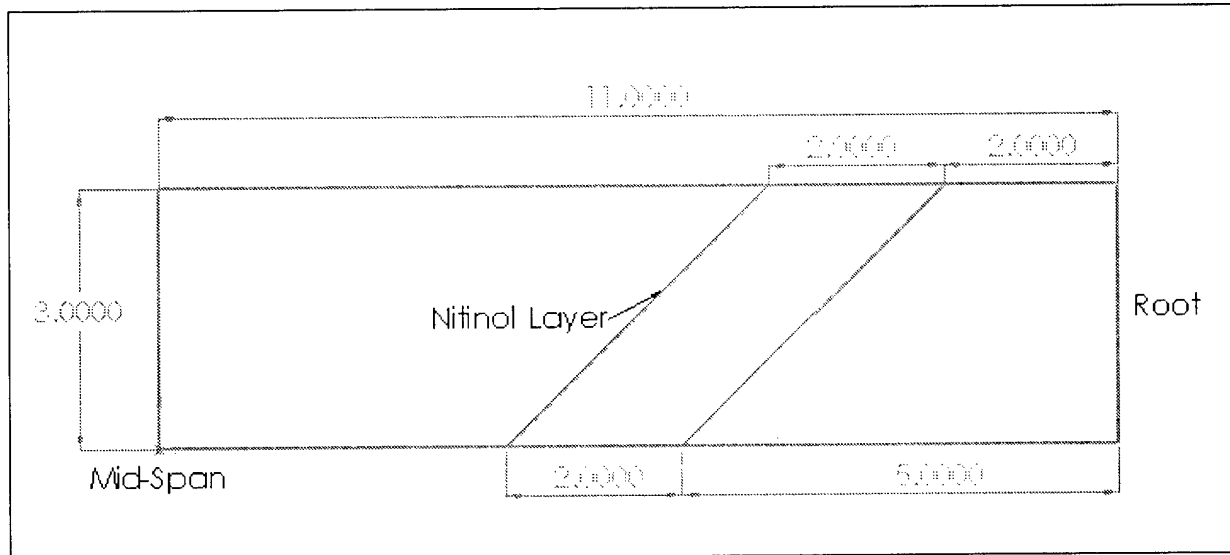


Figure 5.15: Dimensions and Location of Nitinol Section

The materials used for this model were almost identical to those used for the initial wing twist analyses. The properties for the foam and fiberglass remained the same. However, two separate sets of material properties were used to model the Nitinol in the wing, one set for austenite and one for martensite. The properties of martensite are identical to those listed in Table 5.5 with one exception. The modulus of elasticity in the x-direction was corrected to 2.65×10^6 psi to match the value found while running tensile tests on the Nitinol wire used in the experimental stage of this thesis. These tensile tests are described in Chapter Six. The properties for austenite are listed in Table 5.7.

Table 5.7: Nitinol Austenite Properties [31]

Property	Value
E_x (psi)	6×10^6
E_y	5×10^5
E_z	5×10^5
ν_{xy}	0.3
ν_{yz}	0.3
ν_{xz}	0.3
G_{xy} (psi)	2×10^5
G_{yz}	2×10^5
G_{xz}	2×10^5

The modulus of elasticity in the x-direction is much lower than the values indicated in Section 2.5. This disparity will be explained by the results of the tensile testing described in Chapter Six. In addition to these properties, the austenite was set to have a coefficient of thermal expansion of -0.01 in/in. This facilitated the use of the equivalent thermal load to model a one percent pre-strain in the Nitinol wires. A material set for epoxy was also added, since it was assumed that there would be a thin epoxy layer underneath the Nitinol wires. The properties for the epoxy are listed below.

Table 5.8: Epoxy Properties [32]

Property	Value
Modulus of Elasticity (E, psi)	4×10^5
Poisson's Ratio (ν)	.3

To create a finite element mesh for the model, the first step was to mesh the foam core. Since the model was in three dimensions, SOLID95 elements were used in ANSYS to mesh the core. The SOLID95 element contains 20 nodes, and each node has three translational degrees of freedom. Once the core was meshed, the next step was to create a mesh for the outside surfaces of the wing. This was done using SHELL99 elements as before. For areas of the wing where there is no Nitinol, the elements only account for the three fiberglass layers. For areas that are covered by the wires, two layers are added to represent an epoxy layer and the Nitinol layer. As in the previous models, each fiberglass layer was set to be 0.01 inches thick. The epoxy layer was also assumed to be 0.01 inches thick. Each Nitinol layer was 0.008 inches thick. A picture of the meshed model is shown below.

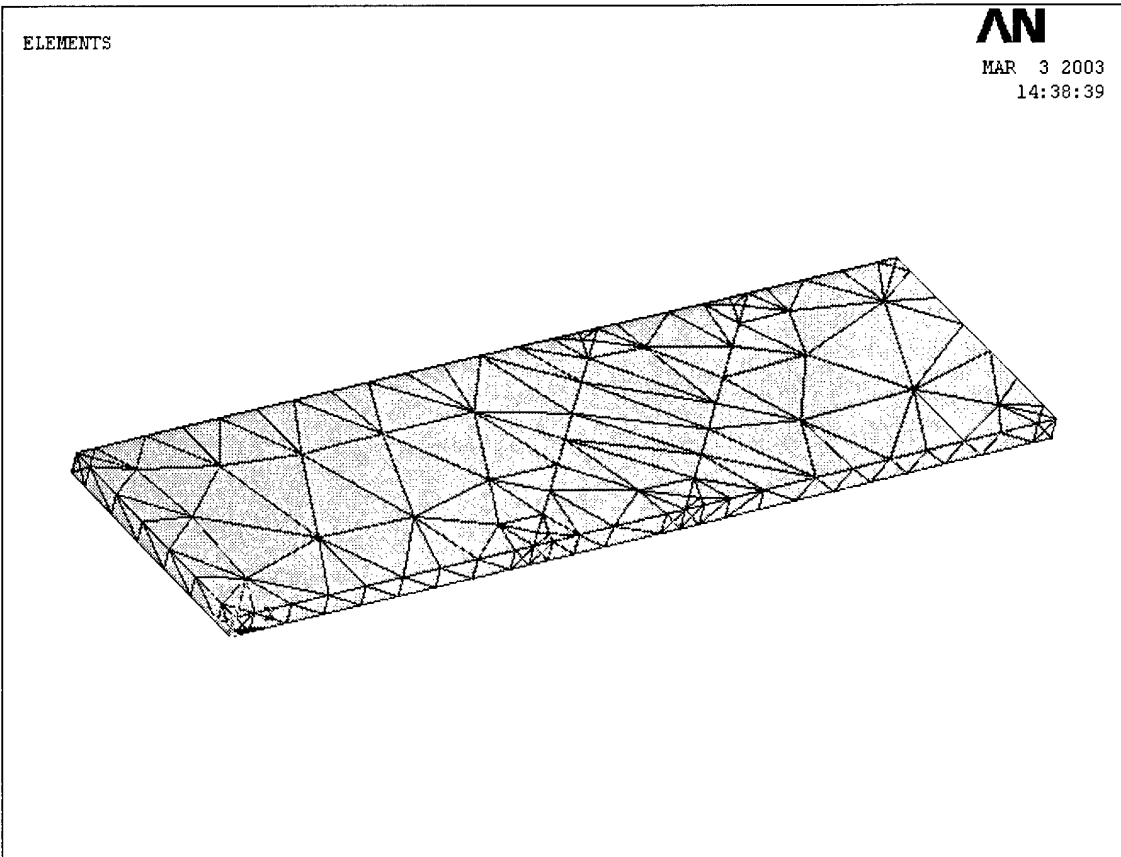


Figure 5.16: Meshed Wing Blank Model

This model was used to analyze both the bias and differential approaches. For the bias approach, the entire bottom surface was meshed with elements containing only the three fiberglass layers. On the top surface, the area containing the Nitinol was meshed with shells containing the fiberglass layers, an epoxy layer, and an austenite layer. For the differential approach, the top surface did not change. On the bottom surface, however, the area containing the Nitinol wires was meshed with shells containing the fiberglass, epoxy, and a martensite layer.

To model the contraction of the top wires due to resistive heating, the equivalent thermal load technique was used again. Since the only material with a non-zero coefficient of thermal expansion was the austenite, adding a uniform temperature of one degree to the model achieved the goal of simulating the resistive heating of the wire. To constrain the model, the right side of the rectangle, corresponding to the wing root end, was fixed in all degrees of freedom.

After running each model, the results for rotation around the span-wise axis of the wing were plotted and the amount of wing twist was analyzed. To determine the exact amount of

wing twist at the mid-span hinge, the vertical deflections of the corner points on that end of the model were used to construct a line. By determining the angle between this line and the horizontal axis, the wing twist was determined.

Figure 5.17 shows the results for the bias approach. The maximum wing twist predicted by the model is 3.29 degrees.

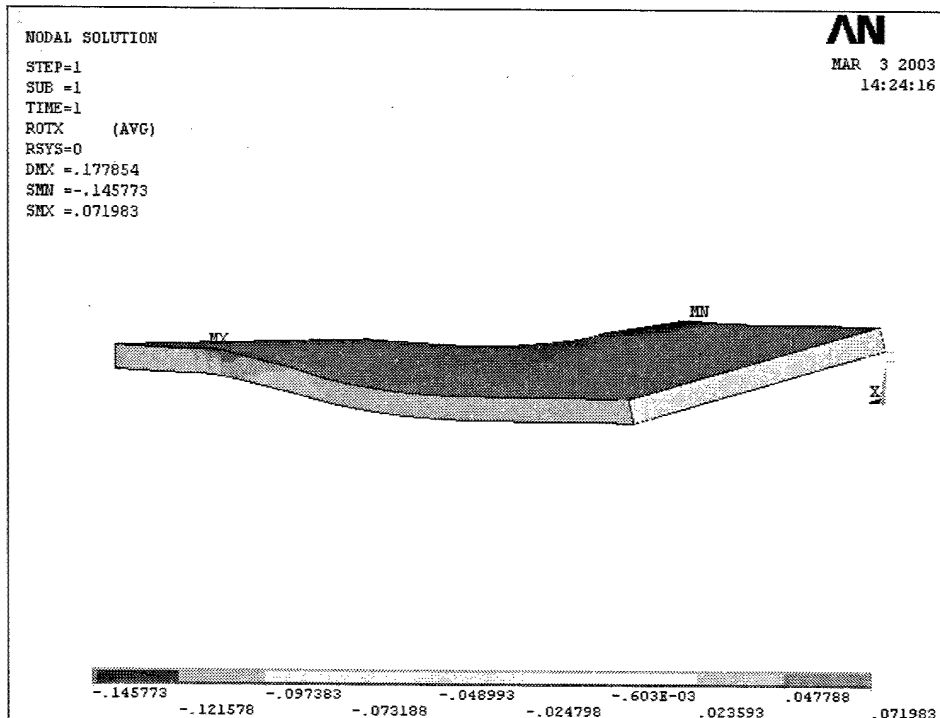


Figure 5.17: Bias Approach Wing Twist Results

Figure 5.18 shows the differential approach structural response. The model predicted 3.18 degrees of wing twist.

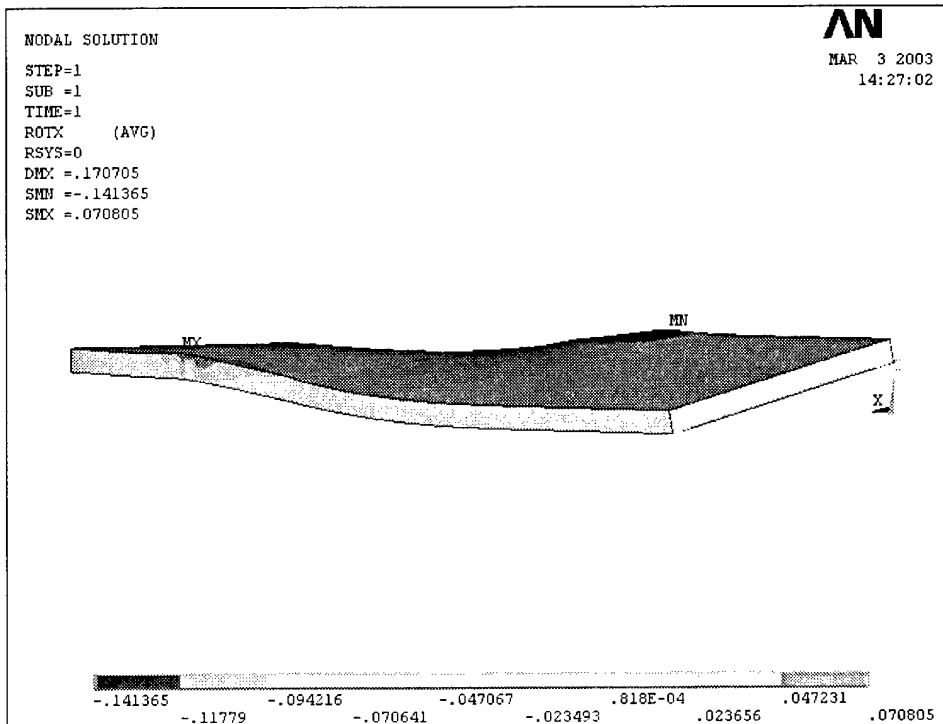


Figure 5.18: Differential Approach Wing Twist Results

The small difference between the two values can be easily explained. Since in the differential approach there are Nitinol wires on the bottom surface of the wing, there is additional stiffness that the top wires must overcome to twist the wing. This is not the case for the bias approach.

5.3: Thermal – Structural Interaction

Up to this point, all the structural analyses have ignored the effects of thermal heating of the wing. However, it is possible that the heating of the fiberglass and foam in the wing could cause deformations that would counteract the motion caused by the Nitinol actuator. To determine if these thermally induced deformations were significant, a finite element analysis was performed in ANSYS.

The first step was to characterize the heat transfer between the Nitinol and the rest of the wing. By performing a simple transient thermal analysis, it was shown that as the Nitinol is

heated, there is almost no span-wise heat transfer. Heat does flow down into the fiberglass and the core, but only in the area directly below the Nitinol. This result is shown in the temperature profile below, with units of degrees Celsius.

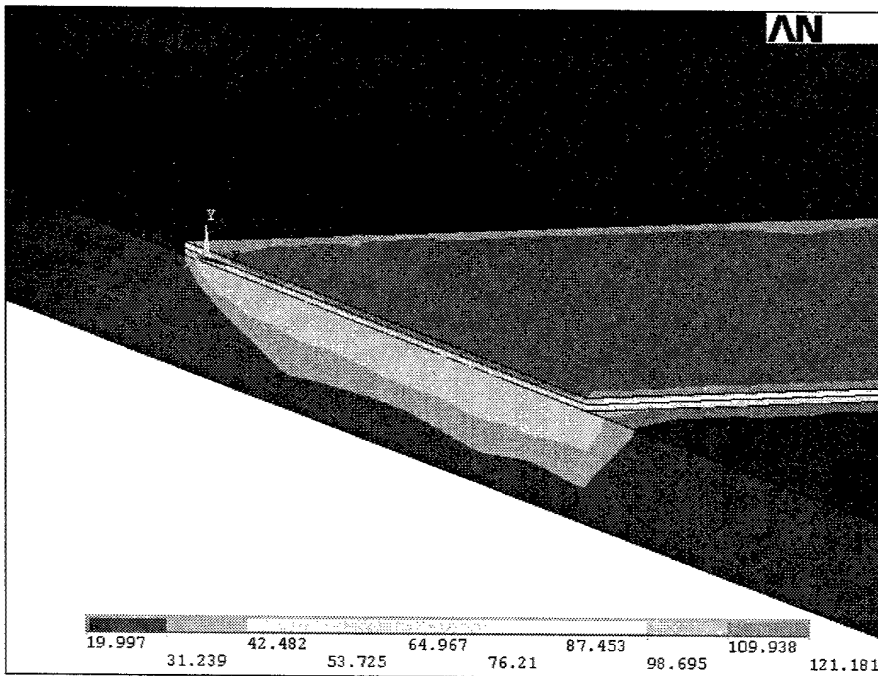


Figure 5.19: Heat Distribution in Wing

The heating of the wing in the area below the Nitinol wires can have two main effects. If only one of the composite panels is heated, there will be a non-uniform expansion which will move the wing tip up or down, depending on which side the wires are located. If both panels are heated uniformly, this effect is negated. The second effect is the bulk expansion of the foam core. To determine if these effects could be ignored, it was necessary to determine the numerical values for the deformation values in these two scenarios. Using a structural model similar to that used to determine the wing twist for the bias and differential approaches, the true values for each material's coefficient of thermal expansion were input, and temperatures were added to the model. The values used for the coefficients of thermal expansion are listed below.

Table 5.9: Coefficients of Thermal Expansion [30,31]

Material (direction)	Value
Rohacell Foam (isotropic)	$2.1 \times 10^{-5}/^{\circ}\text{F}$, $3.7 \times 10^{-5}/^{\circ}\text{C}$
Fiberglass (x)	$4 \times 10^{-6}/^{\circ}\text{F}$, $7.2 \times 10^{-6}/^{\circ}\text{C}$
Fiberglass (y)	$1.6 \times 10^{-5}/^{\circ}\text{F}$, $2.9 \times 10^{-5}/^{\circ}\text{C}$
Fiberglass (z)	$1.6 \times 10^{-5}/^{\circ}\text{F}$, $2.9 \times 10^{-5}/^{\circ}\text{C}$

For the first case, the top layer of fiberglass in the Nitinol covered area was set to be 100 Celsius, which is an increase of 80 degrees from the assumed ambient air temperature of 20 Celsius. This produced a rotation of the wingtip downward, as shown in Figure 5.20. The maximum amount of translation downward was 0.050479 inches, which is almost 1.3 mm. There was also a net clockwise rotation around the span-wise axis of 0.116 degrees, which is in the direction opposite the twist imparted by the Nitinol actuator.

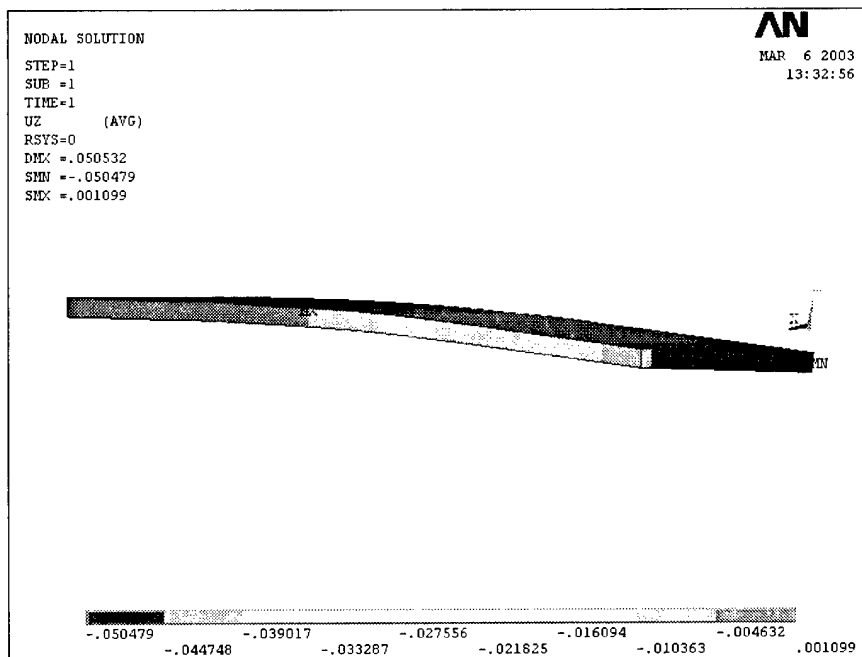


Figure 5.20: Deflection Due to Expansion of Top Fiberglass Layer

In the case of bulk expansion, the entire area under the Nitinol wires was set to 100 Celsius. The results for each direction of deflection are shown below.

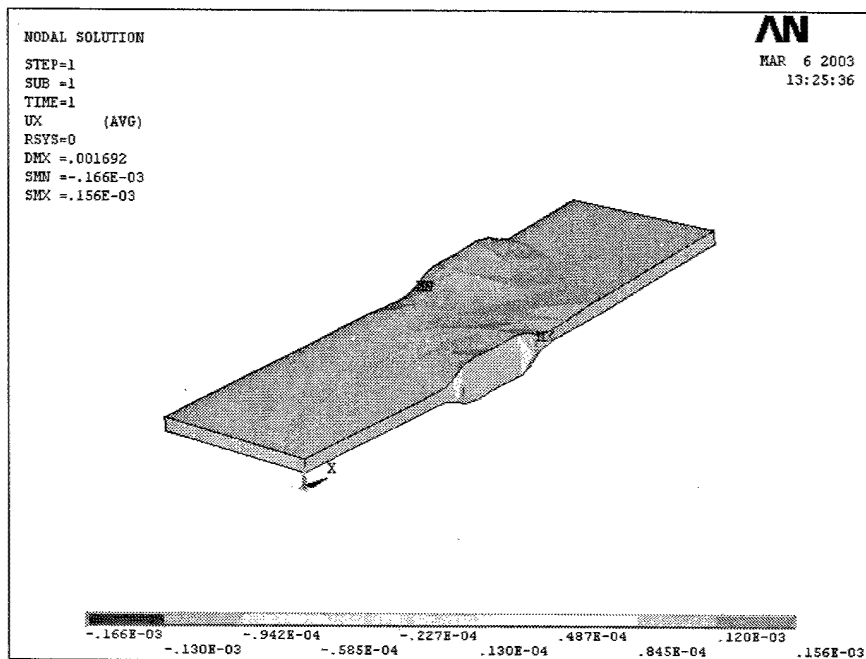


Figure 5.21: Deflection from Foam Expansion in X-Direction

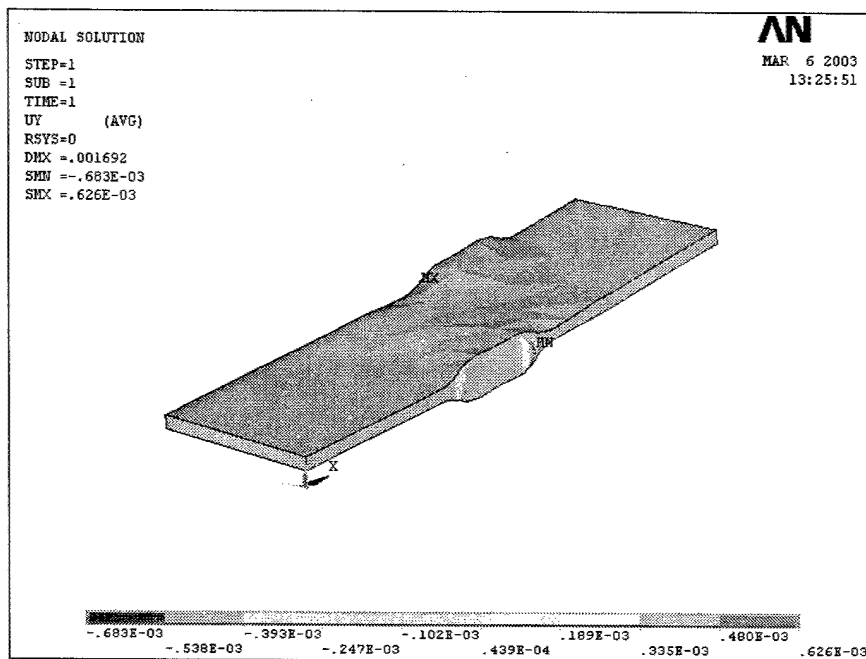


Figure 5.22: Deflection from Foam Expansion in Y-Direction

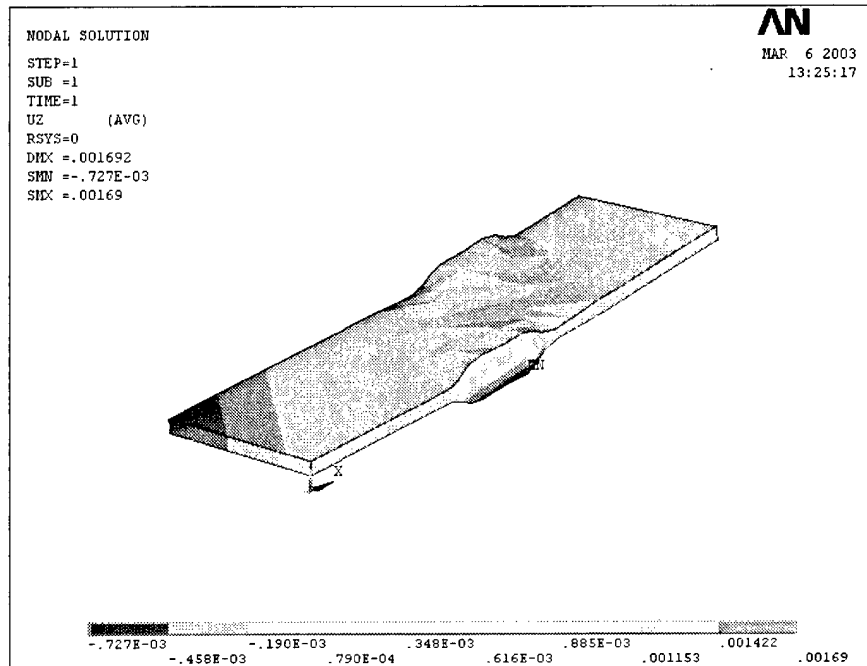


Figure 5.23: Deflection from Foam Expansion in Z-Direction

As shown, the deflections due to thermal expansion of the foam are extremely small, and can most likely be ignored. The maximum deflections in each direction are listed below.

Table 5.10: Maximum Deflections from Foam Expansion

Direction	Deflection (in)
X	0.166×10^{-3}
Y	0.683×10^{-3}
Z	0.00169

It should be noted, however, that the expansion of the top fiberglass layer produces a deflection of the wing tip downward. Also, the rotation about the span-wise axis works against the Nitinol actuator. Since the amount of thermally induced rotation is small compared to the expected rotation produced by the actuator, this is not a huge concern. Overall, the effects of the wing materials' coefficients of thermal expansion should not hamper the performance of the actuator.

5.4: Performance Analysis

For simplicity, all performance analysis is done using the assumption that the longitudinal axis of the WASP is fixed. With this axis fixed, only roll motion is permitted. By using this assumption, the six small-perturbation equations of motion for the airplane can be reduced to one equation [33].

$$I_{xx}\dot{p} = qSb\left(C_{l\rho}\frac{pb}{2v} + C_{l\theta}\right) \quad (5.5)$$

In this equation, I_{xx} is the moment of inertia about the longitudinal axis of the aircraft. The roll rate is represented by p , q is the dynamic pressure, S is the plan form area of the two wings, b is the overall wingspan, and v is the velocity of the aircraft. The remaining variables are $C_{l\rho}$, the roll damping coefficient, and $C_{l\theta}$, the roll moment coefficient caused by the twisting of the wing.

These are non-dimensional coefficients. Most of these variables are defined by the shape, size, and specified performance window of the WASP. These are shown below.

Table 5.11: Roll Equation Constants

Variable	Value
I_{xx}	0.055 slug-ft ²
q	9.204 lb/ft ²
S	0.962 ft ²
b	4.05 ft
v	88 ft/s

It should be noted that the value for the dynamic pressure is calculated using the sea level value for the density of air, 0.002377 slugs/ft³.

In order to determine the roll rate caused by the wing twist, the values for the roll damping coefficient and roll moment coefficient must also be known. In order to determine these values, it was necessary to utilize an Athena Vortex Lattice (AVL) model of the WASP that was designed by Sean George, a Draper Laboratory engineer. The first input needed to make the model produce the desired results was the profile of the expected wing twist along the span of the wing. In general terms, this profile is shown below.

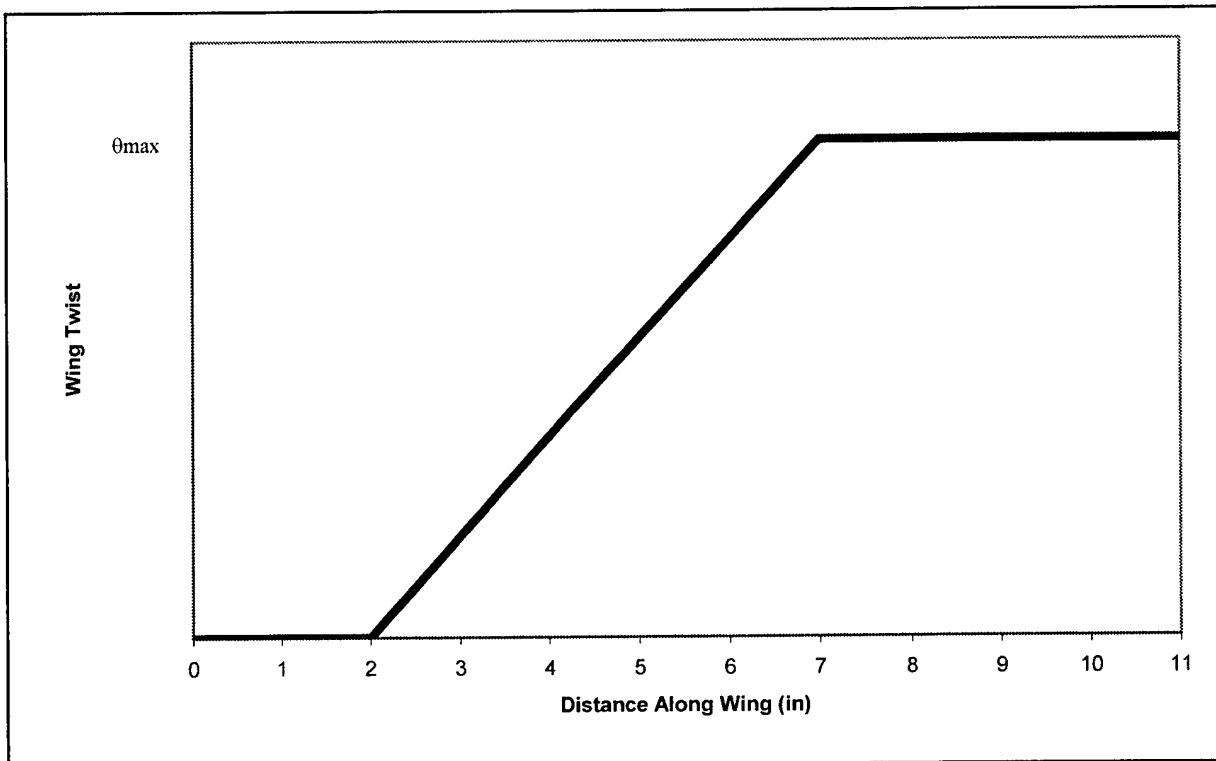


Figure 5.24: Wing Twist Profile for Inner Wing Panel

This profile is based on the assumption that the wing twist will increase linearly along the span of the wing in the area covered by the SMA actuator. The inner panel will be twisted to a maximum value θ_{\max} . As stated before, it is assumed that the wing twist will be constant at a value of θ_{\max} on the outer panel.

With the wing twist profile known, it was possible to input the cruise velocity and obtain the needed values. The program produced a roll damping coefficient for the WASP of -0.721 . For the roll moment coefficient, the value produced by AVL was $0.465/\text{radian}$. To find the exact roll moment coefficient, this value must be multiplied by the maximum twist angle, θ_{\max} . This roll moment coefficient is obtained by assuming that only one wing twists to initiate the roll.

Having determined numerical values for the variables in Equation 5.5, the next task was to solve it to determine the roll performance of the aircraft. As an initial step, solving the equation by hand and letting the time approach infinity produced the steady state solution to the equation. Using this process, the steady state roll rate was found to be:

$$p_{ss} = -\frac{C_{l_0} * 2 * v}{C_{l_p} * b} \quad (5.6)$$

If the steady state roll rate is calculated for successively larger angles of twist, the following relationship results. Not surprisingly, larger twist angles produce larger roll rates.

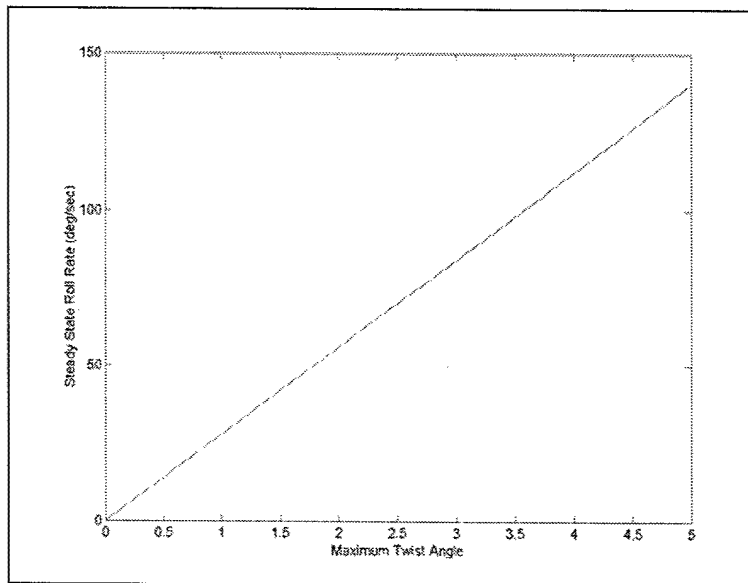


Figure 5.25: Steady State Roll Rate for Various Maximum Twist Angles

Using MATLAB, it is simple to solve Equation 5.5 to determine the overall time response given a specific maximum angle of twist. For example, if a maximum twist angle of one degree is assumed, it takes approximately 0.4 seconds for the roll rate to reach the steady state value, as shown below.

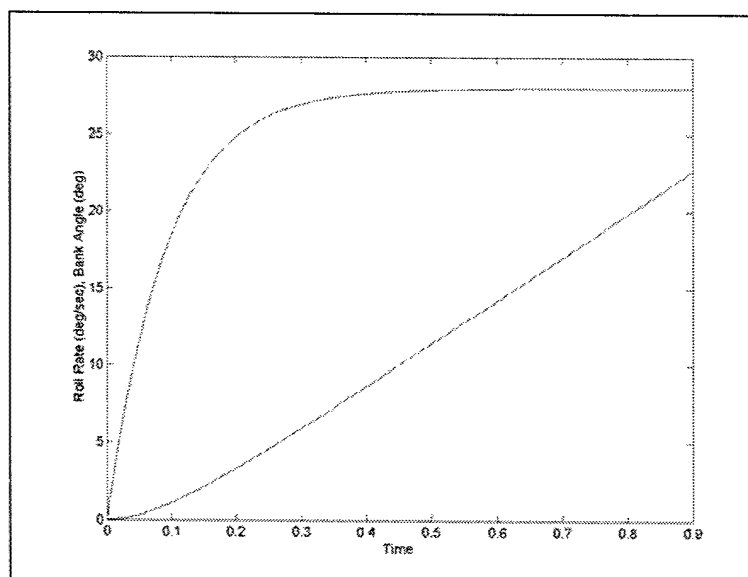


Figure 5.26: Roll Rate and Bank Angle Response for One Degree Wing Twist

These results are only moderately useful, however. This method of solving Equation 5.5 assumes that the wing twists instantaneously and that the roll moment coefficient instantly changes from zero to its maximum value. In reality, this is not so. The roll moment coefficient actually ramps up to its maximum value as wing twist gradually increases. To improve this model, the time elapsed while the wing twists must be considered.

The reason why the wing will not twist instantaneously is related to the transition temperatures described in Chapter Two. If Nitinol wire is heated, the phase change in the wire begins when the temperature reaches the austenite start temperature. At this point the wire will begin to deform and recover the pre-strain, as martensite begins to change to austenite. This will continue until the temperature reaches the austenite finish temperature, at which time all the Nitinol will be austenite and the wing will be completely twisted. In the bias approach, this phenomenon also is seen when the wing untwists. This time, the wing begins to recover the twist when the wires cool to the martensite start temperature, and the twist is completely eliminated when the wires have cooled to the martensite finish temperature.

The time needed for the wing to twist is therefore based on the time it takes for the Nitinol wire to heat and cool. Figure 5.9 showed the time response of the chosen Nitinol wires. A summary of these times is shown below. These times are based on the assumption that the ambient air temperature is 20 degrees Celsius and the M_f , M_s , A_s , and A_f temperatures are 70, 85, 85, and 100 degrees respectively.

Table 5.12: Heating and Cooling Times for Nitinol Wire

Action	Time
Heat from 20 C to 85 C	0.9 s
Heat from 85 C to 100 C	0.3 s
Cool from 100 C to 85 C	0.5 s
Cool from 85 C to 70 C	1.5 s

For the bias approach, these times indicate that if a wing starts an ambient air temperature of 20 C, it will take 3.2 seconds for the wing to twist and untwist. For the differential approach, these times mean that once heating of the top wires begins, they will not cool back to the M_f temperature for 3.2 seconds, meaning that the bottom wires cannot begin to deform for 3.2 seconds. Assuming that the bottom wires are heated to A_s at the same time the top wires reach M_f , it will take the wing 3.5 seconds to twist and untwist using the differential approach.

Since the roll moment coefficient varies with time, finding the solution to Equation 5.5 becomes more complicated. However, if the equation is rewritten, it can be seen that the roll moment coefficient acts as a forcing function.

$$I_{xx}\dot{p} - qSbC_{l_p} \frac{pb}{2v} = qSbC_{l_0} \quad (5.7)$$

If it is assumed that the wing twists linearly with time as the temperature in the wire increases from A_s to A_f (as in both approaches) and that the wing untwists linearly with time as the temperature decreases from M_s to M_f (as in the bias approach), this forcing function can be written as a piecewise linear function in time. Furthermore, Equation 5.7 can be easily discretized using a finite difference approximation with time.

$$I_{xx} \frac{p_{i+1} - p_{i-1}}{2\Delta t} - qSbC_{l_p} \frac{b}{2v} p_i = qSbC_{l_0} \quad (5.8)$$

A MATLAB program was used to transform this equation into a matrix equation, and this equation was solved to find the roll rate and bank angle values at each time step.

5.4.1: Bias Approach Performance

For the bias approach, the first analysis performed was a simulation of a single actuation cycle for one wing assuming the 3.2 second actuation cycle. Assuming a maximum wing twist of one degree, the roll rate reaches a maximum value of nearly the steady state value. As seen below, the roll rate slope gradually increases after the wing twist begins to increase at 0.9 seconds.

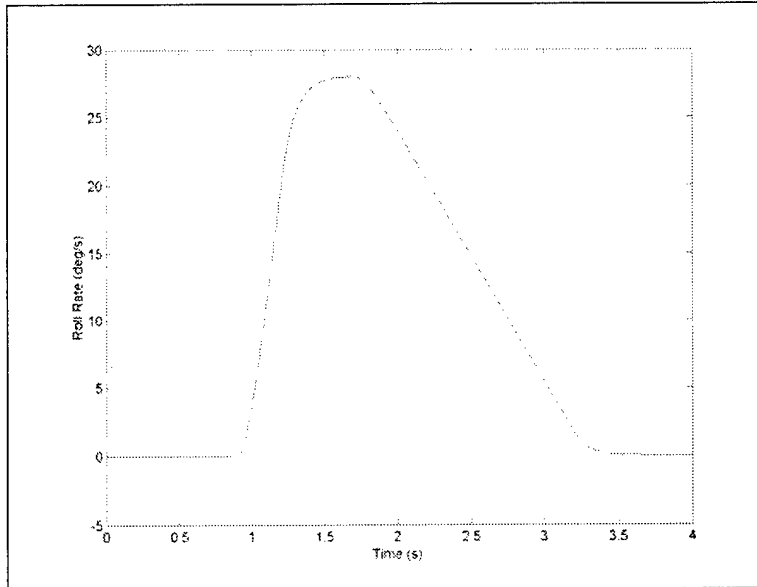


Figure 5.27: Roll Rate Response for Bias Actuation of One Wing (One Degree Wing Twist)

The bank angle produced by the actuation of one wing reaches a maximum value of almost 40 degrees.

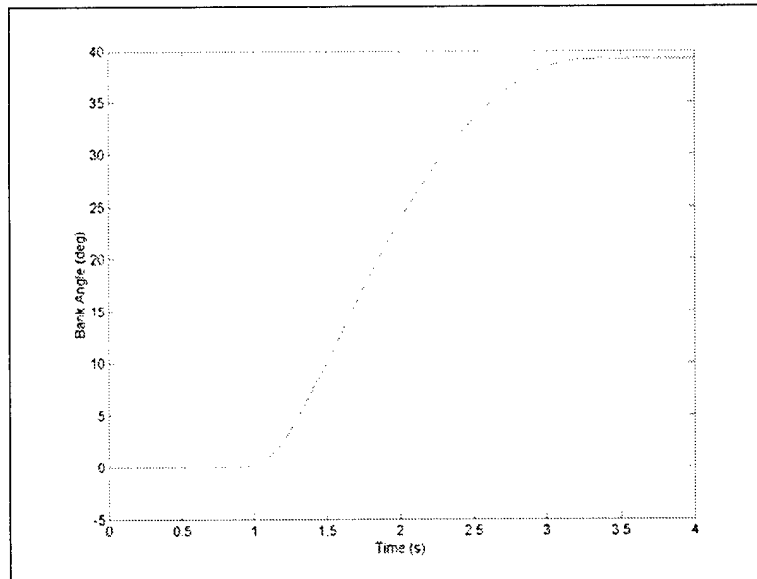


Figure 5.28: Bank Angle Response for Bias Actuation of One Wing (One Degree Wing Twist)

If the wing twist value is allowed to vary, the value of the steady state bank angle reached by actuating and relaxing one wing follows a linear relationship with the maximum wing twist value, as illustrated in Figure 4.7.

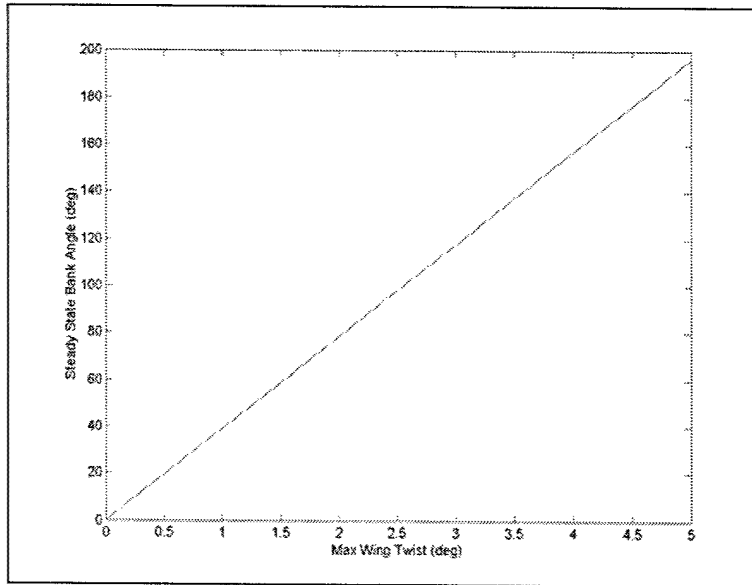


Figure 5.29: Bank Angles From Bias Actuation of One Wing

In order for the aircraft to recover from the roll and return to level flight, the opposite wing must be actuated. In the MATLAB program, this was modeled by summing the effects of the roll moment coefficients produced by each wing to determine an overall roll moment coefficient function. The roll rate and bank angle responses were examined for different delays between the actuation of the first wing and actuation of the second. Figures 5.30 and 5.31 show the responses for a delay of 0.1 seconds.

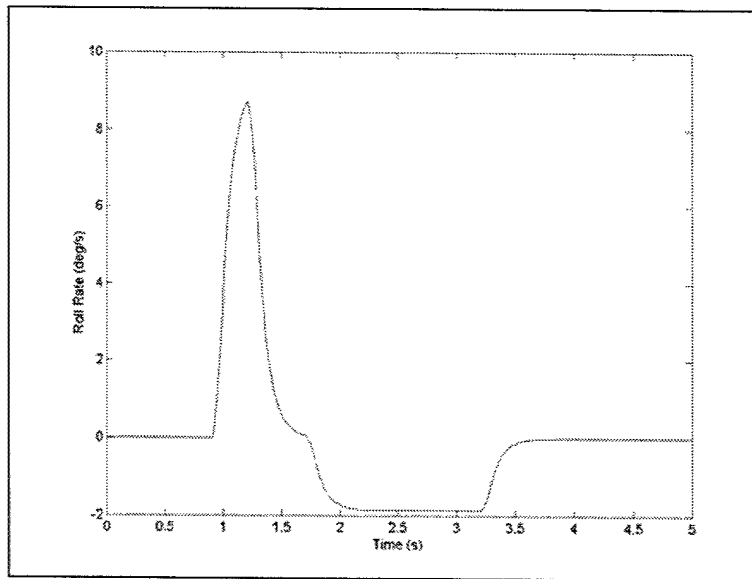


Figure 5.30: Roll Rate Response for Bias Actuation with 0.1 Second Delay

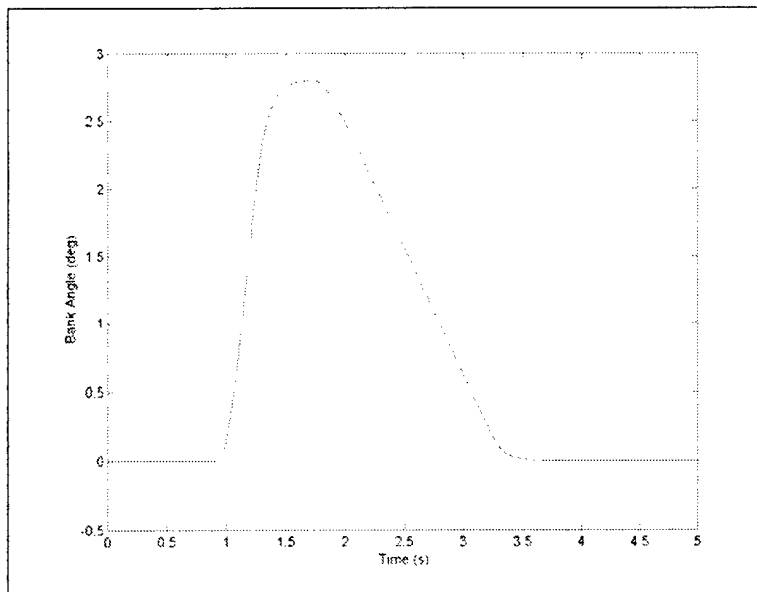


Figure 5.31: Bank Angle Response for Bias Actuation with 0.1 Second Delay

If the delay is increased to 0.5 seconds, the following results are produced:

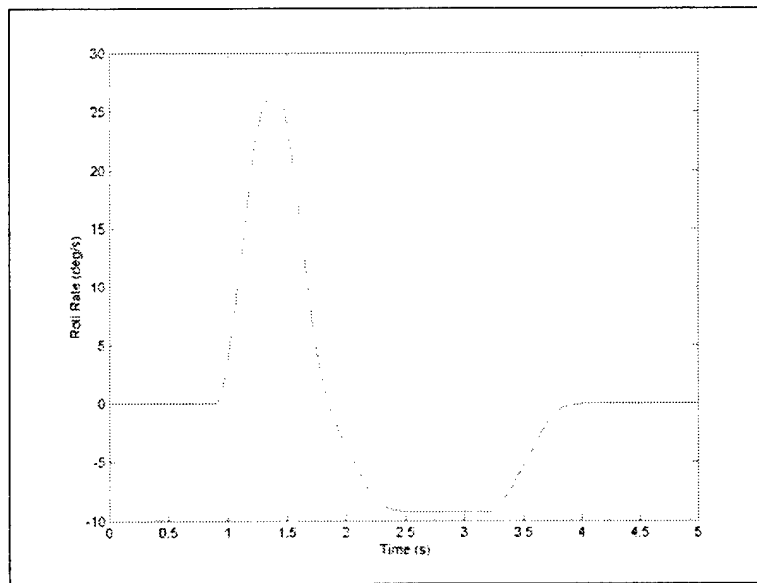


Figure 5.32: Roll Rate Response for Bias Actuation with 0.5 Second Delay

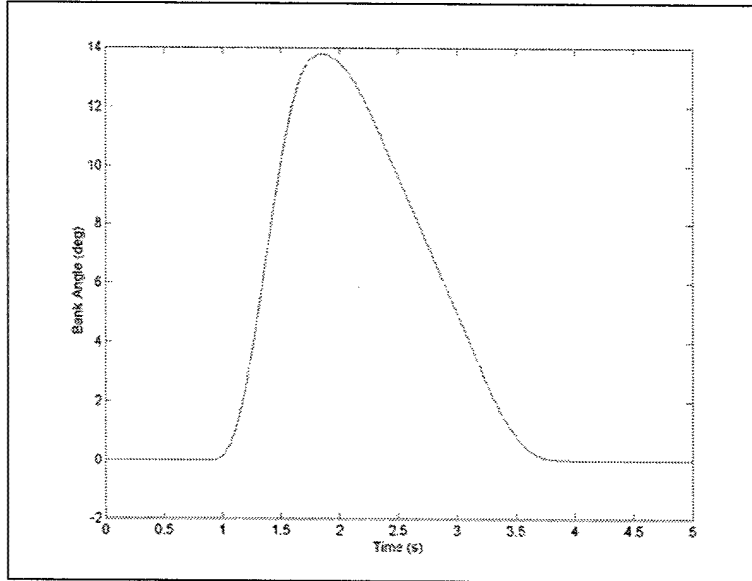


Figure 5.33: Bank Angle Response for Bias Actuation with 0.5 Second Delay

So far it has been assumed that the wing would be actuated and allowed to cool in the fastest time possible. As soon as the A_f temperature is reached in the wire, the power would be cut off and cooling would begin. It is possible, however, to extend the time the wing is actuated by pulsing the current, which would be intended to keep the temperature just above M_s , since that is the temperature where the wing would begin to untwist. If it is assumed that the wing twists to one degree and that there is a 0.5 second delay between the actuation of the first and second wings, then powering the actuator on each wing for an additional 0.5 seconds produces the following results.

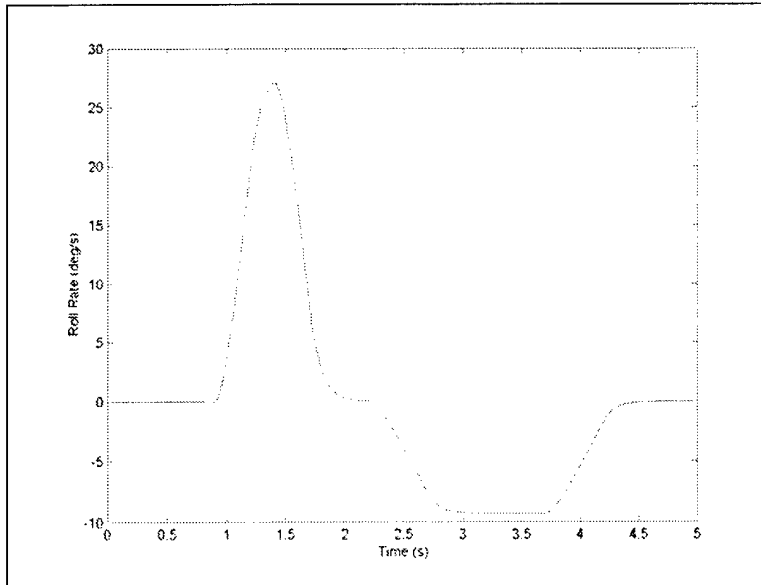


Figure 5.34: Roll Rate Response for Bias Actuation with 0.5 Seconds Additional Power

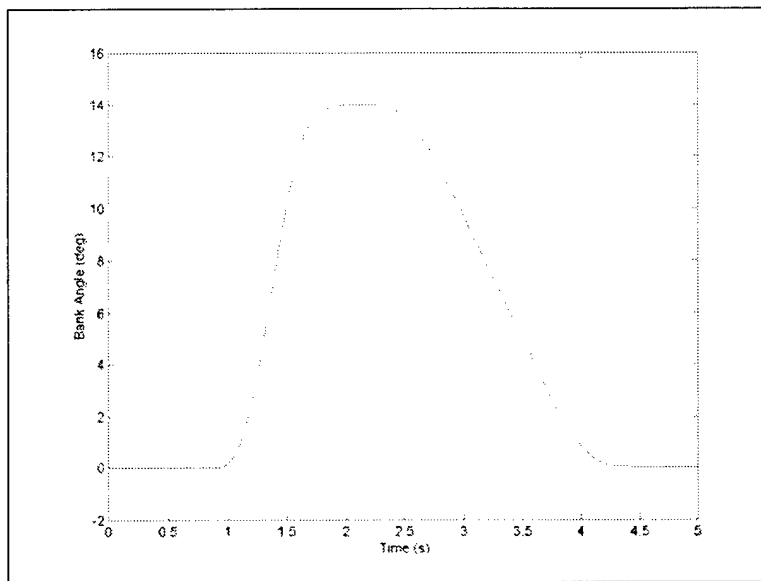


Figure 5.35: Roll Rate Response for Bias Actuation with 0.5 Seconds Additional Power

It should be noted that if the aircraft is to return to level flight, the power times for both wings must be equal.

So, the turning characteristics of the aircraft can be altered by changing the delay between wing actuation and by powering each actuator longer. Essentially, to increase the maximum bank angle achieved during the roll, the delay between actuation of the first and second wings should be increased. To increase the time the aircraft remains at the maximum bank angle, the actuators should be powered for a longer time.

5.4.2: Differential Approach Performance

In the case of the differential approach, the results are significantly different. If one wing is actuated with one degree of twist, and then deactuated using the bottom wires, the following roll rate response is produced.

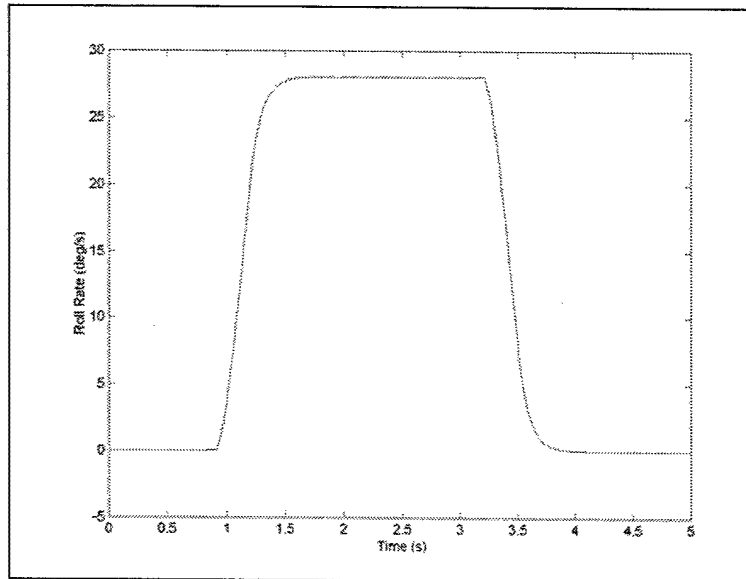


Figure 5.36: Roll Rate Response for Differential Actuation of One Wing (One Degree Wing Twist)

Comparing this graph to Figure 5.27, it is evident that the same maximum roll rate is achieved. The need to have the top wires cool to M_f before the bottom wires can be actuated means, however, that the aircraft must maintain the roll for a longer period of time, as shown above. The bank angle produced using the differential actuation of one wing is much larger than that produced by bias actuation, since the roll is maintained for a longer period of time.

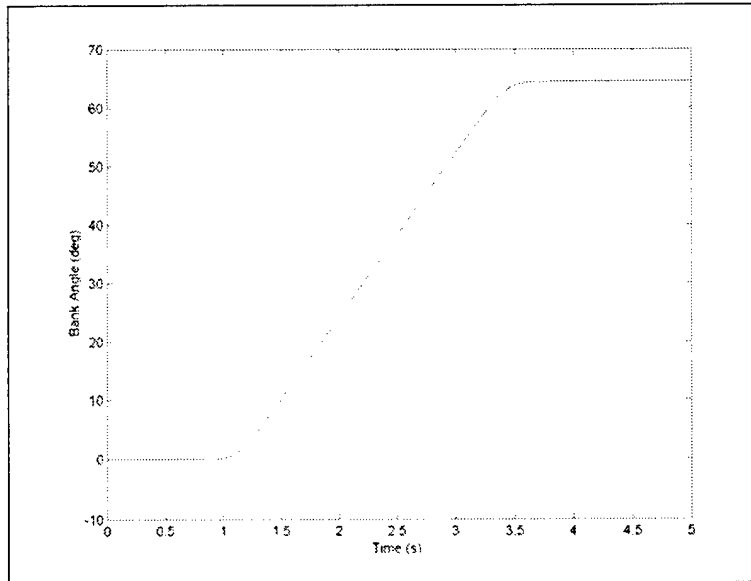


Figure 5.37: Bank Angle Response for Differential Actuation of One Wing (One Degree Wing Twist)

Like in the bias approach, the second wing must be actuated to return the aircraft to level flight. If there is a 0.1 second delay between actuation of the first and second wings, the following roll rate and bank angle responses occur.

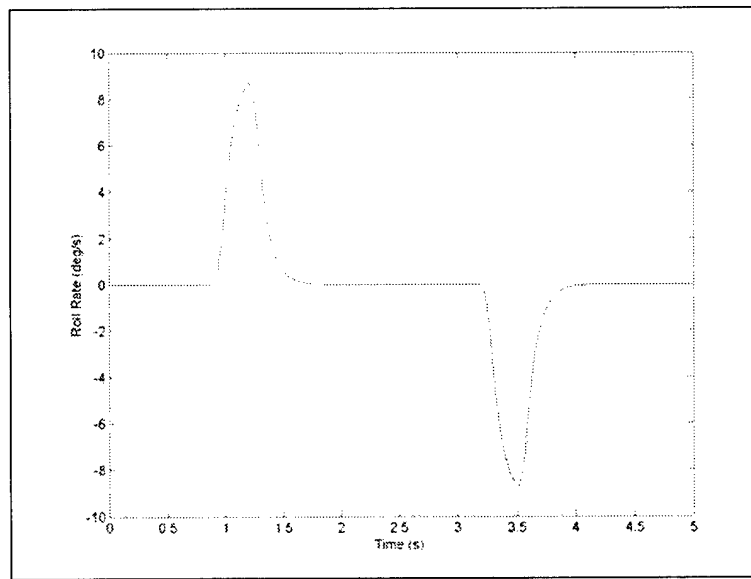


Figure 5.38: Roll Rate Response for Differential Actuation with 0.1 Second Delay

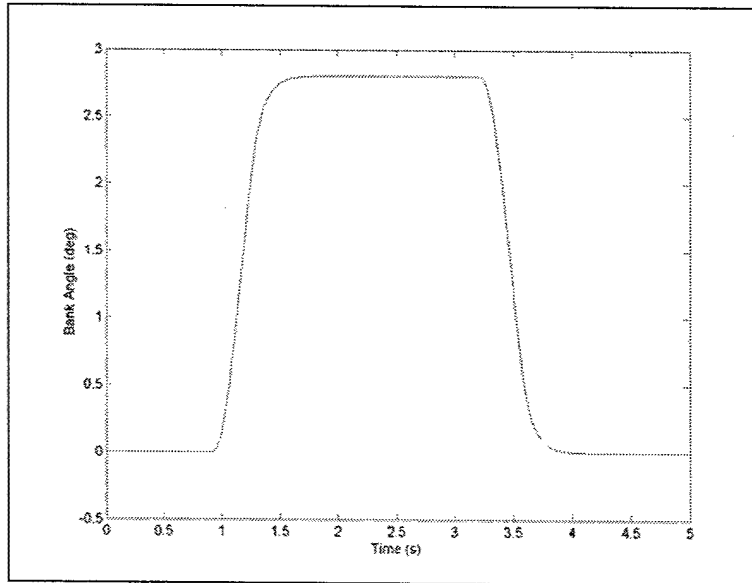


Figure 5.39: Bank Angle Response for Differential Actuation with 0.1 Second Delay

As in the bias approach, delaying actuation of the second wing for 0.1 seconds produces a maximum bank angle of just under three degrees. This bank angle is sustained for a much longer time using differential actuation, however.

If the delay is increased to 0.5 seconds, similar comparisons can be made between the bias and differential actuation schemes. As in the bias approach, an increased delay in the differential approach results in a larger bank angle.

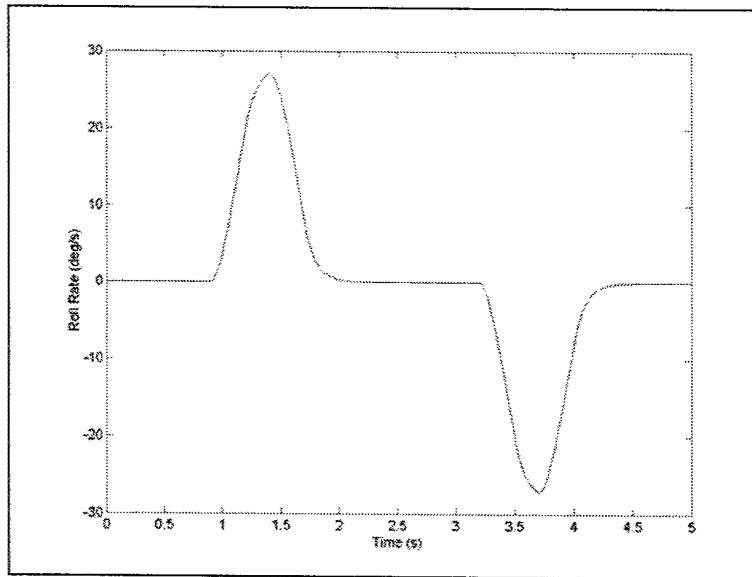


Figure 5.40: Roll Rate Response for Differential Actuation with 0.5 Second Delay

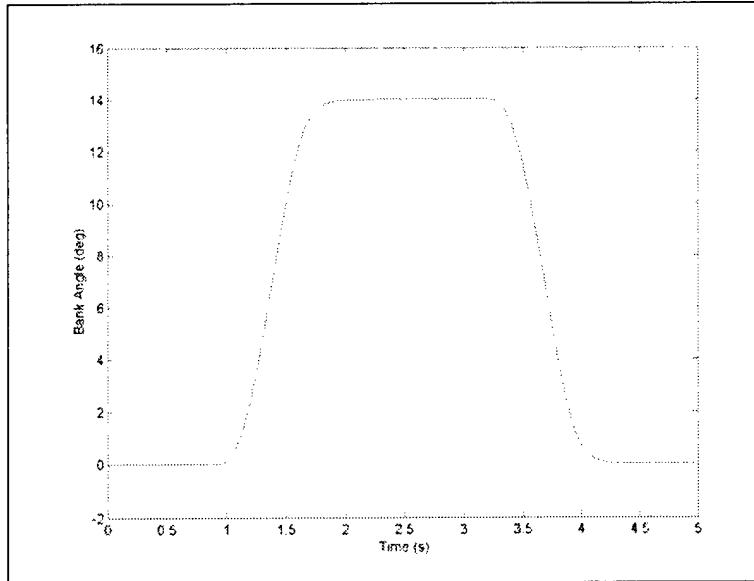


Figure 5.41: Bank Angle Response for Differential Actuation with 0.5 Second Delay

Finally, in the differential approach, there is a way to increase the time a particular bank angle is sustained. In the bias approach this was done by adding heat to the actuator to prevent it from cooling. Since in the differential approach the wing will not automatically untwist when it cools, this additional heat is not needed. The same effect can be gained by simply waiting a little longer before the bottom wires are actuated. If the differentially actuated wings with one degree of twist and a 0.5 second delay are held twisted for an additional 0.5 seconds, the following results are produced.

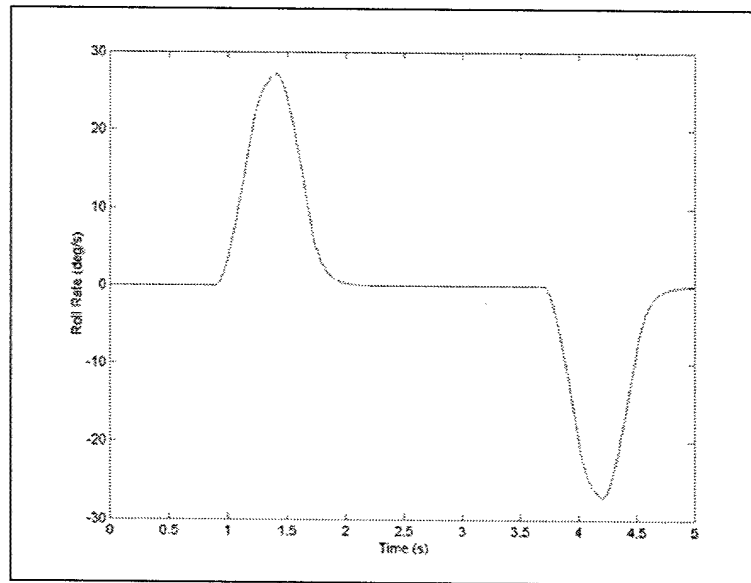


Figure 5.42: Roll Rate Response for Differential Actuation with 0.5 Seconds Additional Power

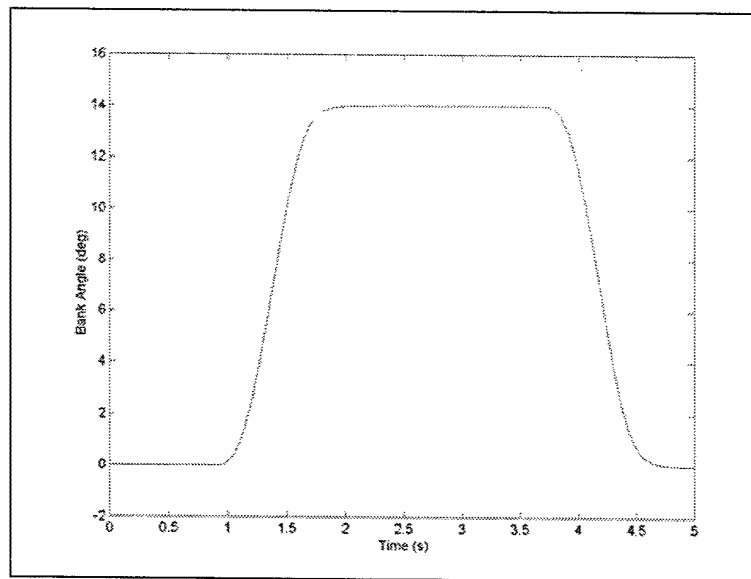


Figure 5.43: Bank Angle Response for Differential Actuation with 0.5 Seconds Additional Power

Clearly the same effect is achieved as in the bias approach, as the bank angle is sustained for a longer period of time.

5.4.3: Comparison

The bias and differential approaches each have strengths. In the case of the bias approach, the main advantage is the need for only one set of wires on each wing. This means that the bias approach results in a lighter aircraft as a whole. Having wires only on one side also means that the bias approach should take roughly half the power to actuate the wing. However, to sustain bank angles for a prolonged length of time, the bias approach must be used with additional power, as shown in Figure 5.35. In the end, this could possibly eliminate the power advantage of the bias actuator.

If bank angles are only desired for a small amount of time, the bias approach is the better choice. The need to wait for the top wires to cool before the bottom wires can be actuated in the differential approach means that the turn must be maintained for a longer period of time. There is a lower limit to how long the turn must be maintained in the bias approach as well, but it is far lower than that in the differential approach.

In situations when bank angles must be sustained for prolonged periods of time, the differential approach is advantageous. Since no power is needed to keep the wing twisted, as in the bias approach, the differential approach is more efficient in this type of situation.

Overall, both approaches have attractive qualities. More in-depth analysis is needed to determine which approach is better for this application.

5.5: Power Consumption

As stated in Section 5.1.1, the thermal analysis used to determine the time response of the SMA actuator assumed a current of 20 MA/m^2 . For 1000 micron wires, this translates to a current of 15.7 amps. If a wire length of one meter is assumed, Equation 5.1 predicts a wire resistance of 1.02 ohms. Therefore, using Equation 5.2, the peak power required to operate the actuator is 251.3 watts. The voltage required is 16 volts.

As mentioned before, the total cycle time for the bias approach is 3.2 seconds, which means that the wing can actuate at a frequency of 0.3125 hertz. However, current is applied to the wire for only 1.2 seconds of that time. It could be said that the actuator is “on” for 1.2 seconds. If the power required is scaled by the proportion of heating time to total cycle time, the average, or continuous power required for the actuation of one wing is 94.24 watts. If it is

assumed that the actuator will produce the amount of twist predicted in Section 5.2.3, then the continuous power can be divided over 3.29 degrees of wing twist to obtain a value of 28.64 watts/degree for the continuous power needed per degree of wing twist.

For the differential approach, the total cycle time is 3.5 seconds, which means an actuation frequency of 0.2857 hertz. For a full actuation of one wing, each actuator must be heated for a total of 1.2 seconds. This means that the continuous power required over the cycle is 172.32 watts. Assuming a wing twist 3.18 degrees as in Section 5.2.3, the continuous power needed per degree of wing twist for the differential approach is 54.19 watts/degree.

Since both wings may be actuated at the same time, it is possible that for the bias approach, both actuators will be “on” at the same time. This would mean that the peak power required is 502.6 watts. For the differential approach, the worse case scenario would be if all four actuators (2 on each wing) were “on” at the same time. A peak power of 1005.2 watts would be required.

[THIS PAGE INTENTIONALLY LEFT BLANK]

Chapter 6: Material Characterization Tests

In order to determine the exact properties of the SMA wire being used for the prototype, it was necessary to perform some mechanical tests. This chapter describes those tests and the results obtained in them.

6.1: Nitinol Wire

The thermal analysis results in the previous chapter indicated that for totally covered wires on the surface of the wing, the fastest time response for the heating and cooling cycle is found by using 1000 micron wire. Wire of this size was purchased from Shape Memory Applications Inc. [34]. Since this company sells many different Nitinol alloys, it was necessary to specify the desired type. For this application, alloy H was chosen because its A_f temperature is near 100 degrees Celsius. This Nitinol alloy contains no additional alloying elements along with the nickel and titanium. According to the company website, this alloy is 55 percent nickel and 45 percent titanium. This wire was bought in the straight annealed condition, meaning that after it was drawn, it was heated to remove any pre-strains. Because of the processing of the wire, it has a naturally forming oxide coating. The expected temperature hysteresis of this wire is 30 degrees Celsius.

6.2: Tensile Tests

Although published values for the mechanical properties of Nitinol exist, many of these properties are described in terms of a range of values, as in Section 2.5. For this reason, it was desirable to perform tensile tests to determine more accurate values to be used in analysis. Because the property values for Nitinol in the austenite and martensite phases are different, it

was necessary to perform two sets of tests. In the first set the wires were tested at room temperature. The second set tested the wire at a temperature above A_f .

6.2.1: Test Specimens

The first step was to construct test specimens to be used in the testing machine. Each specimen was constructed from a six-inch section of wire. In order to remove any pre-strain that may have resulted from the wire being spooled after it was annealed, it was necessary to heat the wire to above the A_f temperature prior to testing. Resistive heating was used to do this. However, connecting lead wires to the test specimen was made more complicated by the fact that soldering the leads directly to the Nitinol was not possible. To facilitate a connection, crimps were attached to each end of the Nitinol specimen. The lead wires, which were made from 16 gauge copper wire, were then soldered onto these crimps. Each specimen was connected to a power supply, and current was applied to heat the Nitinol to its austenite phase. This ensured that the wires had no pre-strain.

6.2.2: Test Setup

An INSTRON testing machine was used to perform the tensile tests. Since each of the specimens had crimps and lead wires attached at the ends, special care was needed to ensure that the machine's grips could hold the specimens in place. In addition, the specimens for the high temperature tests needed to be resistively heated during the test, forcing the specimen to be electrically insulated from the machine grips. For these reasons, plastic inserts were attached to each side of the grip using double sided tape.

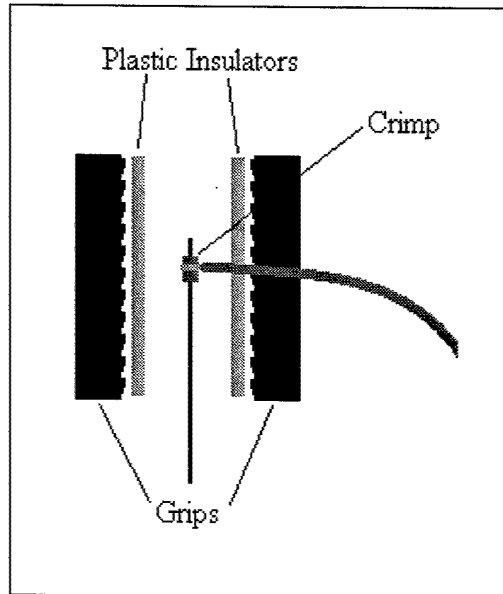


Figure 6.1: INSTRON Grip Setup

Once the insulators were attached, the specimen was inserted and the grips were tightened. Because the plastic was somewhat compressible, the crimped ends of the specimen sank into them, which added to the strength of the grip. After tightening the grips, the machine was adjusted to take any slack out of the wire.

6.2.3: Low Temperature Tests

For the low temperature tests, inserting the specimens in the grips of the INSTRON machine and adjusting the machine completed the mechanical setup stage of the experiment. Even though the lead wires were not used in these tests, they were left on the specimens so that the quality of the machine grip on the specimens was consistent between the high and low temperature tests. Next, the computer was set to collect data for the test, and the strain rate for the test was specified. In these four tests, the strain rate was varied to determine if it had a significant effect on the results for the modulus of elasticity for the data. One test was done at 0.02 in/min, one at 2 in/min, and two at 0.5 in/min.

As shown below, the results of the tests were very uniform. The modulus of elasticity of the Nitinol had an average value of 2.65×10^6 psi. This value is significantly lower than the value of 3.75×10^6 psi used in the structural analysis. The plateau in the stress-strain curves at

approximately 23000 psi is consistent with the expected behavior of the material in its martensitic form, since detwinning is occurring in this region.

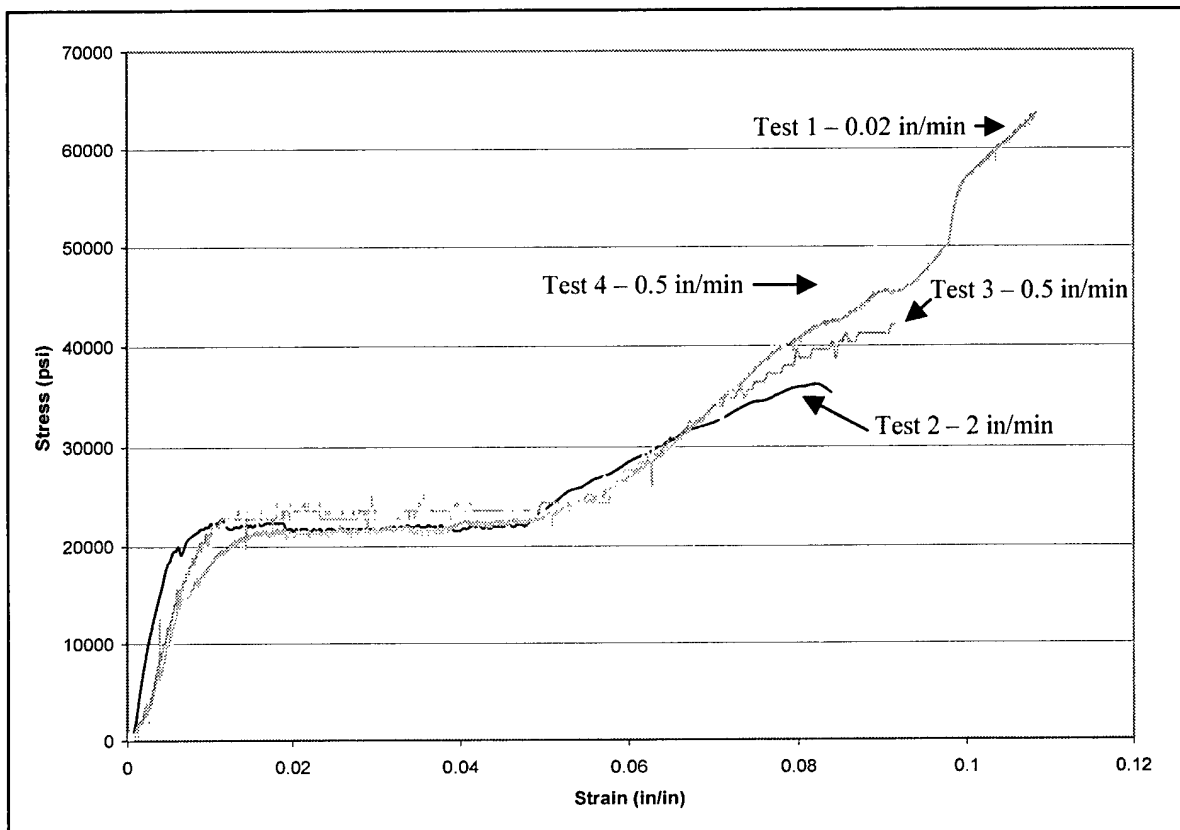


Figure 6.2: Stress vs. Strain Curves for Low Temperature Tensile Tests

6.2.4: High Temperature Tests

The setup for the high temperature tests contained all of the same steps as the low temperature tests, with a few important additions. Since these tests required that the wire be heated, the lead wires were connected to a power supply. To monitor the temperature of the wire, a thermocouple was attached to the wire using a small amount of thermal grease and foil tape. This thermocouple was connected to a thermocouple meter.

Before starting the test, the power supply was turned on and the wire was heated. The amount of current was manually controlled to achieve a steady state temperature of approximately 120 degrees Celsius. Once this temperature was obtained, the tensile test was started and data collection commenced.

Two tests were performed, and both used a strain rate of 0.5 in/min. As shown below, the results varied significantly between the two tests. In the first test, the Nitinol was found to have a modulus of elasticity of 6.32×10^6 psi. The second test showed this value to be only 4.01×10^6 psi. Not only do these values differ, but also they are significantly lower than the expected values for austenite. To understand both of these discrepancies, the description of stress-induced martensite in Chapter Two must be recalled.

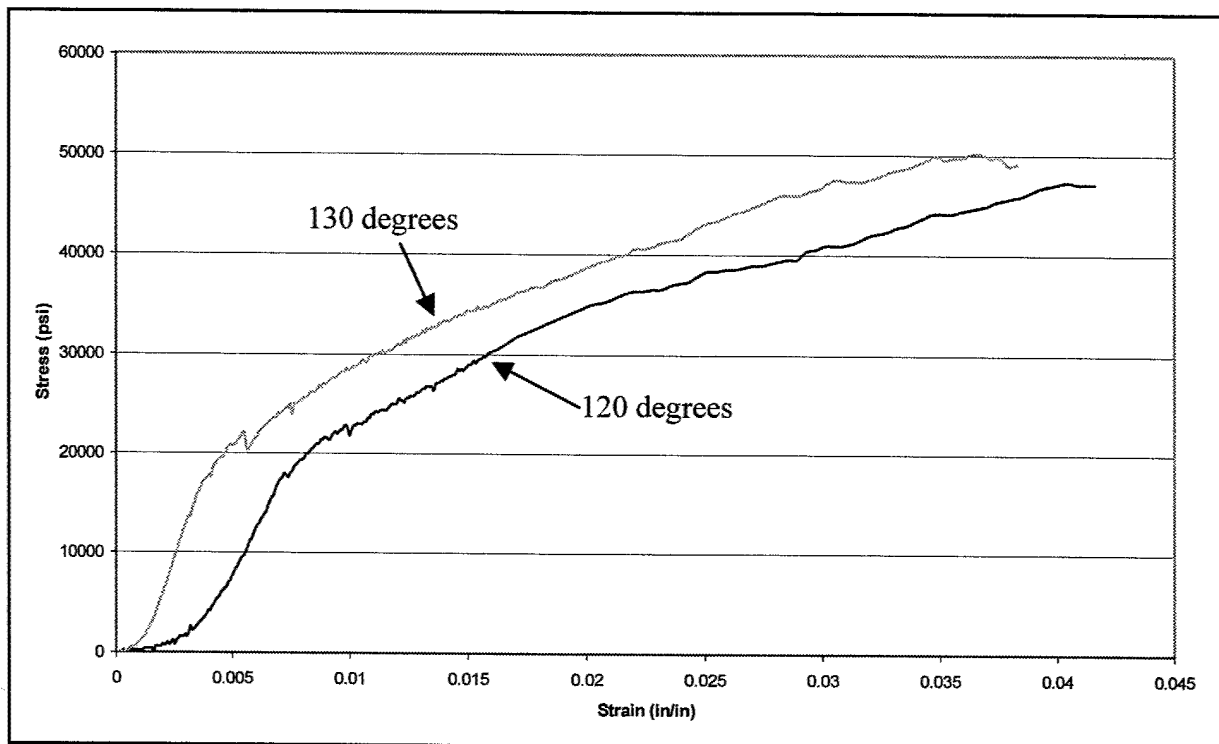


Figure 6.3: Stress vs. Strain Curves for High Temperature Tensile Tests

Since the temperatures of the wire during these tests were just above A_f , it is very likely that the temperature was below M_d , the maximum temperature in which stress-induced martensite can form. For this reason, as soon as the tensile test began and stress was added, portions of the wire began to return to martensite. The result of this is that the overall modulus of elasticity of the material was lower than that for pure austenite.

The explanation for the difference in the moduli between the two tests is centered around the effects of temperature on the ability of stress-induced martensite to form. The first test was conducted with the wire at 120 degrees, while in the second test the wire was closer to 130

degrees. It is evident that even this ten degree difference significantly changes the amount of stress needed to form martensite, which most likely accounts for the difference in the moduli.

As mentioned in Chapter Five, these tests were used to update the value for the modulus of elasticity of austenite in the structural models.

6.3: Cycle Tests

Although the A_f temperature of the wire was specified when it was purchased, verifying this value was important. Furthermore, the other transition temperatures were not specified. To determine these temperatures, a test was used to analyze the wire as it cycled between deformed and undeformed states. This test was largely modeled after the procedure used by Dr. Joe Ayers and his staff to train the SMA muscles used in his biomimetic robots [22]. The basic idea for this test is to place the wire specimen in a state of constant stress by hanging a weight from one end of the wire. This weight must be enough to deform the wire at low temperature. When the temperature is raised above A_s , the wire shortens. As the wire cools and changes back into martensite, it is deformed again by the weight.

6.3.1: *Test Specimen*

The test specimen used in this experiment was constructed in much the same manner as those used in the tensile tests. Crimps were attached to the ends of a length of Nitinol wire approximately eight inches long. Leads were soldered to the crimps, and resistive heating was used to remove any pre-strain from the wire. At this point, one of the crimps was cut off. A new crimp and lead wire were attached to the same end in order to have a distance of approximately five inches between the crimps.

6.3.2: *Test Setup*

Test Fixture

In order to conduct this experiment, a test fixture was designed and built. This cycle is shown below.

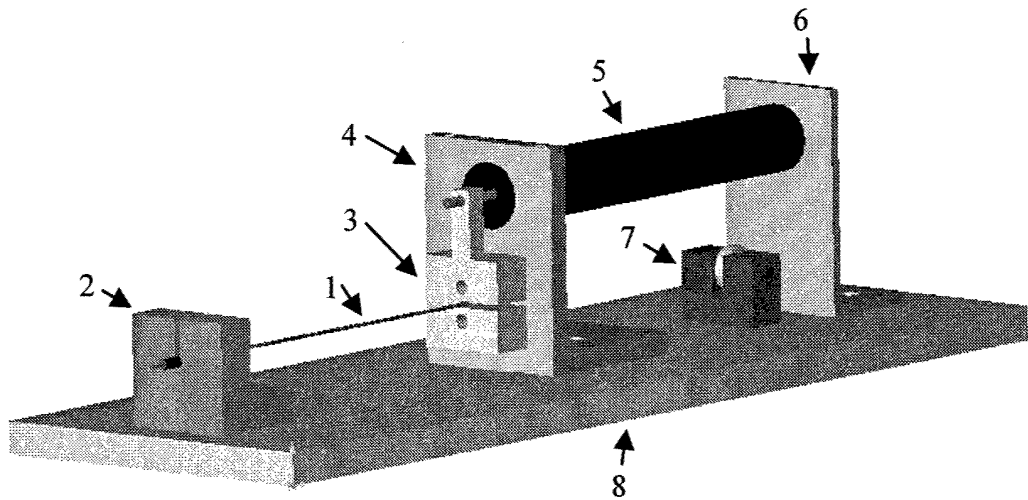


Figure 6.4: Test Fixture Diagram

In this figure, the main parts of the fixture are numbered. The Nitinol wire is part number one. Part two is a post with a slot to allow the wire to be slid into place. It is constructed of a polymer so as to electrically insulate the wire from the metal base plate, which is part number eight. Part three holds the other end of the Nitinol wire, and it is also constructed of a polymer. As the wire shortens, the crimp on the end pulls part three forward. Attached to the back of part three are two high-strength pieces of string, which loop over the pulley assembly and pass through a hole in the fixture, as shown in Figure 6.5. The pulley assembly is part seven. These pieces of string hold a weight, which pulls part three backward. This deforms the wire when it is in its martensite phase. As the wire changes length and part three moves back and forth, the core of the linear variable differential transformer (LVDT) is moved with it. This LVDT is shown as part five. Part four holds the front end of the LVDT and acts as a mechanical stop to prevent part three from moving past that point when the wire is stretched. Finally, part 6 holds the rear end of the LVDT.

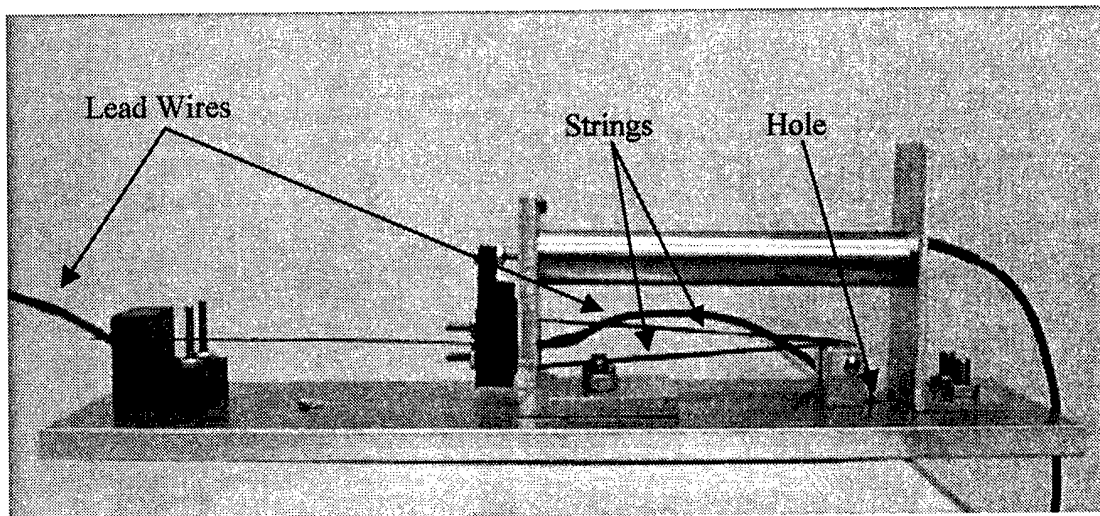


Figure 6.5: Test Fixture

Resistive Heating

The Nitinol wire was connected to a Kepco DC power supply using lead wires, as shown in Figure 6.5.

Instrumentation and Data Collection

During this test, two items were needed at each time interval: a temperature and a displacement measurement. In order to obtain the temperature of the wire, a K-type thermocouple was attached to the middle of the Nitinol wire. Since exposed junction thermocouples were used, a small amount of heat conducting epoxy was added to the junction to electrically insulate it from the Nitinol wire. A small piece of foil tape was used to secure the thermocouple to the wire.

The thermocouple was connected to an HP 34970A Data Acquisition Unit, which was set up to collect thermocouple readings. This Data Acquisition Unit was then connected to a laptop computer using a GPIB interface.

As mentioned before, an LVDT was used to collect displacement data. The LVDT chosen for this test was the Schaevitz DC-SE General Purpose LVDT. A DC power supply was used to power the LVDT. The LVDT was connected to a National Instruments DAQ-1200 card, which was connected to the laptop computer.

A LabView program was written to facilitate data collection with the laptop computer. This program collected the temperature reading from the thermocouple and the voltage produced by the LVDT. It also recorded the time at which each reading was taken.

6.3.3: Test Procedure

The first step in conducting the actual test was to insert the wire into the test fixture. At this point the thermocouple was attached and the weight was added to the end of the string to deform the wire. Once the wire was initially deformed, the test was ready to proceed. The LabView program on the computer was started, and the Kepco power supply was turned on.

The power supply was set to provide six amps of current when it was turned on. This current was left on until the temperature of the wire reached approximately 120 degrees Celsius. After the power was cut off, the wire was allowed to cool until it reached approximately 30 degrees Celsius. At this point the current was turned on and the cycle was repeated.

6.3.4: Test Results

Multiple cycles were performed on three different wire specimens to obtain a satisfactory amount of data. For each cycle, a data file was produced containing the time, temperature, and LVDT voltage data.

In order to make the LVDT data useful, it was necessary to perform some manipulation. Each voltage was compared with the overall voltage differential over the cycle to determine a percentage of the overall stroke. Once this manipulation was completed, the stroke percentage was plotted versus the temperature of the wire. A typical graph of one cycle is shown below.

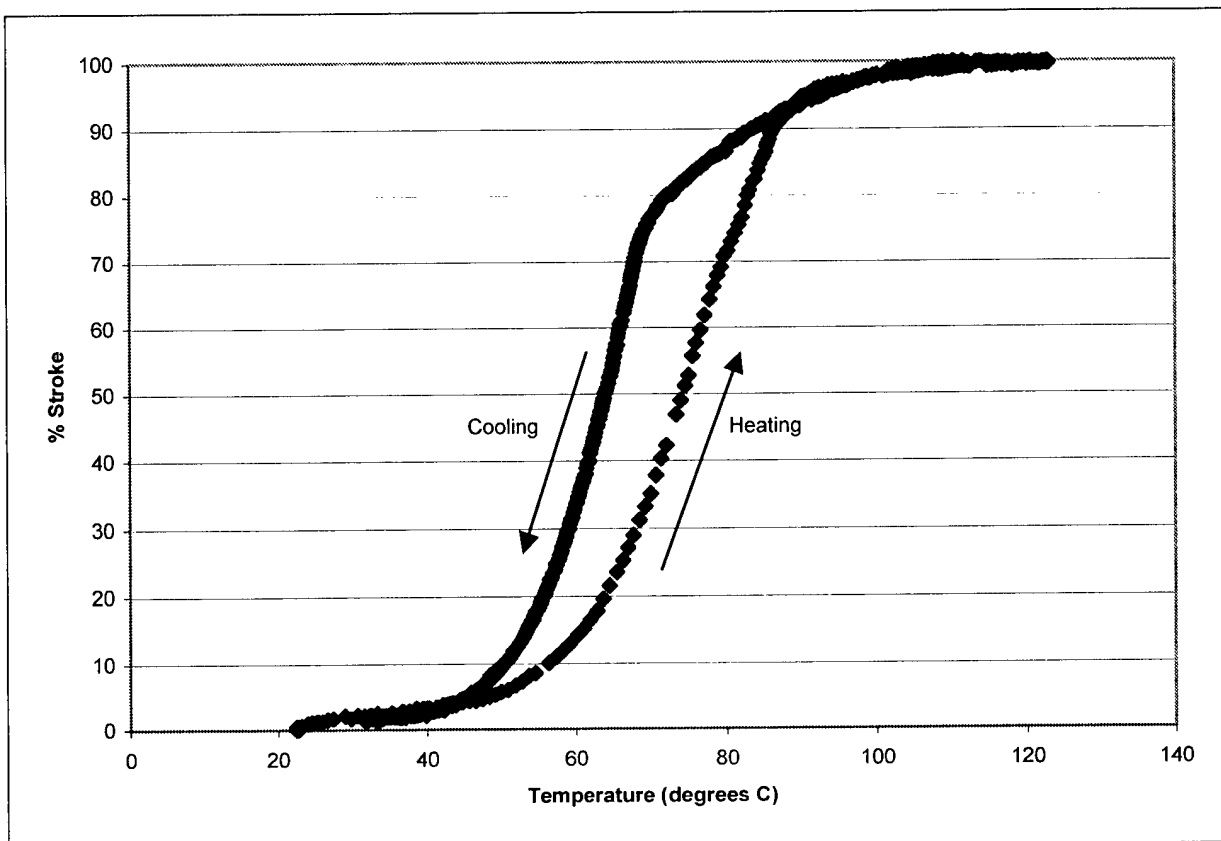


Figure 6.6: Typical Cycle Test Results

The results above clearly show the temperature hysteresis involved in transitioning from austenite to martensite and visa-versa. The difference in density of the data points on the graph shows that the wire heated much faster than it cooled. In order to determine the transition temperatures, however, additional analysis of the graph was needed.

Since each cycle produced a graph like Figure 6.6, a consistent method was needed to graphically determine the transition temperatures. The method chosen was based on the assumption that the transition temperature is the temperature at the point where best-fit lines intersect on the graph. As shown in Figure 6.7, these best-fit lines were added to each graph, and lines were projected from the intersections.

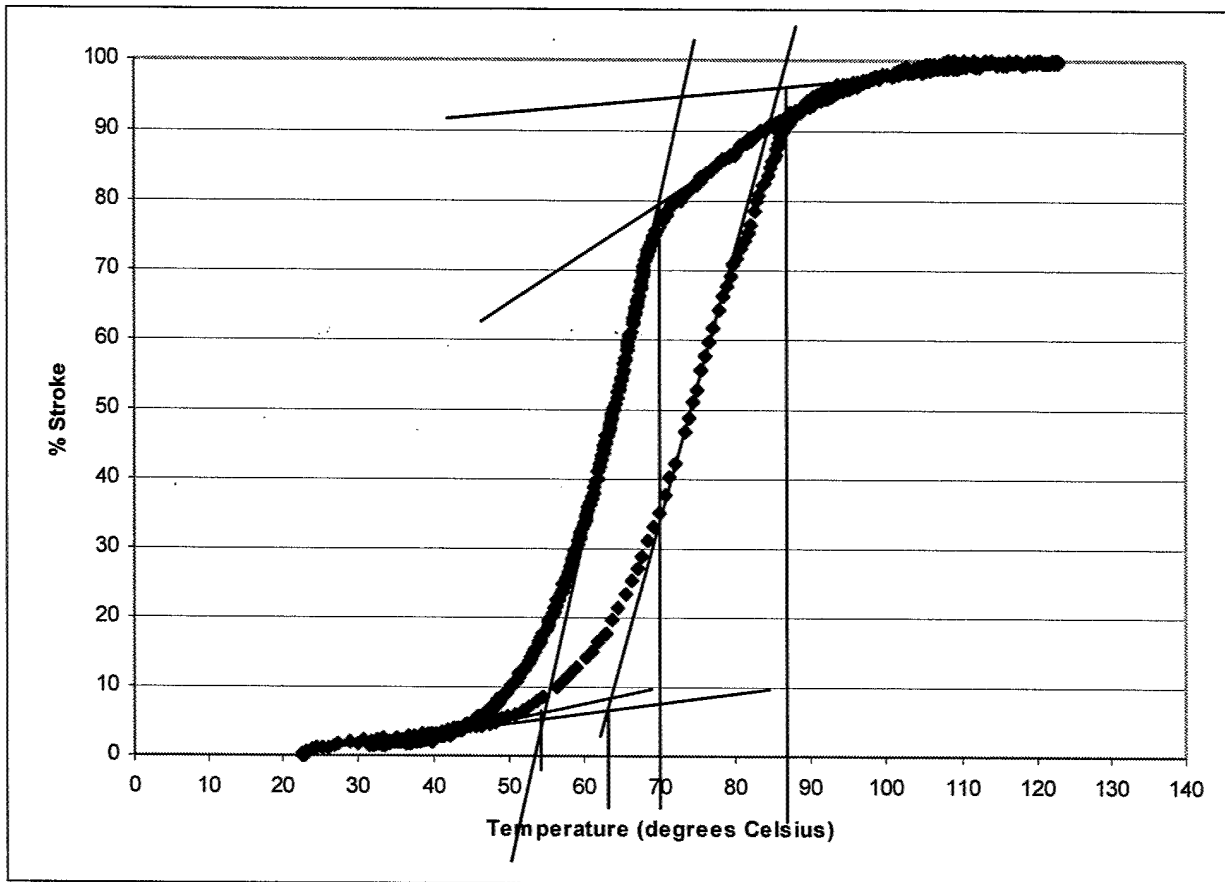


Figure 6.7: Transition Temperature Determination

These transition temperatures were recorded for each of the cycle, and an average was found. Based on these results, the experimentally determined transition temperatures for this Nitinol wire are as follows.

Table 6.1: Experimental Transition Temperature Results

Transition	Temperature (degrees Celsius)
A_f	88
A_s	61
M_s	72
M_f	54

The transition temperatures found using this experiment were significantly lower than those assumed in the modeling stage of this thesis. It was expected that the A_f temperature would be near 100 degrees Celsius. One possible cause for this difference is that the thermocouples were not reading the exact temperature of the wire. It is possible that the oxide coating on the

wire provided some thermal insulation from the junction of the thermocouple. It is also possible that the epoxy used to coat the junction did not fully transfer the heat of the Nitinol wire. Even if these transition temperatures are not accurate, they do provide an “indicated transition temperature” if the same method of attaching the thermocouples is used.

It must be noted that there was some variance between the average values obtained for each sample. As shown in the following table, the first specimen had a much higher A_f temperature than the other two samples. Additional testing on more samples should be done to further examine the variation in the transition temperatures.

Table 6.2: Transition Temperature Variance Between Samples (degrees Celsius)

Transition	Sample 1	Sample 2	Sample 3	Standard Deviation
A_f	94.7	87.3	86.8	4.40
A_s	63.7	61.2	59.4	2.14
M_s	72.3	71.9	70.6	0.90
M_f	56.3	53.3	53	1.84

Chapter 7: Prototype Construction and Testing

In order to test the actual performance of the actuator design, a series of tests were conducted on mock-ups of the WASP wing. A simplified rectangular test blank was used instead of fabricating the exact wing geometry. This chapter details the setup, procedure, and results for each of these tests. It also provides a comparison between the analytical data found in Chapter Five and the experimental data found in this chapter.

7.1: Construction

7.1.1: Lay-up and Curing of Test Blanks

The initial step in constructing the prototype specimens was to build sandwich plates of fiberglass and foam. This was done in MIT's Technology Laboratory for Advanced Composites (TELAC). These plates were built to match the dimensions used in the structural models of Chapter Five.

The core was constructed from a 0.25-inch sheet of Rohacell 31 foam. The core section for each specimen was cut to be 12 inches by 4 inches. On each side of the foam core, two layers of fiberglass pre-preg were attached. Woven plies were used for the inner layers, while unidirectional plies were on the outside. A diagram of the lay-up is included below.

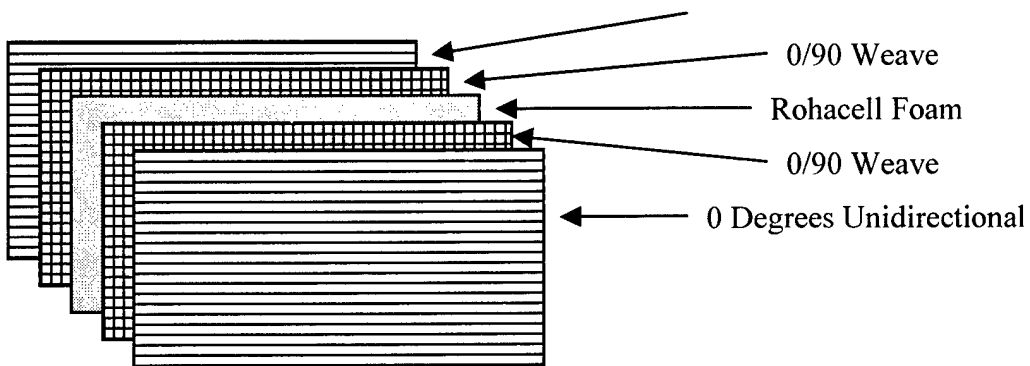


Figure 7.1: Lay-up Diagram

Once the initial construction of the specimens was complete, they were cured to solidify the epoxy bonds between the individual plies and between the inner plies and the foam core. A diagram of the cure setup is shown in Figure 7.2.

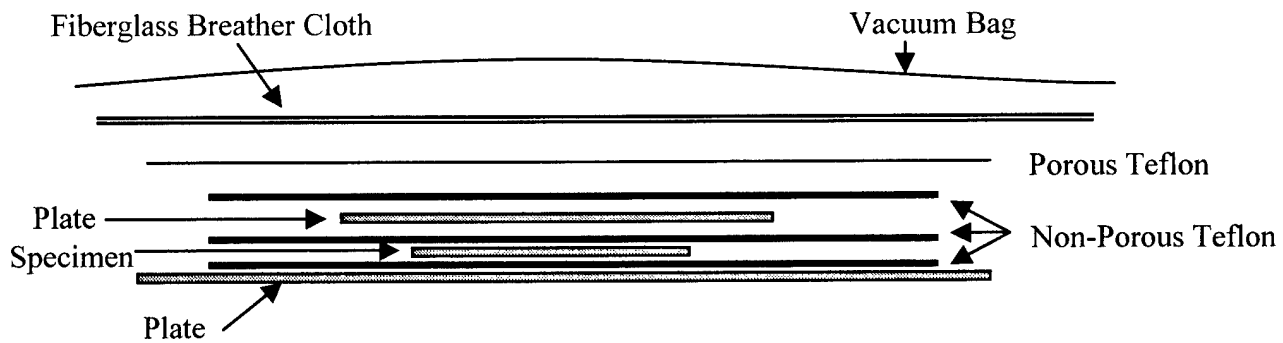


Figure 7.2: Cure Setup

The plates were cured in an autoclave for 90 minutes at a temperature of 260 degrees Fahrenheit. The pressure in the autoclave was set to 30 psi, and the vacuum bag itself was vented to the outside air to prevent vacuums from forming inside the foam. Once the cure time passed, the plates were cooled at a rate of five degrees per minute until the temperature reached 150 degrees. At this time they were removed from the autoclave and allowed to air cool to room temperature.

A diamond saw was used to cut the fiberglass/foam plates to the correct dimensions for the test specimens. Each plate was cut to be 11.5 inches by three inches. The extra half inch in the span direction was included to allow for clamping during testing.

7.1.2: Preparation of Nitinol Wire

As discussed in Chapter Five, the structural analysis of the wing test blank assumed that a Nitinol layer covered a 45 degree section of the wing. The layer was set to be 0.008 inches thick and spanned two inches in width if measured along the span, as shown below.

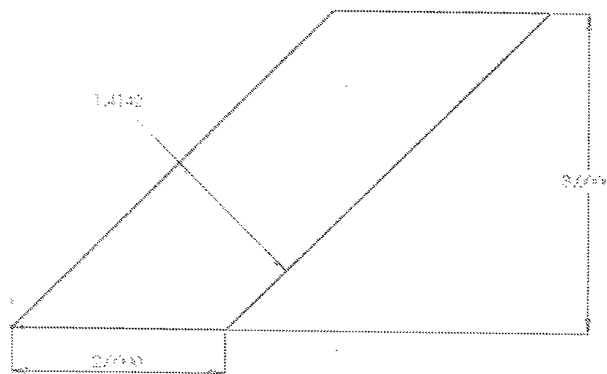


Figure 7.3: Dimensions of Nitinol Covered Area

Because the actual wires are one millimeter in diameter, it takes ten wires to achieve the same enclosed cross sectional area.

Since this design calls for the use of one bent wire instead of multiple smaller wires, a bend pattern was designed to arrange the wire over the same area covered in the structural model. This arrangement is shown in Figure 7.4. Each bend in the pattern has a radius of 0.0625 inches. This pattern calls for a wire with a length of just over one meter.

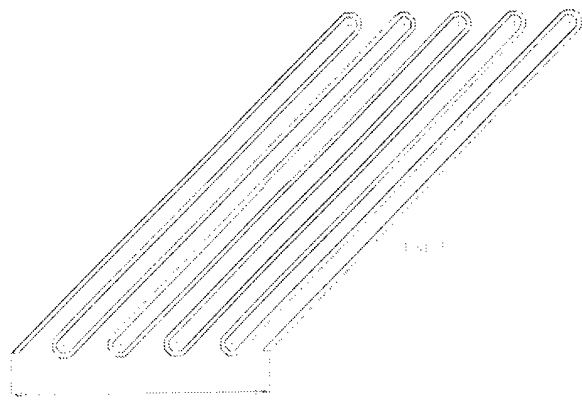


Figure 7.4: Wire Arrangement

Before the wire could be bent, some preprocessing was needed. As in the previous tests, it was first necessary to resistively heat the wire to above A_f . Once this was accomplished, the next step was to pre-strain the wire one percent. This was done using a specially designed fixture, as shown below. In this fixture, one end of the wire was held in a clamp. A crimp was attached to the other end of the wire, which rested against the back of the tensioning bolt. When the bolt was turned, the wire is stretched.

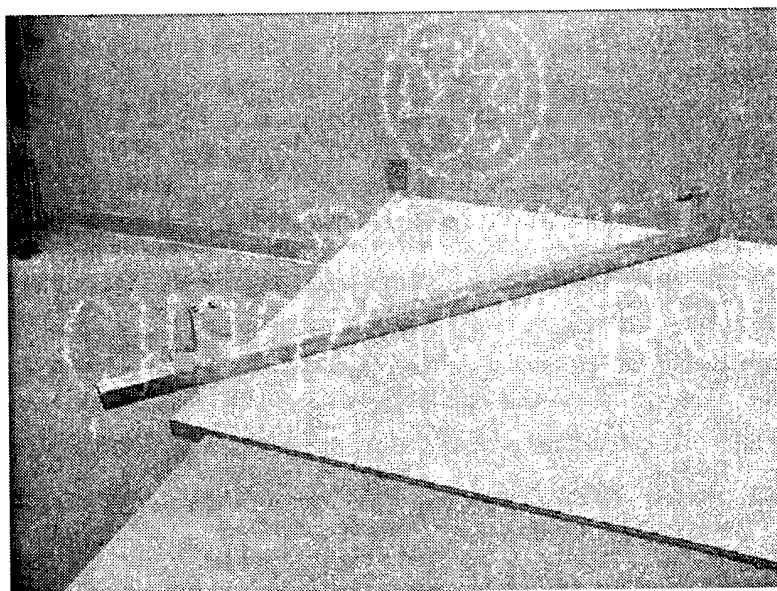


Figure 7.5: Pre-straining Fixture

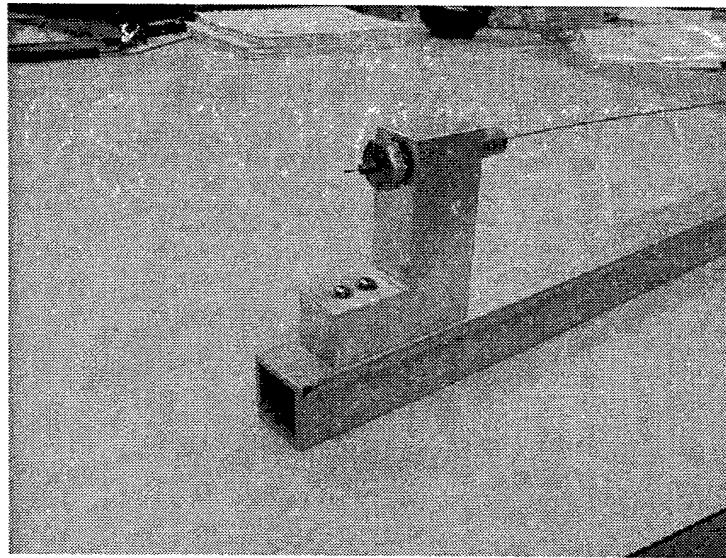


Figure 7.6: Bolt End of Pre-straining Fixture Showing Crimped End of Wire

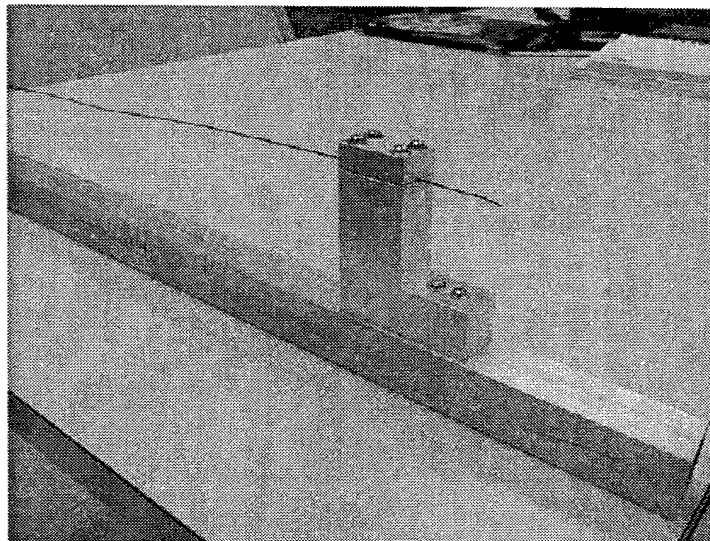


Figure 7.7: Clamp End of Pre-straining Fixture

Since the bolt had a known thread pattern, turning it resulted in a known strain. When the bolt was loosened, the elastic strain in the wire relaxed. Because of this, it was necessary to strain the wire past one percent to get a permanent one percent pre-strain. Through trial and error, it was determined that a gross strain of 1.9 cm was needed to deform the one meter long wire 1 cm, or one percent. This corresponded to 15 turns on the bolt.

After the wire was pre-strained, it was bent to the correct pattern using another fixture. A base plate with 0.125 inch diameter pins was used as a template for the bend pattern. A clamp

was also built into the structure to support one end of the wire as it was bent into shape. This fixture is shown in Figure 7.8.

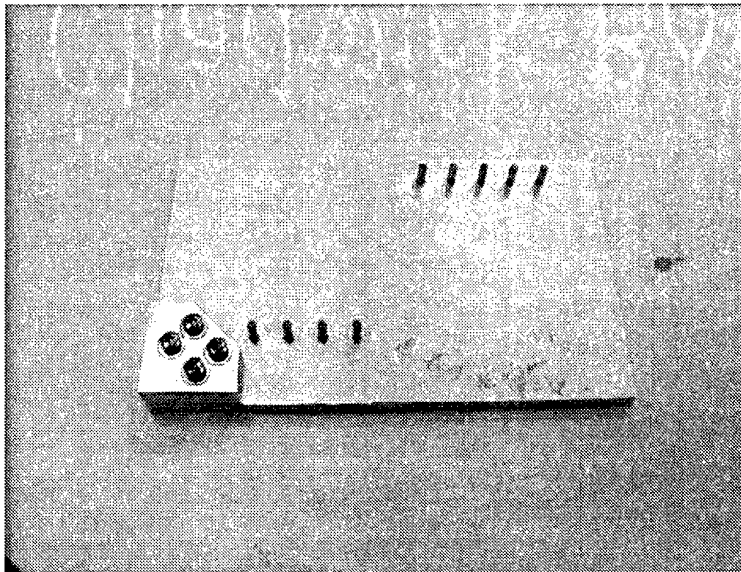


Figure 7.8: Wire Bending Fixture

7.2: Wires Attached with Epoxy

The first tests were conducted with the Nitinol wire attached to the wing using epoxy, as described in previous chapters. The setup, procedure, and results of those tests are detailed in this section.

7.2.1: *Tests One and Two*

The first two tests were used to determine the effectiveness of two epoxies in bonding the Nitinol wire to the wing. The first epoxy tested was Bond-It 7040 Super Bonder, which is produced by the Cotronics Corporation [35]. This adhesive is advertised as having bond strengths up to 5000 psi under temperatures up to 450 degrees Fahrenheit, and it was chosen specifically because it could maintain bond strength at high temperatures even though it cures at room temperature. The second epoxy tested was West Systems 105/205 [36]. This epoxy cures at room temperature, but it is not rated to withstand temperatures as high as the Super Bonder.

The need for epoxy that cures at room temperature was due to the pre-straining of the wire. Heating the wing, wire, and epoxy past the wire's A_f temperature to cure the epoxy would

have caused the Nitinol wire to recover its pre-strain, which would have eliminated its potential as an actuation device.

To attach the Nitinol wire to the fiberglass and foam test blank, a multi-step process was used. The first step was to tape the bent wire down in the proper pattern. Once this was completed, the bends in the wire were tacked down using superglue. After the superglue dried, the epoxy was prepared and applied to the surface of the wing and the wires. An aluminum block was used to apply pressure to the wires as the epoxy cured. The final result is shown in Figure 7.9.

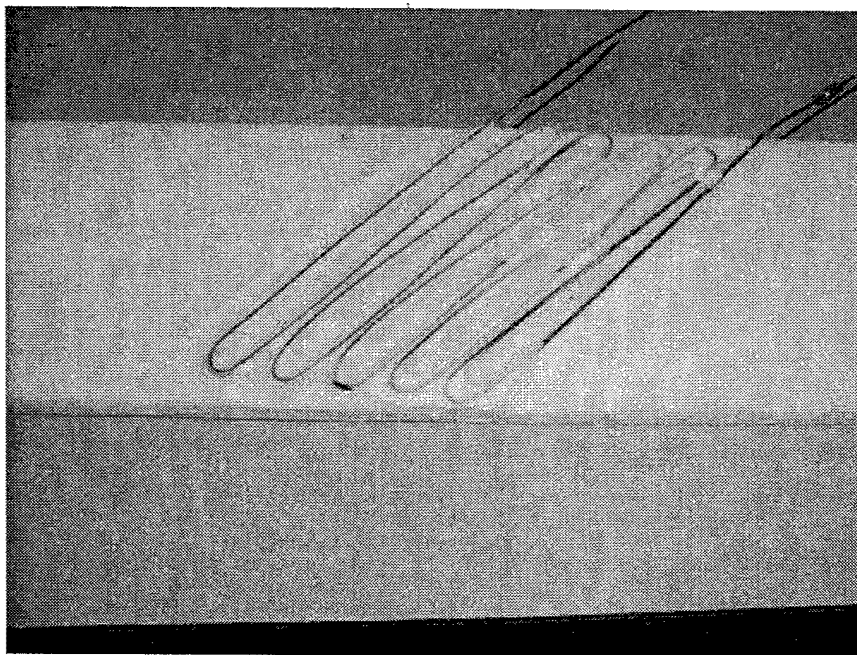


Figure 7.9: Nitinol Wires Attached With Epoxy

Both of these tests examined specimens utilizing the bias approach, where pre-strained wires were placed on only one side. The only instrumentation devices that were used on these two tests were the thermocouples used to monitor the temperature of the wires. As in the cycle tests in Chapter Six, these thermocouples were connected to an HP 34970A Data Acquisition Unit, which was connected to a laptop computer installed with LabView software. The K-type thermocouples were attached to the wire using foil tape. The Nitinol wire was connected to the Kepco DC power supply as in the previous tests. A small vice held the fixed end of the wing test blank. The test setup is shown below.

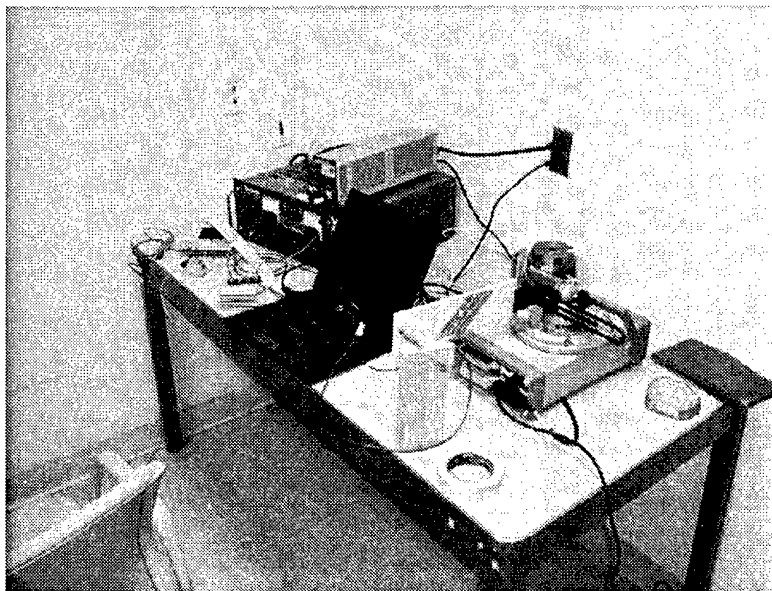


Figure 7.10: Setup for Tests One and Two

Once setup was complete, the LabView program was started and the power supply was manually activated. As the current flowed through the wire, the temperature was monitored on the computer. The power supply was shut off when either the temperature reached the predicted A_f temperature or when bond failure occurred. Any deflection of the wing test blank was visually monitored.

Due to an error connecting the thermocouples, the temperature measurements in these tests were inaccurate, which most likely resulted in the wires being overheated. Before the power supply was shut off, and before any noticeable deformation of the wing took place, the epoxy surrounding the wires in the middle of the wire pattern began to degrade. This resulted in these middle wires detaching from the wing in both tests. The test specimen before and after the second test is shown in Figures 7.11 and 7.12.

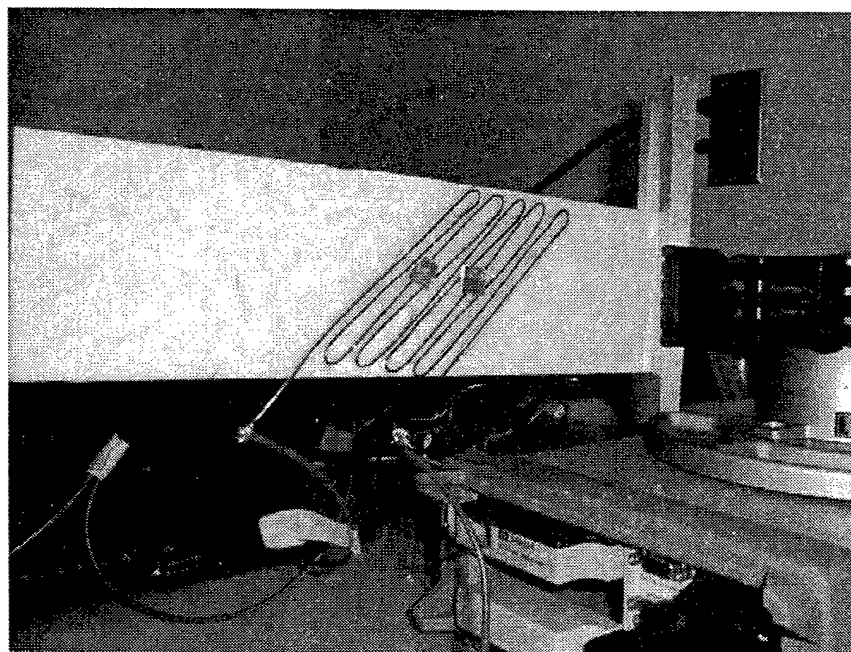


Figure 7.11: Test Specimen Prior to Test Two

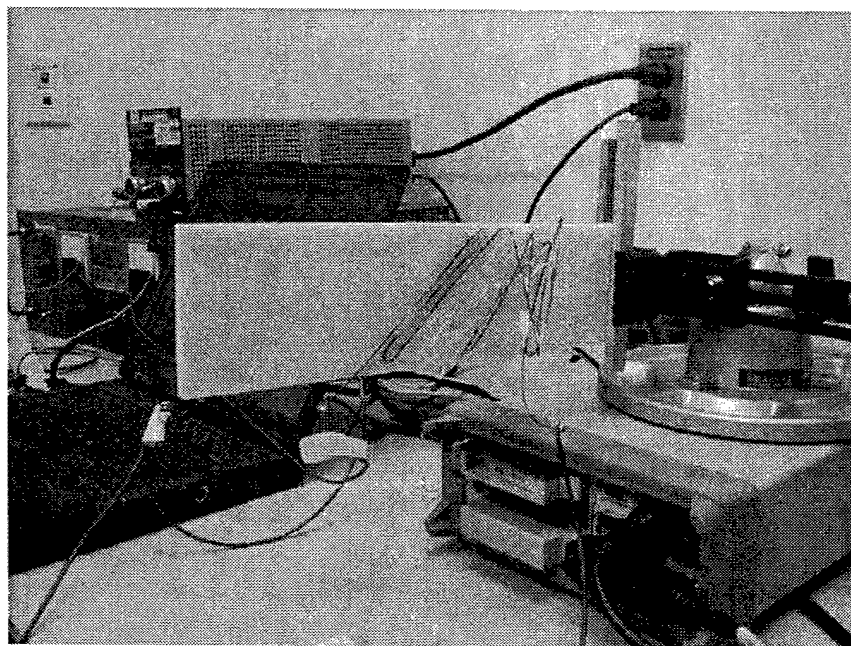


Figure 7.12: Test Specimen After Test Two, Showing Bond Failure

Since the West Systems epoxy was not rated to withstand temperatures near the A_f temperature of the wire, the failure of the epoxy in the second test was not a big surprise. In the first test, however, the thermal degradation of the epoxy was not the expected failure mode.

Given the advertised temperature tolerance of the Cotronics Super Bonder, it was expected that the cause of failure, if failure occurred, would be a lack of sufficient bond strength to hold the wires on the wing as they attempted to recover the pre-strain. The test results seemed to indicate that the Super Bonder could not withstand the heat produced by resistively heating the wires. This is the first possible explanation of the results in the first test.

The second possibility is that uneven heating of the wire along its length caused part of the wire to heat far past A_f while the rest was still far below that temperature. If that occurred, then the overheated wires may have caused degradation of the epoxy, which resulted in a bond failure. Since only part of the wire was over A_f , not enough of the wire had transitioned to cause visible deformation of the wing. Examination of the test specimens from both of these tests showed that the degradation of the epoxy began around the middle wires in the pattern. This seemed to indicate that the middle portion of the wires heated faster than the ends.

A third possible reason for the failure of the epoxy in the first test is that the rapid heating of the wire caused a rapid rise in temperature in the surrounding epoxy. It is possible that the epoxy can maintain a bond when the temperature gradually rises, but that it degrades locally if the temperature is increased at too fast a rate.

7.2.2: Test Three

Because the Cotronics Super Bonder was rated to withstand temperatures far above the A_f temperature of the Nitinol Wire, it was decided to run a test in a more controlled environment to verify that it could maintain a bond. A test specimen identical to that used in the first test was constructed. This specimen was placed in an oven and the temperature was set to gradually rise to 110 degrees Celsius. A thermocouple was inserted into the oven to monitor the temperature. This setup is shown in Figure 7.13.

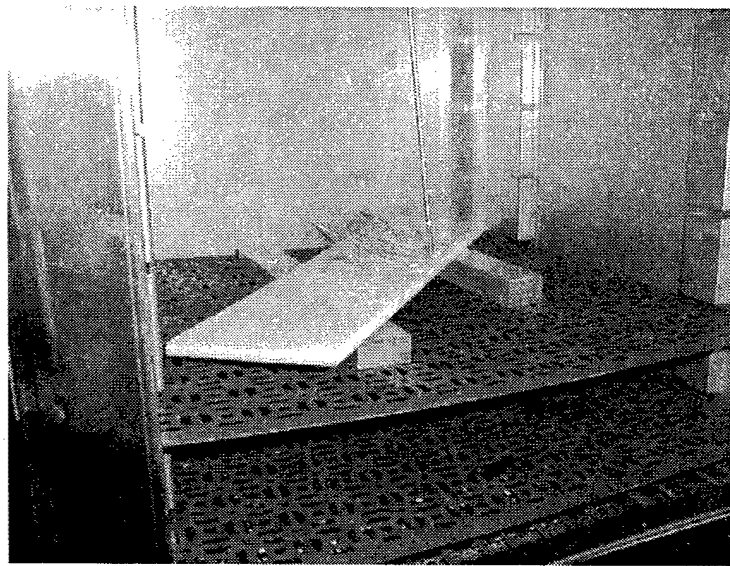


Figure 7.13: Oven Test Setup

After the temperature in the oven reached 110 degrees, the specimen was left in the oven for approximately ten minutes to ensure that the Nitinol wire had reached that temperature. Then the specimen was removed from the oven.

As shown below, the oven test resulted in significant twisting of the wing. Measurement showed that the wing twisted just over 3.5 degrees. Furthermore, inspection of the bond showed that the epoxy held the wires on the wing. As the wing cooled, it did not recover its previous shape.

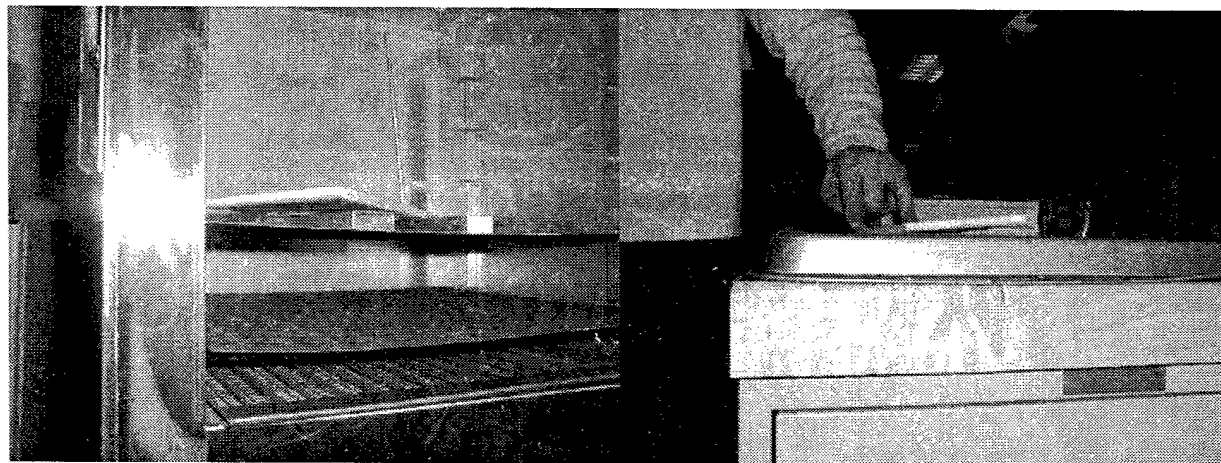


Figure 7.14: Wing Twist from Oven Test

The results of this test show that the Cotronics Super Bonder can survive the high temperatures needed to transform the Nitinol when the temperature is gradually increased. Furthermore, it showed that as long as the epoxy does not thermally degrade, the bond between the wire and the fiberglass surface of the wing is strong enough to hold the wires as they recover the pre-strain.

The fact that the wing did not return to the untwisted condition when the wire cooled seemed to indicate that the bias approach would not work for this particular wing lay-up and actuator pair, since the wing did not have enough stiffness to re-deform the wire. However, further consideration of the test revealed that the heating of the epoxy in the oven may have been the cause of the wing's failure to return to the original configuration. Because the epoxy was cured at room temperature, heating it in the oven may have acted as a secondary curing process. When the Nitinol wires deformed and twisted the wing, the epoxy may have cured around the wires and wing, making it impossible for the wing to deform the wires and un-twist when the Nitinol cooled.

7.2.3: Test Four

Because inaccurate temperature readings were produced in the first two tests, a fourth test was conducted on a test specimen using the Cotronics Super Bonder. In this test, a more sophisticated test setup was used that monitored both the temperature of the wires and the deflection of the test specimen.

As before, thermocouples were connected to the Data Acquisition Unit, which was connected to the laptop computer. Three thermocouples were attached to the wing using foil tape. Two Schaevitz DC-SE LVDT's were used to measure the deflection of each corner of the mid-span end of the wing test blank. As in the cycle tests, the LVDT's were connected to the laptop computer via a National Instruments DAQ-1200 card and were powered with a DC power supply. As shown below, the LVDT's were held in vices and the LVDT cores were connected to the wing using small linkages and threaded rods.

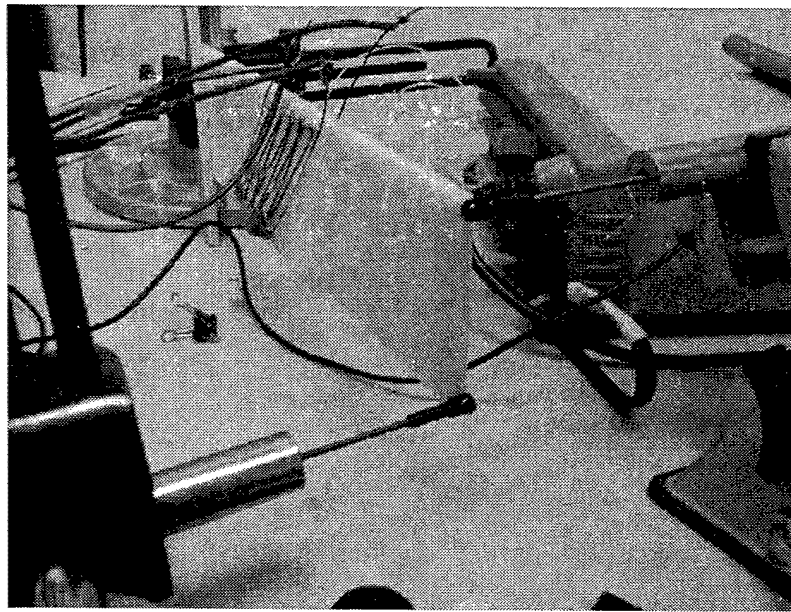


Figure 7.15: LVDT Setup

To begin the test, the LabView program was started and data collection was started. The Kepco power supply was turned on and a constant current of five amps was applied to the wire. When the temperature of the wire rose above A_f , the power supply was shut off. This cycle was repeated to obtain data for several actuation cycles.

This test produced mixed results. The initial actuation of the wing resulted in bond failure at multiple locations, but the failure was not catastrophic, so the test was continued. As in the first two tests, the bond failed because of the degradation of the epoxy, not because of insufficient bond strength. As shown in the following graph, the first actuation of the wing produced a wing twist angle of just under 0.7 degrees. It is notable that the bond failure did not occur in the middle of the wire pattern as in the first two tests. The first failures actually occurred near the end of the wire, indicating that uneven heating of the wire was not the true cause of the epoxy failure.

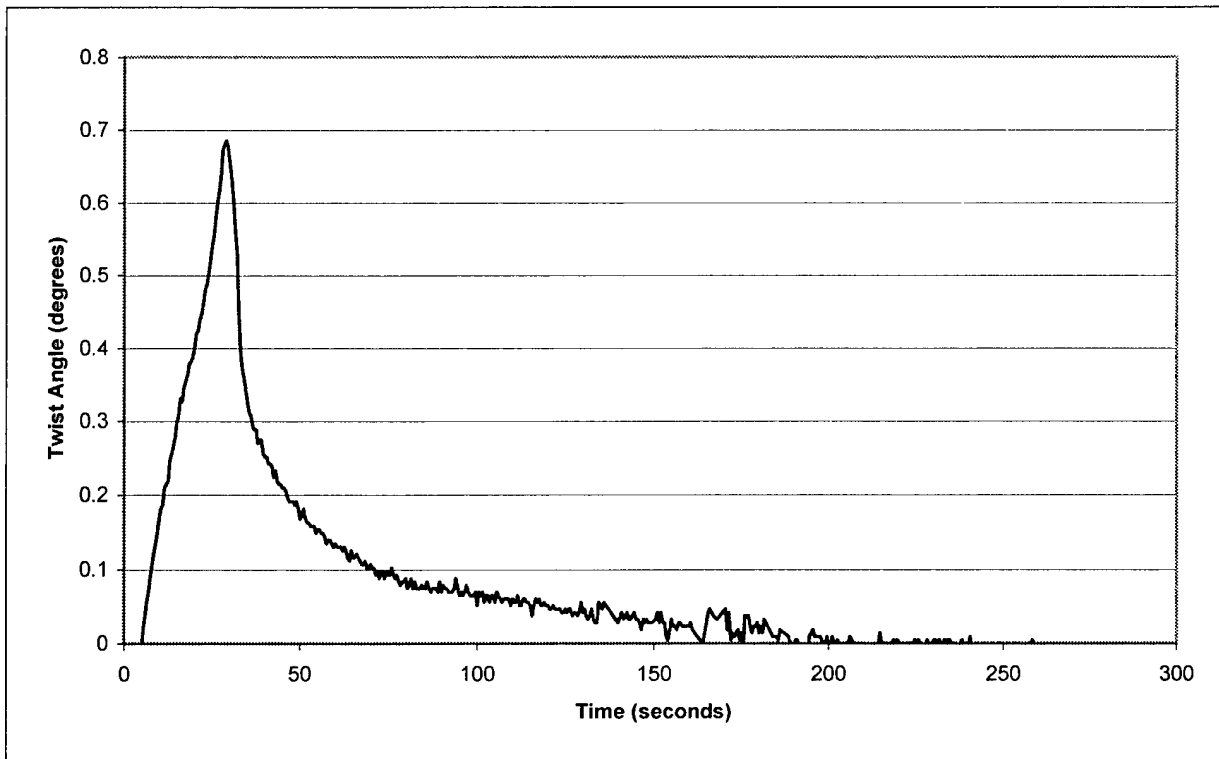


Figure 7.16: First Actuation of Epoxy Covered Wires

The subsequent actuation cycles produced decreasing amounts of twist. Figures 7.17 and 7.18 show the results for the third and fifth actuation cycles. As these tests were performed and the Nitinol wire stretched and contracted, more and more of the bond failed, which accounts for the sharp decrease in the amount of actuation.

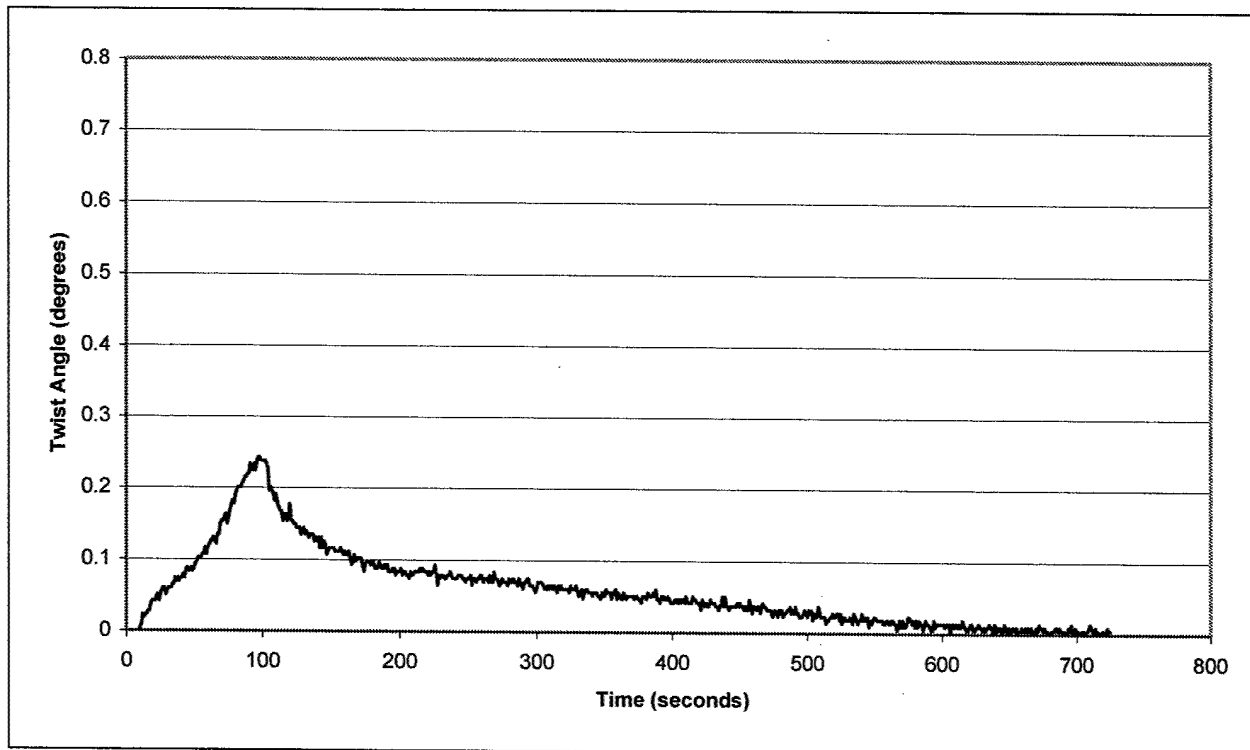


Figure 7.17: Third Actuation of Epoxy Covered Wires

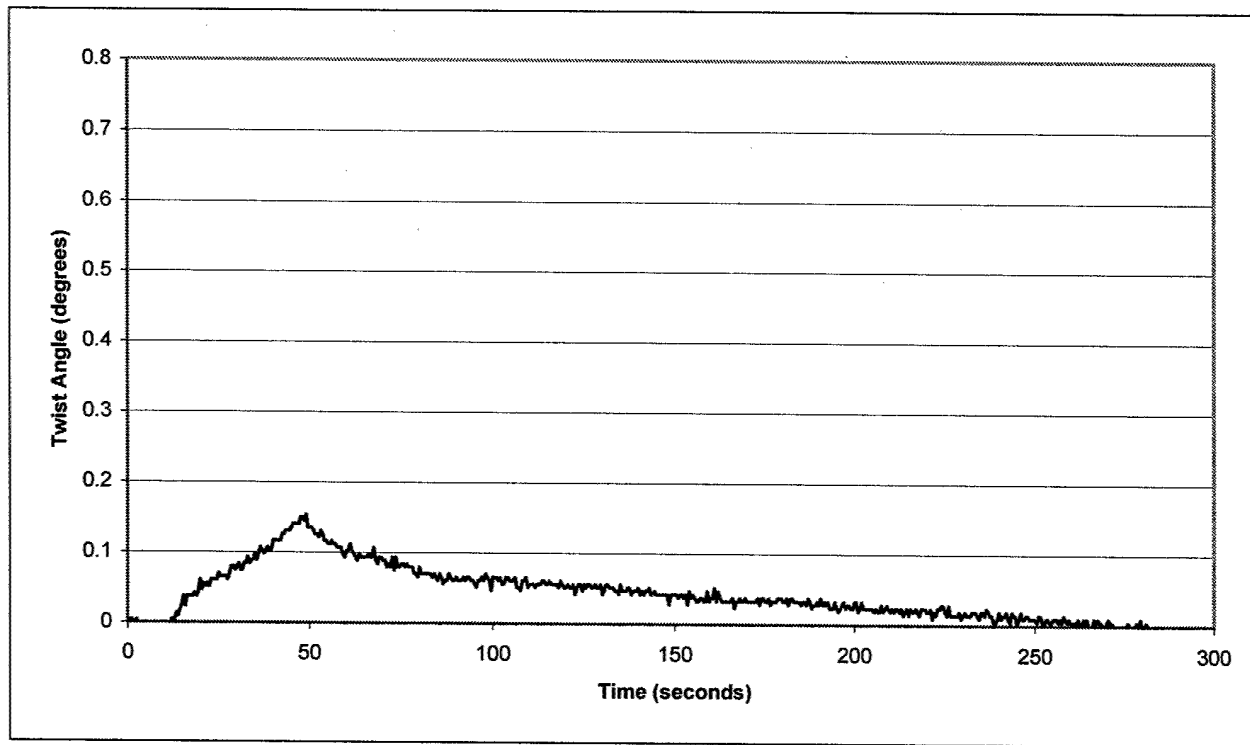


Figure 7.18: Fifth Actuation of Epoxy Covered Wires

One interesting result of these tests can be seen by examining one of the temperature vs. time graphs. As shown in Figure 7.19, there was a delay in the heating of the wire when the wire reached approximately 75 degrees Celsius. This temperature delay was seen on each of the test cycles.

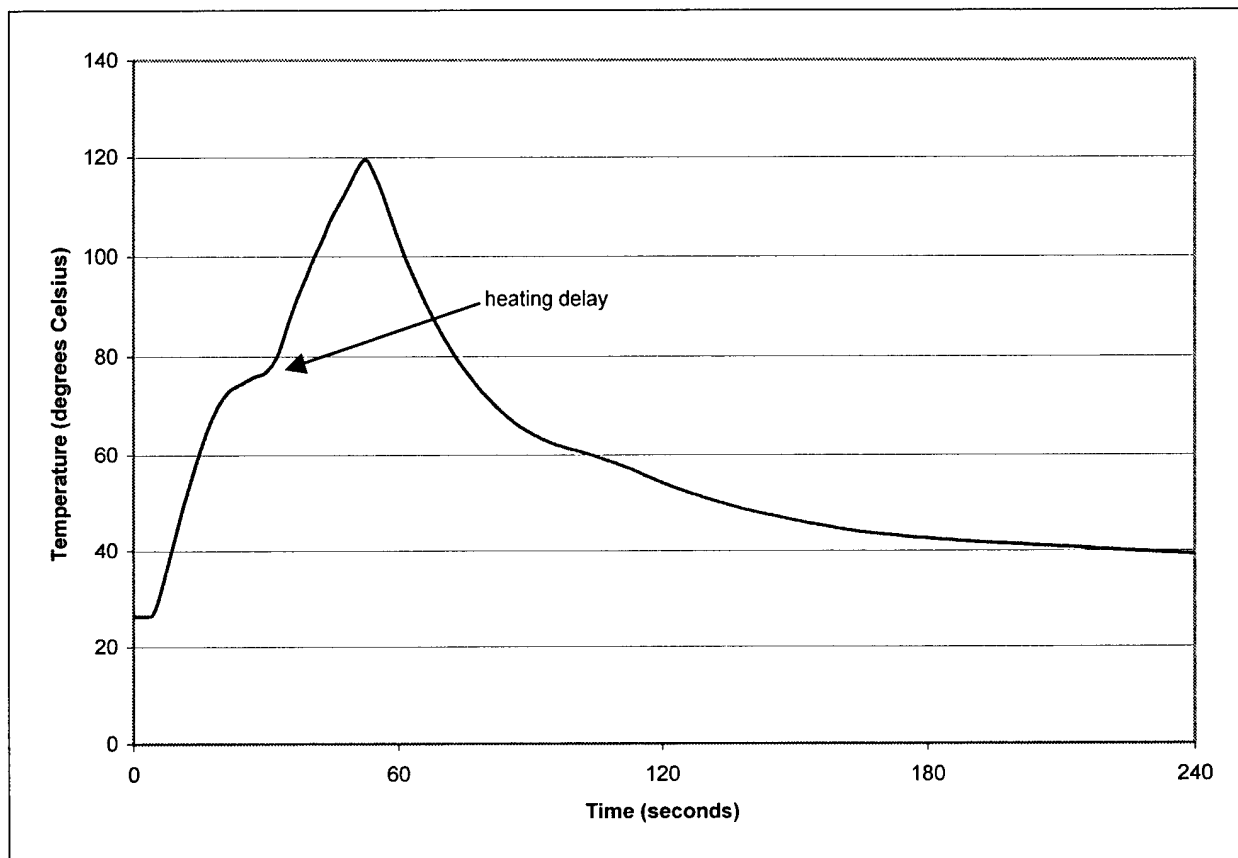


Figure 7.19: Heating and Cooling of Epoxy Covered Wires

7.2.4: Conclusion

While these tests do not completely rule out using epoxy to bond the wire to the wing, they do illustrate the difficulty in doing so. Based on the success of the oven test, the Cotronics Super Bonder can hold up to high temperatures. Test four also shows that uneven heating of the middle of the wire was not the cause of the degradation of the epoxy. The first and fourth tests show, however, that problems occur when the wires are rapidly heated. Of the three possible reasons for the failure of the epoxy listed in Section 7.2.1, this is the most likely. This problem would be compounded if the actual current of 15.7 amps, which was assumed in the thermal

analysis portion of this thesis, were used instead of five amps like in these tests. Furthermore, the heating delay shown in Figure 7.19 indicates a strange phenomenon occurring between the wire and the epoxy. This could be due to a property of the wire, or it could be due to a phase change in the epoxy.

7.3: Wires Attached with Pins

Because of the unsatisfactory performance of the epoxy bond, an alternative solution was examined. It was decided to insert pins into the wing test blank to provide a mechanical fixture for the Nitinol wires to react against. Nine holes, each 0.125 inches in diameter, were drilled into the wing in the exact pattern used for the wire bending fixture in Figure 7.8. After the wire was bent into shape on that fixture, it was placed on the wing around the pins. To secure the wire, Kevlar string was wrapped around the pins and the bent ends of the wire. The Cotronics Super Bonder was then used to secure the string and the terminal ends of the wire. The final product and a close up of the pins are shown in Figures 7.20 and 7.21, respectively.

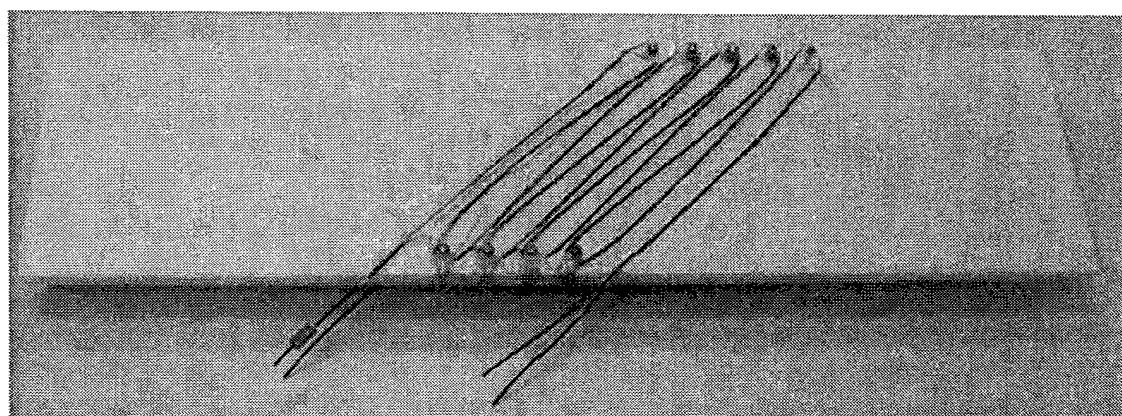


Figure 7.20: Nitinol Wire Attached With Pins

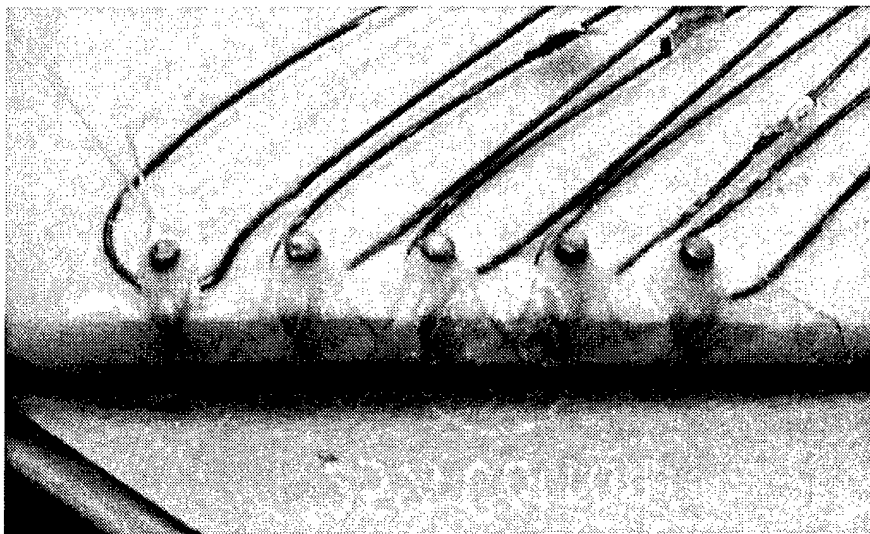


Figure 7.21: Enlarged View of Pins

7.3.1: Bias Test

The first set of tests conducted with this improved test specimen analyzed the bias approach. Pre-strained wires were attached to only one side of the wing. The setup for this test was identical to that of test four in Section 7.2.3, with one exception. Because the wires were not attached to the wing between the bent ends, it was possible to loop the foil tape around the wire, which ensured a better connection between the thermocouple and the Nitinol wire.

After the test was setup and the data collection system was activated, the power to the Nitinol wire was turned on and the test began. A current of five amps was used to power the actuator. As the wire was heated, the wing twisted to approximately 3.2 degrees. When the temperature of the wire reached approximately 125 degrees, the power was shut off and the wire was allowed to cool. As shown in Figure 7.22, the wing recovered a large portion of the twist induced by the actuator, but it did not fully untwist. After the wire had cooled to near room temperature, there was still over one degree of twist in the wing.

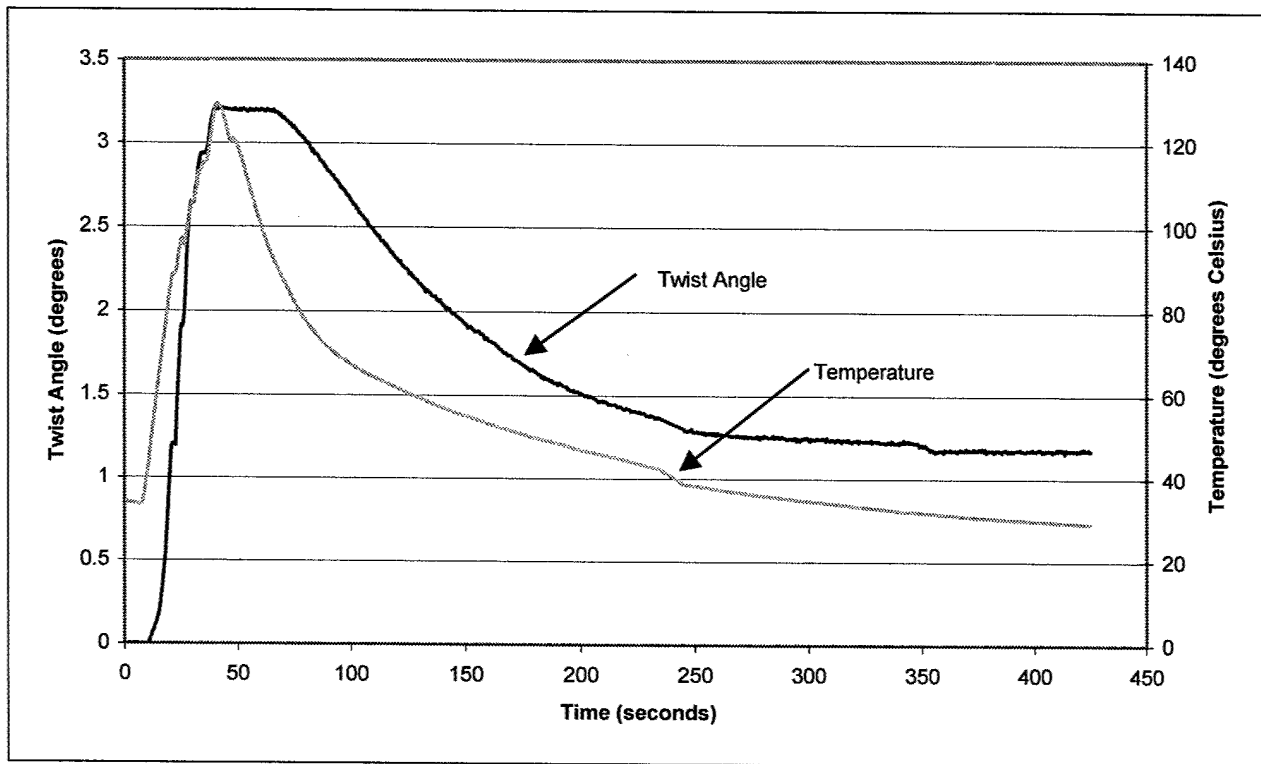


Figure 7.22: First Actuation Cycle

The second actuation cycle produced different results. As the wire was heated, the wing twisted to approximately the same overall angle. However, upon cooling, it recovered back to the angle at which it had started before the second cycle was begun. This is shown below.

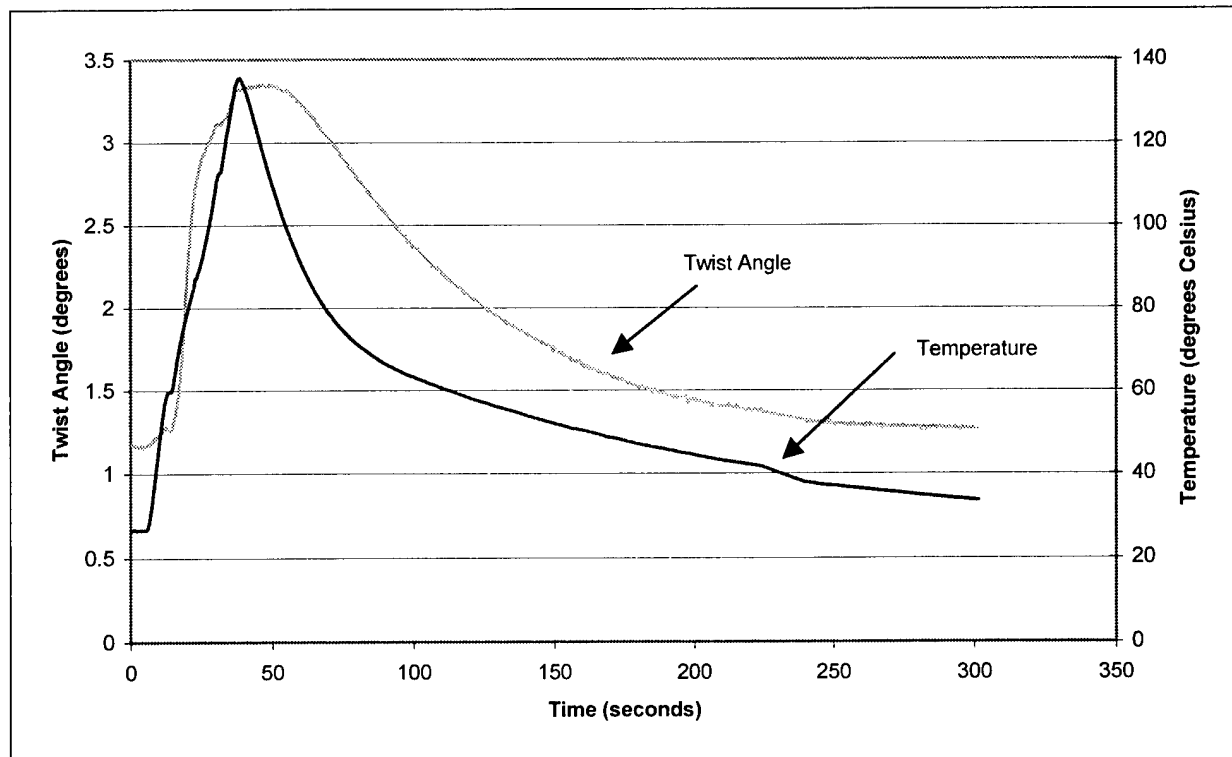


Figure 7.23: Second Actuation Cycle

The next few cycles showed a gradual decrease in the amount of wing twist produced by the actuator. However, whatever twist the actuator produced was recovered when the wire cooled and the stiffness of the wing re-deformed the wire. Several more actuation cycles were run, and in the end it appeared that the performance of the actuator leveled off. As shown in the following figure, the actuator seemed to settle into a fairly consistent performance envelope.

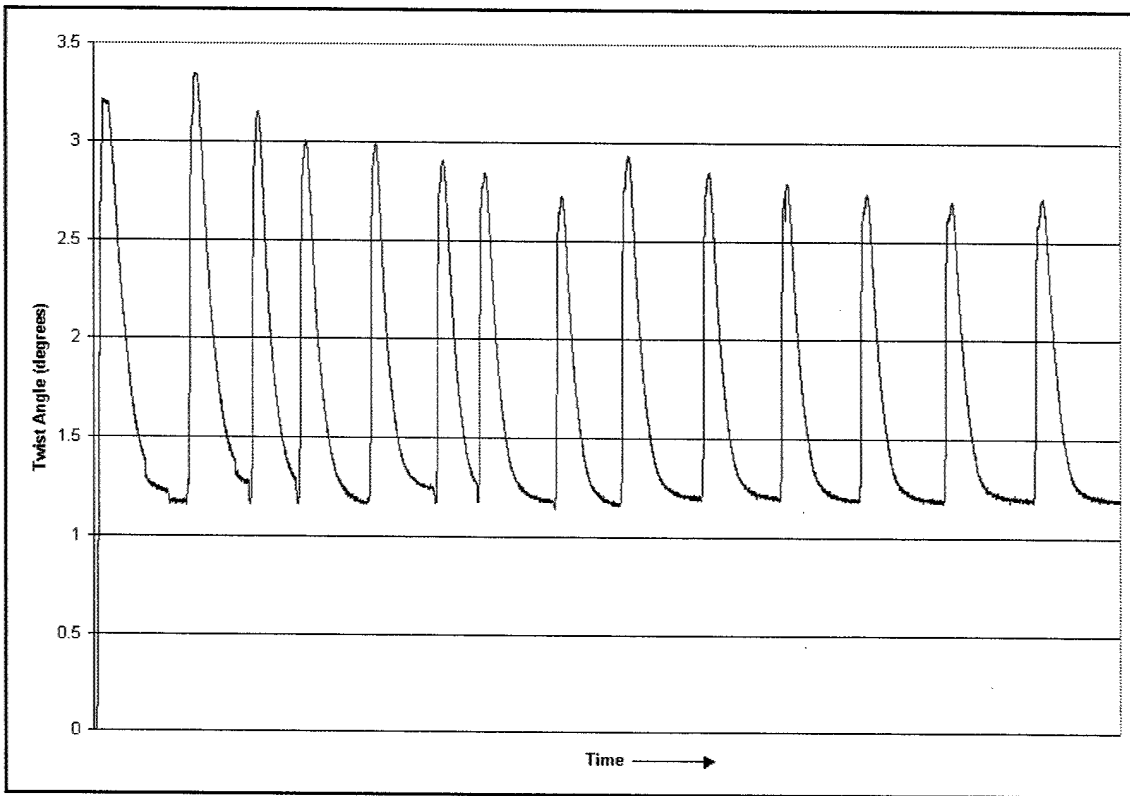


Figure 7.24: Twist Angle Evolution with Bias Actuation

7.3.2: Differential Test

A similar test was run on a test specimen to analyze the differential approach. Pre-strained wires were attached to the top surface of the wing, while un-strained wires were attached to the bottom side. The same test setup was used as in the previous test, except now three thermocouples were attached to each side of the wing.

The pre-strained wires were heated past the A_f temperature and then allowed to cool, and the deflection and temperature readings were recorded as before. Once the top wires cooled, the previously un-strained bottom wires were heated. The bottom wires, which had been strained by the twisting of the wing caused by the top wires, now contracted and twisted the wing in the opposite direction. Once these wires cooled, the cycle was repeated.

In the analysis of the differential approach in Chapter Five, it was assumed that the wing would not recover any of the twist produced by actuation of the top wires. The bottom wires would need to be actuated to return the wing to the un-twisted condition. However, the test cycles in the previous section show that the wing does indeed have the stiffness needed to

recover at least a portion of the twist. For this reason, it was known that this test was actually a test of a system with characteristics of both the bias and differential approaches.

The first actuation of the top wires produced a wing twist of nearly 2.5 degrees counterclockwise to the span axis of the wing. This is lower than that produced by the first actuation of the wires in the previous section. The smaller amount of twist was due to the additional stiffness in the wing stemming from the wires on the bottom side. As the wires cooled, the wing recovered to a twist angle of 0.6 degrees. This larger recovery was also due to the increased stiffness of the wing with wires on the bottom surface.

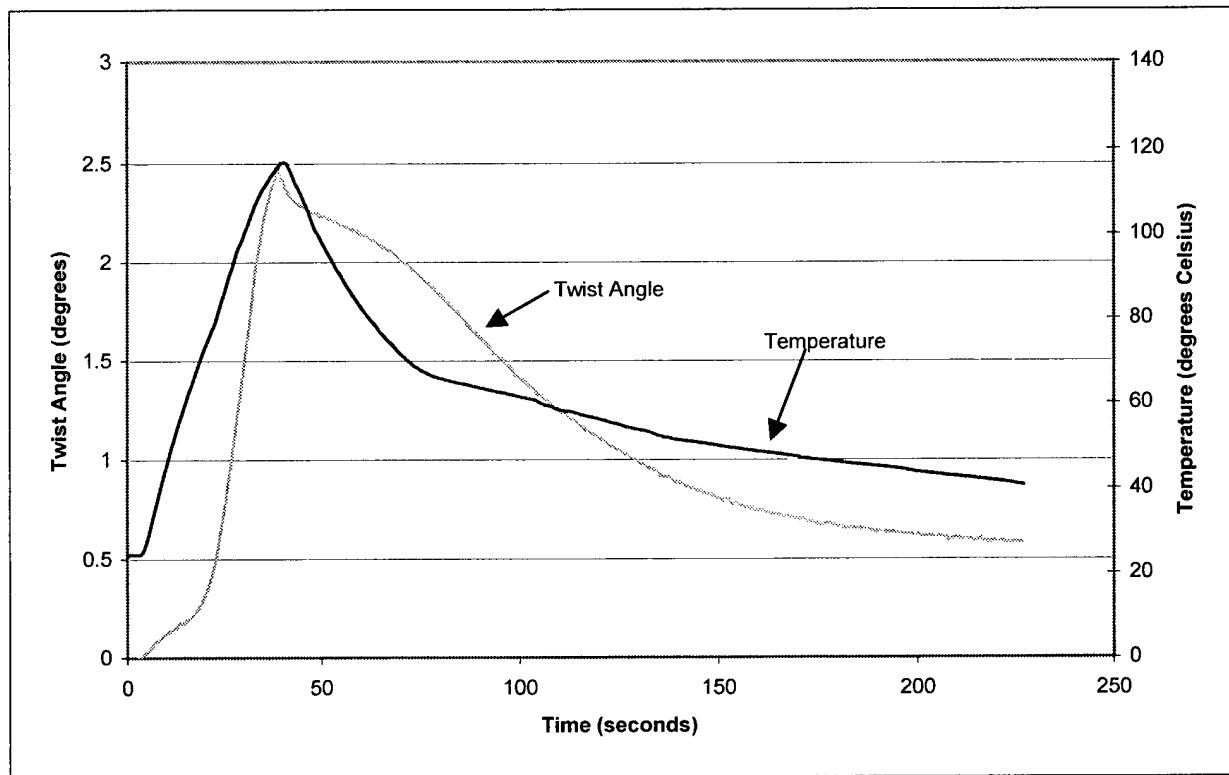


Figure 7.25: First Actuation of Top Wires

The subsequent actuation of the bottom wires caused the wing to twist past zero degrees and to a twist angle of nearly two degrees clockwise, as shown in Figure 7.26. Twist in this direction is defined as being negative. When the bottom wires cooled, the wing recovered some of the twist, but it stopped at 0.3 degrees of twist in the clockwise direction.

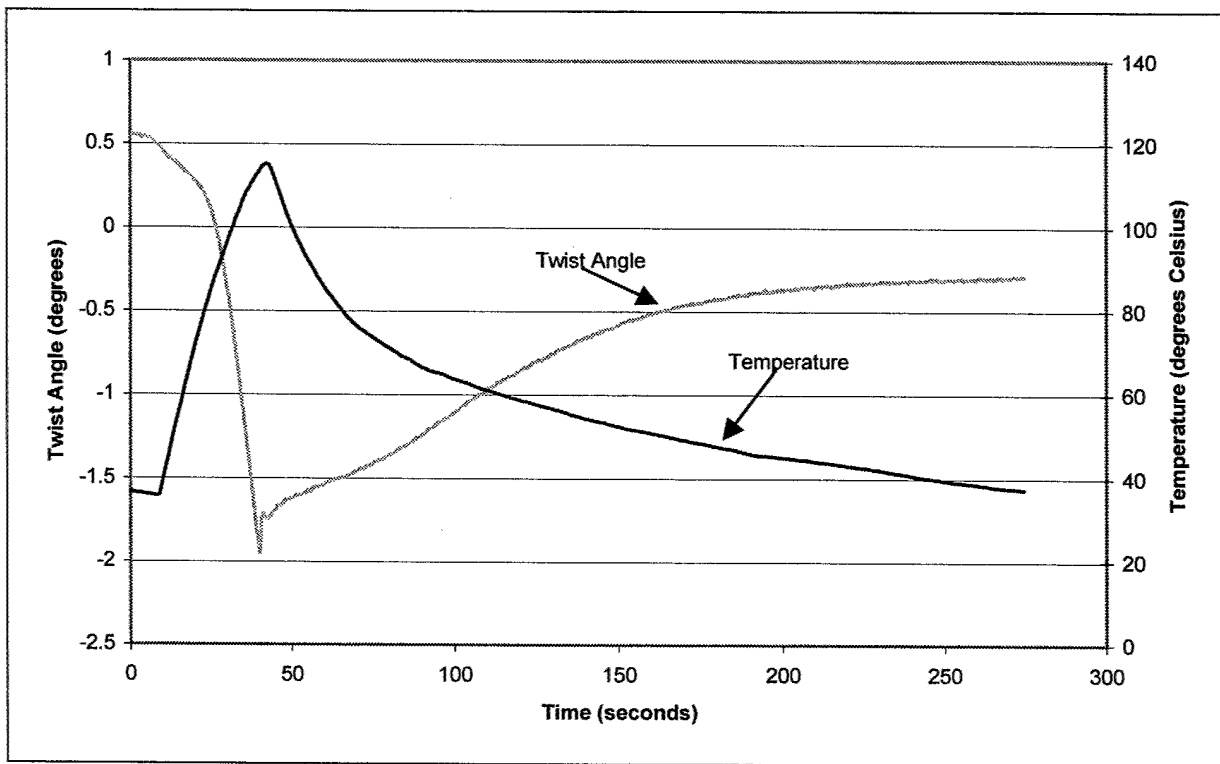


Figure 7.26: First Actuation of Bottom Wires

As in the previous test, this test was run for several cycles. The top and bottom wires were alternately heated and cooled, and the results were recorded for each actuation. These are shown below.

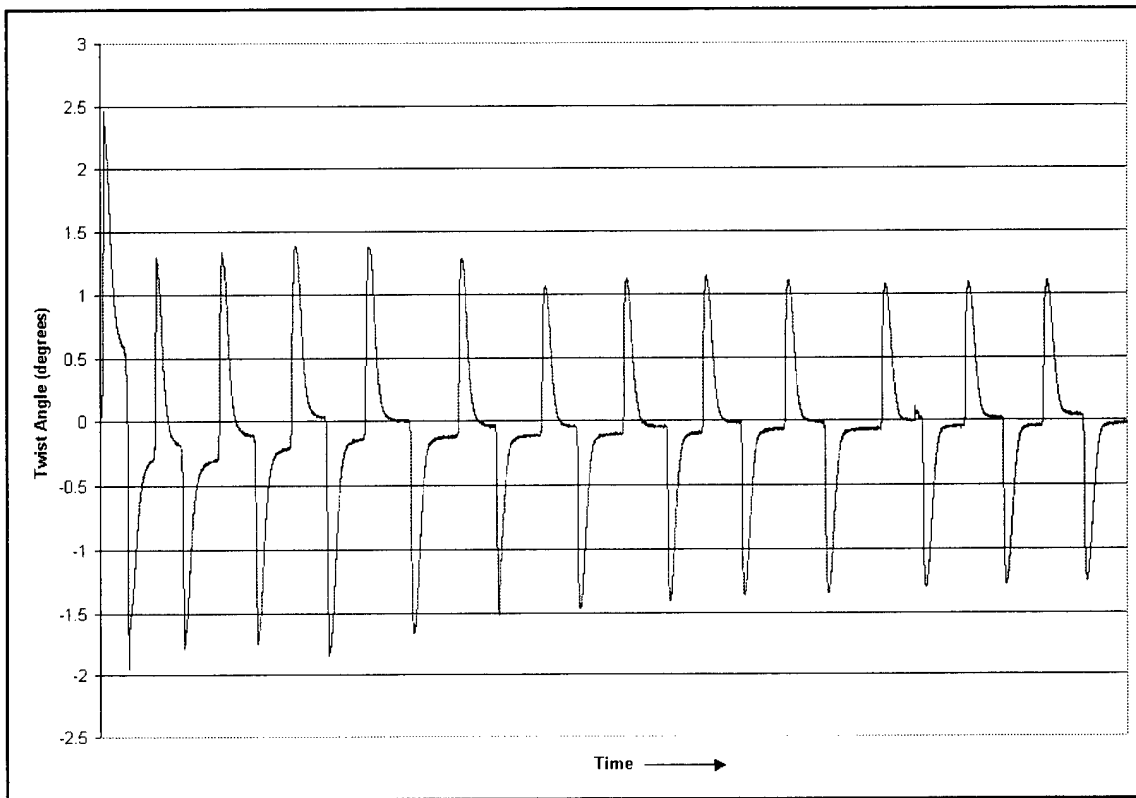


Figure 7.27: Twist Angle Evolution for Differential Actuation

The graph above illustrates two main points. First, the system seemed to settle in to a steady state as more cycles were run, as was seen in the previous section. Second, as the amount of cycles run on the wing increased, the residual twist when the wires cooled approached zero degrees.

7.3.3: Conclusion

Based on the results of the last two tests, the concept of using pins or other mechanical means to affix the SMA wires to the wing shows promise. In both the bias and differential setups, the system seems to settle into a predictable cycle of wing twist and relaxation.

If the bias approach were chosen, the wing would most likely have to be actuated multiple times prior to being attached to the aircraft to determine what the residual wing twist was after actuation. Then it could be attached in a way that would mitigate the pre-twist in the wing. For example, in the test described in Section 7.3.1, the residual wing twist was just over a

degree. If the wing were mounted so that this corresponded to zero degrees AOA, the wing would return to that AOA after each actuation cycle.

The differential approach is attractive because the system seems to reach an equilibrium condition where zero degrees AOA will be achieved whenever the wing relaxes. Furthermore, this system seems to provide a means to twist the wing in either direction, unlike the differential approach previously described and analyzed.

7.4: Comparison of Analytical and Experimental Results

The data obtained through the experiments described in this chapter are useful in evaluating the soundness of the modeling and analysis techniques described in Chapter Five. There is value in comparing the results for the amount of wing twist predicted as well as the time response of the actuator.

7.4.1: Structural Analysis

The analysis of the wing test blank in Chapter Five predicted that for the bias approach the SMA actuator would twist the wing 3.29 degrees. The measurements of the test specimen used in the oven test showed that the wires actually twisted the wing just over 3.5 degrees. The data from the bias approach test where the Nitinol was attached with pins indicated that the wing initially twisted approximately 3.2 degrees.

The analysis also predicted that when wires were added to the bottom of the wing for the differential approach, the resulting stiffness increase would decrease the maximum wing twist to 3.18 degrees. In the differential approach test of Section 7.3.2, the wing twisted to only 2.5 degrees. This indicates that the model underestimated the effect of adding the Nitinol to the bottom of the wing.

Overall, the analysis of the bias approach wing twist produced reasonable results, but the model for the differential approach was not as accurate. The major downfall of the analysis is its inability to predict how much twist the wing will actually recover as the wires cool back down below M_f . However, the modeling used to predict the amount of wing twist produced good results.

7.4.2: Time Response

The thermal analysis in Chapter Five was used to predict how fast the actuator could operate, given the expected flight conditions. The cycle times predicted were based on the assumption that considerable convective cooling would occur as the aircraft traveled through the air. In these tests, however, only free convection was present to cool the wires. The current used to heat the wires was also much smaller than that assumed in the analysis. Despite these differences, the test data can be used to evaluate the value of the thermal modeling.

If the ANSYS models used to predict the heating and cooling response of 1000 micron wires are slightly altered, they can be used to predict the heating and cooling rates given the actual test conditions. For the case of wires covered by epoxy, the following results are given for a current of five amps and a convection coefficient of five $\text{W/m}^2\text{-C}$. This convection coefficient is an estimate.

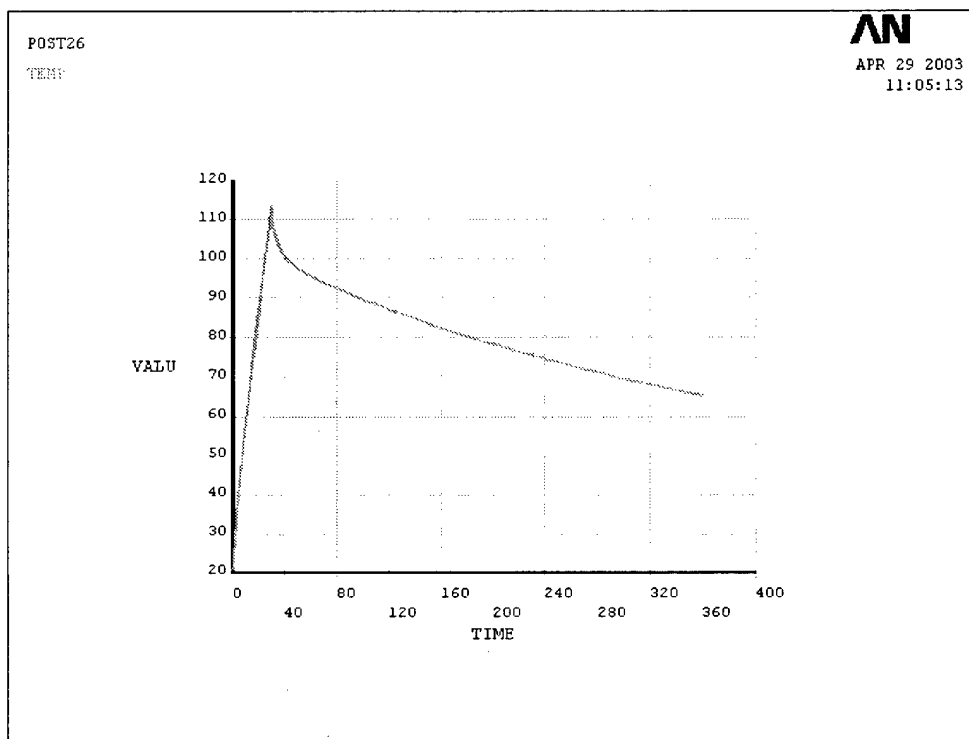


Figure 7.28: Revised Heating and Cooling Curve for 1000 Micron Wires (Time in seconds, Temperature in Degrees Celsius)

This revised model predicts that it will take approximately 30 seconds for the wire to heat from 20 degrees to 110 degrees. It predicts that cooling from 110 to 70 degrees will take 270 seconds.

The actual temperature data taken in the bias tests where epoxy was used to secure the wire are shown below.

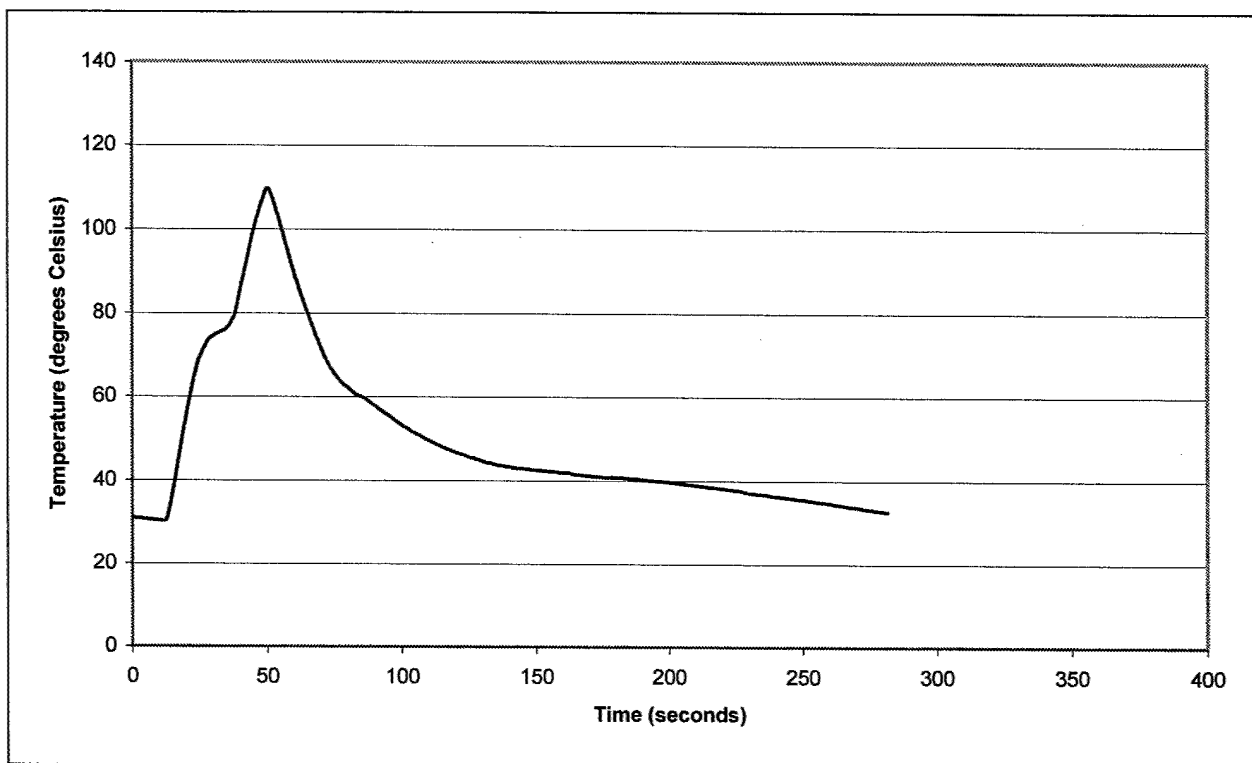


Figure 7.29: Heating and Cooling of Nitinol Wire Attached Using Epoxy

According to this data, it actually took approximately 38 seconds for the wire to heat from 30 degrees to 110 degrees. Cooling from 110 degrees to 70 degrees took only 20 seconds. Thus the thermal model appears to slightly underestimate the time needed to heat the wire while considerably overestimating the time needed for the wire to cool. This could be because of an overly conservative convection coefficient, but it could also be a result of inaccurate heat capacity and thermal conductivity data for the epoxy and fiberglass. If the wing absorbed more heat than expected, that would explain the longer heating time and shorter cooling time for the wires. Another possible explanation for the faster cooling rate is that much less epoxy was covering the wires, making the convective cooling much more effective.

The use of the pins to secure the wires for the last two tests provided a different case from those that were examined in Chapter Five. Because the wires are not covered in epoxy, it would be tempting to treat them as plain wires. In truth, they actually do not behave as plain wires

because they are touching both the fiberglass on the wing and the pins used to secure them. When the temperature history is examined for one of these tests, it is clear that the heating and cooling properties of these wires were not considerably different from those of the epoxy covered wires. This is shown in Figure 7.30.

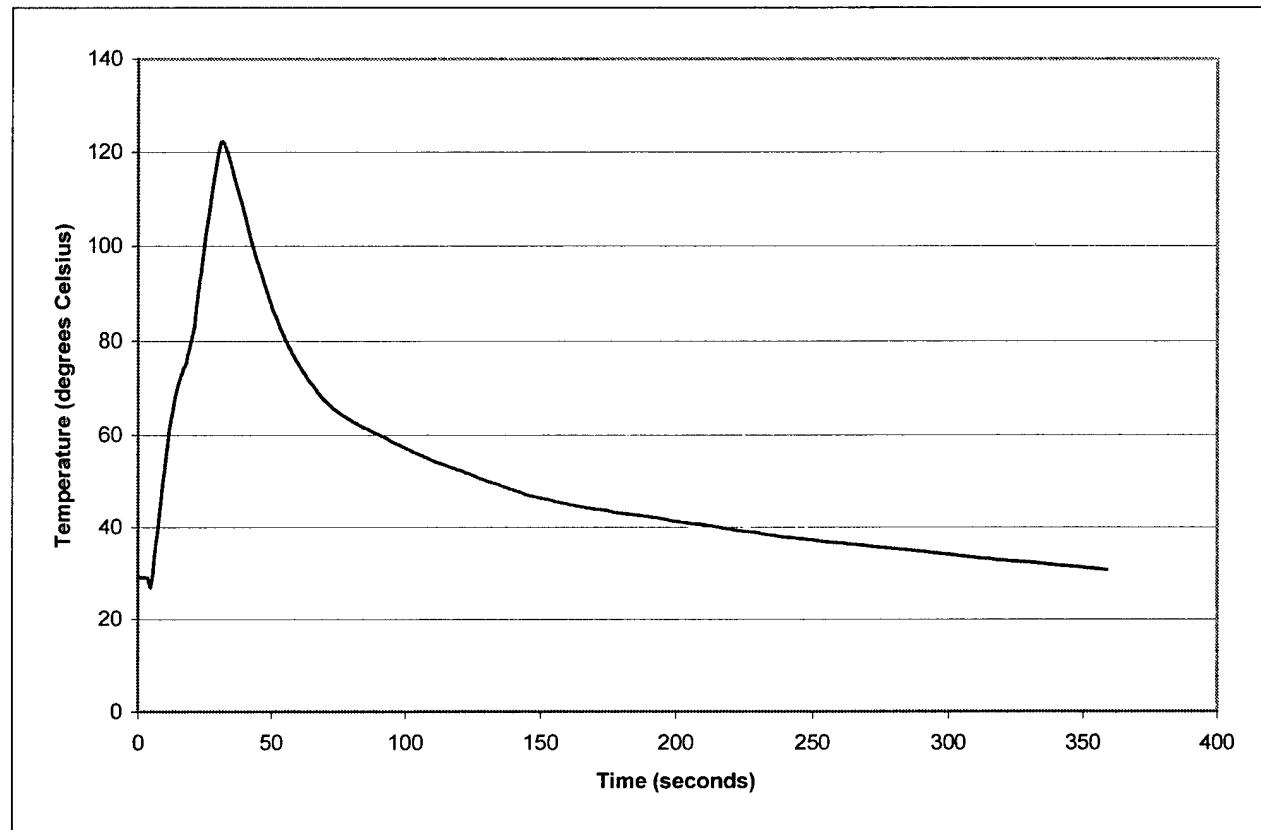


Figure 7.30: Heating and Cooling of Wires Attached Using Pins

Because of the similarity between the epoxy covered wires and those attached with pins, it is only necessary to determine how to correct the ANSYS model for covered wires. This could be as easy as determining a more accurate convection coefficient or more accurate material properties for the epoxy. Because the heating time of the model was of the right order of magnitude, this model should not be discounted.

7.4.3: Conclusion

Although these models are not flawless, they are a reasonable starting point for future analysis. It is likely that only small alterations would be necessary to develop models that are consistent with experimental results.

Chapter 8: Conclusions and Recommendations

The work in this thesis encompassed the design, analysis, and testing of a first order SMA actuator for the wing of the WASP, a small gun-launched UAV. First, a design concept was formulated. The basic design parameters were determined and two possible configurations were explored – the bias and differential approaches.

Next, detailed modeling and analysis was used to refine the conceptual design and to determine more specific parameters for the actuator. The thermal analysis determined the cycle time of the actuator and helped to determine the optimum size for the Nitinol wires. Structural analysis illustrated the amount of wing twist that could be expected if an actuator of this type was used. The allowable amount of pre-strain for the wires was also determined. Finally, a preliminary performance analysis showed what bank angles and roll rates could be achieved using the actuator.

Material testing was conducted to characterize the SMA wire to be used in the testing of a prototype actuator. Tensile tests were done to experimentally determine the modulus of elasticity of the wire in both the martensite and austenite phases. A cycle test was performed to determine the actual transition temperatures of the wire.

Finally, prototype actuators were fabricated and tested. Two methods for attaching the SMA wire to the wing were examined. The first was to use epoxy to attach the wires. The second was to wrap the wire around pins in the wing. The results of these tests, as well as the results of the analysis, have produced several important conclusions.

8.1: Conclusions

This thesis has demonstrated that shape memory alloy wires can be used to induce significant amounts of twist in the wing of a small UAV. Testing of prototype actuators has

shown that twist angles of over one degree can be repeatedly achieved with a very simple design. Performance analysis has shown that this amount of wing twist can produce roll rates of over 25 degrees/second.

Testing has also shown that mechanical attachment of the SMA wires results in a much more reliable actuator. Using epoxy to attach the wires to the surface of the wing was almost totally unsuccessful. Even using a high temperature epoxy does not seem to solve the problem of thermal degradation of the adhesive as the wire is heated rapidly. On the other hand, using mechanical means, such as pins or other devices, to attach the wires showed much promise. Repeated actuation cycles were performed, and once the system settled, the performance of the actuator seemed to stabilize at a predictable level. As predicted in the analysis, the addition of heat into the wing did not cause any noticeable deformations due to the effects of the wing materials' coefficients of thermal expansion. Since the amount of pre-strain used in the design was based on analysis of an epoxy bond, using mechanical attachment would mean that larger pre-strains could be used. This would result in larger wing twist values.

This thesis has also shown, however, that an SMA actuator is probably not fast enough to be the only means of roll control for the aircraft. The thermal analysis of wires fully covered by epoxy showed that the best possible cycle time for the actuator is 3.2 seconds. Since testing showed that the time response of the mechanically attached wires was very similar to that of the epoxy attached wires, this cycle time can be assumed for the mechanically attached wires as well. If the only maneuvers needed are slow banking turns to keep the aircraft in a racetrack flight path, this is probably a sufficient time constant. However, a small UAV is sure to be affected by even small wind gusts, making higher frequency roll control a necessity.

8.2: Recommendations

This thesis has demonstrated that an SMA actuator has the potential of providing a roll control solution for a small UAV. In order to make an SMA actuator a reliable device, however, significant work remains.

In the near term, there are a few significant steps to be taken. First, testing similar to that described in the previous chapter should be done in a wind tunnel so as to experimentally determine the actuator time constant. The WASP is designed to cruise at 60 mph, and testing at this speed would provide the higher convection needed to rapidly cool the wires. This testing

would also allow the performance to be characterized with accurate aerodynamic loads taken into account.

Another short-term improvement would be to investigate the use of a different Nitinol alloy. The binary alloy used in this thesis showed a very large temperature hysteresis, which significantly increased the time constant of the actuator. Balta et. al. noted that Nitinol alloys containing copper, NiTiCu, have lower hysteresis values [17]. Testing this alloy should be considered. If an alloy with a smaller hysteresis is used, it may be possible to lower the A_f temperature needed for the wire. The only guideline to be remembered is that the M_f temperature must be greater than the highest temperature in which the aircraft will operate.

An improvement to the models used in Chapter Five would be to more accurately determine the convective film coefficients for both free and forced convection of the Nitinol wires. Both values used in this thesis were estimates, and both were most likely very conservative. Related to this would be the determination of more accurate material properties for the epoxy.

In the medium to long term, many more steps should be taken to improve the SMA actuator design of this thesis. First, the interaction between the epoxy and the Nitinol wire should be investigated in depth. As mentioned earlier, the epoxy did not degrade if the temperature was gradually increased. However, as the wire was rapidly heated, localized failure of the epoxy occurred. The effect of various heating rates should be examined to see if there is a limit to how fast the epoxy can be heated. Since the wire needs to be heated as quickly as possible, this limit must be known if epoxy is used to bond the wire to the wing.

Furthermore, the apparent heating delay that occurred when the wire reached approximately 75 degrees Celsius should be explored. Since this delay did not occur in any of the tests where the wire was mechanically attached to the wing, it appears that a strange interaction takes place between the Nitinol wire and the epoxy. It is possible that at that temperature some phase change in the epoxy occurs, allowing it to absorb more heat without increasing temperature. On the other hand, it could be a property of the Nitinol that causes it to "dump" more heat at that temperature. This interaction should be studied to see if it is related to the degradation of the epoxy.

If one-way shape memory is to be used, as in this thesis, there is an optimization problem to be considered in terms of the balance between actuator strength and the wing's stiffness. In

the experiments described in this thesis, it was apparent that the actuator had enough strength to twist the wing. The wing, however, did not have enough stiffness to fully deform the wires when they cooled. This resulted in residual wing twist. There is some optimal design to be found where the actuator can twist the wing just enough to provide the necessary roll moment, while the wing is stiff enough to fully deform the wires and return to zero degrees AOA.

An alternative to this optimization problem would be to investigate the use of two-way shape memory. If two-way SMA's were used, there would be no need to depend on the stiffness of the wing to deform the wires. As the wires cooled, they would automatically elongate, allowing the wing to untwist fully. Previous work has shown that two-way shape memory can be obtained by relatively simple training procedures [18,19].

Because of the success of mechanically attaching the wires, it would be extremely valuable to explore this option further. The pins used for the specimens tested in this project were bulky and extended far out of the plane of the wing surface. This would obviously cause excessive drag. A more subtle way to mechanically affix the wires to the wing is surely possible, and it would eliminate the need for a high temperature epoxy. One option is to redesign the inboard panel of the WASP wing to include hard points for attaching the SMA wires. It is very likely that a more precise manufacturing process for the actuator would result in a smaller drop in performance as the system "settles in."

Another possibility worth exploring is the idea of etching the desired Nitinol pattern out of a plate of the material. This would allow for a flat surface to contact the surface of the wing, which should enhance the bond strength if an adhesive is used to attach the Nitinol to the wing. Since the pattern would be etched into the Nitinol, no bending procedure would be needed.

It would also be valuable to consider the option of switching directions and moving to an SMA torque tube, as was used in the DARPA Smart Wing concept [26,27]. This concept could be scaled to apply to a small-scale wing like the one on the WASP. If it was found to be structurally robust enough to survive the high-g environment, a torque tube could be used to twist the wing about its span axis.

Finally, the possibility of using the SMA actuator in conjunction with another actuation device should be considered. Because of its large time constant, the SMA actuator probably cannot actuate the wing fast enough or often enough to respond to perturbations caused by wind gusts. On the other hand, higher frequency actuators such as piezoelectric devices, while

actuating at very high frequencies, often cannot provide the deformations needed to induce large roll moments. The solution may be to include actuators of both types on the wing. The high frequency actuators can be used to keep the aircraft in stable flight, while the SMA actuator can be used to induce the roll needed for larger turns and changes in direction.

[THIS PAGE INTENTIONALLY LEFT BLANK]

References

- [1] Martorana, Richard T. *Wide Area Surveillance Projectile (WASP) Final Report*. Charles Stark Draper Laboratory. CSDL-R-2898. Cambridge, MA, 2001.
- [2] Jenkins, Stacy. *Investigation of Curved Composite Panels Under High-G Loading*. Massachusetts Institute of Technology. Cambridge, MA, 1999.
- [3] Kessler, Seth. *Design and Manufacture of a High-G Unmanned Aerial Vehicle Structure*. Massachusetts Institute of Technology. Cambridge, MA, 2000.
- [4] Martorana, Richard T. *Wide Area Surveillance Projectile g-Hardening Program Final Report*. Charles Stark Draper Laboratory. CSDL-R-2933. Cambridge, MA, 2002.
- [5] Kepets, Mark. *Actively Conformable Aerodynamic Surfaces*. Massachusetts Institute of Technology. Cambridge, MA, 2002.
- [6] Friend, C. M. and N. B. Morgan. “Shape Memory Alloys in Medicine – From New Prosthetic Devices to ‘Cuddly’ Instruments.” *Medical applications for shape-memory alloys (SMA)*. Institution of Mechanical Engineers. Bury St. Edmunds, UK, 1999.
- [7] Lipscomb I. P. and L. D. M. Nokes. *The Application of Shape Memory Alloys in Medicine*. Mechanical Engineering Publications Ltd. Suffolk, UK, 1996.
- [8] Otsuka, K. and C. M. Wayman. *Shape Memory Materials*. Cambridge University Press. Cambridge, UK, 1998.
- [9] Hodgson, Darel E., Ming H. Wu and Robert J. Biermann. “Shape Memory Alloys.” Shape Memory Applications Inc. Santa Clara, CA, 1999.
- [10] Chang, L. C. and T. A. Read. AIME vol. 191, p 47, 1951.
- [11] *Shape Memory Alloys*. Ed. Hiroyasu Funakubo. Translated by J. B. Kennedy. Gordon and Breach Science Publishers. New York, 1987.
- [12] *Engineering Aspects of Shape Memory Alloys*. Ed. T. W. Duerig, K. N. Melton, D. Stockel, and C. M. Wayman. Butterworth – Heinmann. London, 1990.
- [13] Liang, Jia and Rogers. “Behavior of Shape Memory Alloy Reinforced Composite Plates Part II: Results.” *Proceedings of the 30th Structures, Structural Dynamics and Materials Conference*, AIAA-89-1331 CP, pp 1504-1513, 1989.

[14] Rogers, C. A. "Active Vibration and Structural Acoustic Control of Shape Memory Alloy Hybrid Composites: Experimental Results." *Journal of the Acoustical Society of America*, 88(6): 2803-2811, 1990.

[15] Baz, Imam, and McCoy. "Active Vibration Control of Flexible Beams Using Shape Memory Actuators." *Journal of Sound and Vibration*, 140(30): 437-456, 1990.

[16] Bidaux, J., J. Manson, and R. Gotthardt. "Active Stiffening of Composite Materials by Embedded Shape Memory Alloy Fibres." *Materials Research Society Proceedings*, 459, (1997): 107.

[17] Balta, J. A., V. Michaud, M. Parlinska, R. Gotthardt, and J. Manson. "Adaptive Composites with Embedded NiTiCu Wires." *Proceedings of SPIE: Smart Structures and Materials 2001: Active Materials: Behavior and Mechanics*. Vol. 4333, 2001.

[18] White, S. R., M. E. Whitlock, J. B. Ditman, and D. A. Hebda. "Manufacturing of Adaptive Graphite/Epoxy Structures with Embedded Nitinol Wires." *Adaptive Structures and Material Systems - American Society of Mechanical Engineers*. AD vol. 35. ASME, New York, 1993.

[19] Hebda, D. A., M. E. Whitlock, J. B. Ditman, and S. R. White. "Manufacturing of Adaptive Graphite/Epoxy Structures with Embedded Nitinol Wires." *Journal of Intelligent Material Systems and Structures*. Vol. 6, March 1995.

[20] Hebda, D. A. and S. R. White. "Structural Behavior of SMA Composite Beams." *Adaptive Material Systems* AMD Vol. 206/MD Vol. 58, 1995.

[21] Song, G., B. Kelly, B. N. Agarwal, P. C. Lam, and T. S. Srivatsan. "Application of Shape Memory Alloy Wire Actuator for Precision Position Control of a Composite Beam." *Journal of Materials Engineering and Performance* Vol. 9(3), June 2000.

[22] Whitting, Jan, Koray Safak, and George G. Adams. "SMA Actuators Applied to Biomimetic Underwater Robots." *Neurotechnology for Biomimetic Robots*. Ed. Joseph Ayers, Joel L. Davis, and Alan Rudolph. The MIT Press: Cambridge, MA, 2002.

[23] Rediniotis, O. K., L. N. Wilson, D. C. Lagoudas, and M. M. Khan. "Development of a Shape Memory Alloy Actuated Biomimetic Hydrofoil." *Journal of Intelligent Materials and Structures*, 2002.

[24] Rediniotis, Othon K. and Dimitris C. Lagoudas. "Shape Memory Alloy Actuators as Locomotor Muscles." AIAA, 2001.

[25] Strelec, Justin K. and Dimitris C. Lagoudas. "Fabrication of Testing of a Shape Memory Alloy Actuated Reconfigurable Wing." SPIE Proceedings, 2002.

- [26] Kudva, J. N., K. Appa, A. Jardine, C. Martin, and B. Carpenter. "Overview of Recent Progress on the DARPA / USAF Wright Laboratory 'Smart Materials and Structures Development – Smart Wing' Program." SPIE Vol. 3044, 1997.
- [27] Jardine, Peter, John Flanigan, Chris Martin, and Bernie Carpenter. "Smart Wing Shape Memory Alloy Actuator Design and Performance." SPIE Vol. 3044, 1997
- [28] "Selected Properties of NiTi." SMA-Inc. Company Website URL: <http://www.sma-inc.com/NiTiProperties.html>. Cited 10 September 2002.
- [29] "DuPont Kapton 500HN Polymide Film." Matweb URL: <http://www.matweb.com>. Cited 23 May 2002.
- [30] "Rohacell 31 Polymethacrylimide (PMI) Rigid Foam Sheet." Matweb URL: <http://www.matweb.com>. Cited 17 April 2002.
- [31] Nokes, D. Charles Stark Draper Laboratory. Conversation, January 2002.
- [32] "Typical Physical Properties." West System Company Website URL: <http://www.westsystem.com/webpages/userinfo/moreinfo/properties.htm>. Cited 23 May 2002.
- [33] Roskam, Jan. *Airplane Flight Dynamics and Automatic Flight Controls Part I*. DARcorporation: Lawrence, KS, 1995.
- [34] "Shape Memory Applications, Inc." Company Website URL: <http://www.sma-inc.com>. Cited 6 May 2003.
- [35] "Cotronics Corp." Company Website URL: <http://www.cotronics.com>. Cited 6 May 2003.
- [36] "West System." Company Website URL: <http://www.westsystem.com>. Cited 6 May 2003.

[THIS PAGE INTENTIONALLY LEFT BLANK]